

INDIAN INSTITUTE OF SCIENCE EDUCATION AND
RESEARCH (IISER) PUNE

DOCTORAL THESIS

**Search for supersymmetry in events with a
photon, jets, b-jets, and missing transverse
momentum**

Author:
Vinay HEGDE

Supervisor:
Dr. Seema SHARMA

*A thesis submitted in fulfillment of the requirements
for the degree of Doctor of Philosophy
in the*

**Experimental Particle Physics
Department Physics**

April 29, 2019

Abstract

Although many of the experimental observations can be theoretically well explained using standard model (SM) of particle physics, SM is not complete because it does not explain gravity, dark matter and dark energy in the universe, matter-antimatter asymmetry, nonzero neutrino mass, observed mass of the Higgs boson being much lower than theoretically favored value etc. Supersymmetry (SUSY) is a well motivated theoretical extension of the SM which can address some of the issues in SM such as, Higgs mass problem and dark matter problem. In SUSY, every SM particle has a superpartner whose spin differs by half a unit. We have not yet observed superpartners with same masses as their SM counterparts which makes SUSY a broken symmetry. There are several theoretical mechanisms to achieve this symmetry breaking, and one of the mechanisms is gauge mediated SUSY breaking (GMSB). If GMSB is realized in nature, it typically results in events with one or more photons in the final state. A search for SUSY is presented based on events with at least one photon, jets, and large missing transverse momentum produced in proton-proton collisions at a center-of-mass energy of 13 TeV. The data correspond to an integrated luminosity of 35.9 fb^{-1} and were recorded at the LHC with the CMS detector in 2016. The analysis characterizes signal-like events by categorizing the data into various signal regions based on the number of jets, the number of b-tagged jets, and the missing transverse momentum. No significant excess of events is observed with respect to the expectations from standard model processes. Limits are placed on the gluino and top squark pair production cross sections using several simplified models of supersymmetric particle production with GMSB scenario. Depending on the model and the mass of the next-to-lightest supersymmetric particle, the production of gluinos with masses as large as 2120 GeV and the production of top squarks with masses as large as 1230 GeV are excluded at 95% confidence level.

Acknowledgements

My heartfelt gratitude to my supervisor Dr. Seema Sharma for her valuable guidance throughout my doctoral thesis project. She has provided me many opportunities and freedom to explore new ideas, and interact with experts in the field. I am very thankful to her for her valuable advises and helping me all these years of my PhD.

I would like to thank Prof. Gobinda Majumder for sharing his experience and insight to understand forward hadron calorimeter. This was my first project in experimental high energy physics, and gave me a good kick start to move towards my thesis project.

I would like to thank Dr. Andrew Whitbeck, who has been a wonderful collaborator, for his invaluable support to make this a very learning experience through his skills and physics insight. I owe a big thanks to Dr. Andrew Whitbeck and Dr. Kevin Pedro for all the help during the physics analysis, and to make it an enjoyable and successful journey. I would also like to thank Dr. Giovanni Zevi Della Porta for a possibility to interact with electron photon group of the CMS, and contribute to the SUSY group. I also extend my gratitude to Dr. Rishi Patel, Dr. James Francis Hirschauer, and Prof. Meenakshi Narain for various interactions during the course of my PhD.

My sincere thanks are due to Dr. Sourabh Dube & Dr. Monoranjan Guchait to be members of the research advisory committee (RAC). Their availability whenever needed, regular feedback and inputs helped in timely completion of this project.

My special thanks to CMS collaboration and CERN for providing high quality experimental setup and resources.

In this journey of 5 years, my institute, Indian Institute of Science Education and Research (IISER) Pune, has been of great support. The institute and the Physics department has provided very good environment, various research facilities and also a constant financial support. The academic and non-academic activities at IISER made my stay very enjoyable. My sincere gratitude to the institute for all the help. I would like to acknowledge Department of Science and Technology, India for enduring financial support to carry about research on CMS experiment. I would also like to acknowledge Fermilab/LPC for supporting my visit which helped to get a broader perspective on CMS research.

Thanks to Mr. Prabhakar Anagare, Ms. Dhanashree Sheth, Mr. Tushar Kurulkar and his team for helping with administrative work at IISER; IT department (Ms. Nisha Kurkure, Mr. Goldi Misra & team), Mr. Brij Kishor Jashal and his team from TIFR for providing very good computing resources.

Last, but never the least, my heartfelt gratitude to EHEP group at IISER (Dr. Seema Sharma, Dr. Sourabh Dube, Ms. Aditee Rane, Ms. Angira Rastogi, Mr. Anshul Kapoor, Mr. Arnab Laha, Ms. Bhumika Kansal, Dr. Kunal Kothekar, Mr. Shubham Pandey, Mr. Shubhanshu Chauhan and undergraduate students), friends & family for having lots of fun, discussions and supporting me at all times.

Contents

Abstract	iii
Acknowledgements	v
1 Introduction	1
2 Standard model and supersymmetry	3
2.1 Standard model particles	3
2.2 Conservation laws and symmetry	4
2.3 Strong interactions	4
2.4 Electro-weak interactions	5
2.5 The Higgs mechanism	5
2.6 Limitations of SM	6
2.7 Supersymmetric extension of the SM	7
2.7.1 R-parity	9
2.8 Gauge mediated SUSY breaking	10
2.8.1 Phenomenology of GMSB	10
2.8.2 Simplified GMSB models	11
3 The Experimental Setup	13
3.1 The large hadron collider	13
3.1.1 Luminosity	14
3.2 The compact muon solenoid	16
3.2.1 CMS coordinate system	16
3.2.2 Superconducting magnet	16
3.2.3 Inner tracking system	17
Performance of tracker	18
3.2.4 Electromagnetic calorimeter	19
3.2.5 Hadron calorimeter	20
3.2.6 Muon chambers	22
3.3 Energy response in long and short fibers of HF calorimeter	22
3.3.1 Data and simulation samples	23
3.3.2 Energy in long and short fibers of HF	24
3.3.3 Effect of Pileup on $R_{S/L}$	26
3.3.4 Studying $R_{S/L}$ at $\sqrt{s} = 13$ TeV and 8 TeV data with 50 ns bunch spacing	27
3.3.5 $R_{S/L}$ for 2015 Data and 2016 Data	29
3.3.6 Performance of $R_{S/L}$ in 2016 Data	31
Stability of $R_{S/L}$ in 2016 Data	32
3.3.7 Corrections for the $R_{S/L}$ Based on ϕ Symmetry	33
3.3.8 Performance of $R_{S/L}$ in data & MC	36
$R_{S/L}$ vs $i\eta$	37
$R_{S/L}$ vs $i\phi$	38

3.3.9	Summary of HF studies using $R_{S/L}$	39
3.4	Trigger system	41
3.5	Object reconstruction	42
3.5.1	Tracking	43
3.5.2	Interaction vertices	43
3.5.3	Muons	44
3.5.4	Electrons and photons	44
Photon Identification		45
Electron Identification		46
3.5.5	Jets	49
3.5.6	Tagging of b-quark jet	51
3.5.7	Missing transverse momentum	52
4	SUSY search with photon	55
4.1	Introduction	55
4.2	MC simulation samples	57
4.3	Triggers	57
4.3.1	Signal triggers	58
4.3.2	Multijet triggers	60
4.4	Event selection	60
4.5	SM background and search regions	63
4.5.1	Optimization of search bins	64
4.6	Background Estimation	65
4.6.1	Lost lepton estimation	67
4.6.2	Estimation of events with electrons faking photons	70
Fake-rate parameterization		71
Data/MC fake rate corrections		71
Fake rate prediction		72
4.6.3	Invisible Z estimation	72
4.6.4	$\gamma + \text{jets}$ and QCD multijet estimation	75
4.7	Systematic uncertainty for signal models	79
5	Results and summary	83
5.1	Results & statistical interpretations	83
5.2	Summary	87
5.3	Outlook	89
5.3.1	Electroweak models	89
5.3.2	Sensitivity of the search	89
A	Additional tables	91
A.1	Lost lepton + τ_{had} predictions	91
A.2	Electron fake photon	93
A.3	Invisible Z estimation	96
A.4	$\gamma + \text{jets}$ and QCD multijet	97
B	Data verses MC in control regions	99
B.1	$e/\mu + \gamma$ control region	99
B.2	$Z(\ell\ell) + \gamma$ control region	100
B.3	Signal acceptance \times efficiency	101
C	Data cleaning	103

List of Figures

2.1	SM cross section measurements by CMS	6
2.2	Top loop diagram contribution to H mass	7
2.3	Corrections to H mass from top loop and stop loop.	8
2.4	Proton decay diagram	9
2.5	BR for bino and neutral wino NLSP decays	11
2.6	SMS diagrams	11
3.1	CERN accelerator complex	13
3.2	Integrated luminosity of data	15
3.3	CMS detector view	16
3.4	CMS tracker	17
3.5	Tracker resolution for muons	18
3.6	Track reconstruction efficiency	18
3.7	Tracker material budget	19
3.8	ECal schematic and resolution	20
3.9	Schematic diagram of HCal	21
3.10	Muon chambers	22
3.11	Muon p_T resolution	23
3.12	Channel occupancy for depth 1 and depth 2	25
3.13	Total number of rechits (inclusive in $i\eta$ and $i\phi$)	25
3.14	Distribution of E_{Short} vs E_{Long} for HF channels.	25
3.15	$R_{S/L}$ for $i\eta$ 32 tower with $i\phi$ inclusive for 2015D-50 ns.	26
3.16	Asymmetric Gaussian fit for $i\eta$ 30	26
3.17	Asymmetric Gaussian fit for $i\eta$ 39	26
3.18	Effect of pileup on $R_{S/L}$ for different $i\eta$	27
3.19	Pileup comparison for 2015 data and 2012 data	27
3.20	E_{Long} for 2012 and 2015 data	28
3.21	E_{Short} for 2012 and 2015 data	28
3.22	$R_{S/L}$ vs $i\eta$ for 3 different run conditions	28
3.23	$R_{S/L}$ vs $i\phi$ plot for $i\eta$ -35	29
3.24	Number of primary vertices before re-weighting	29
3.25	Number of primary vertices after re-weighting	29
3.26	No. of HF RecHits above 10 GeV	30
3.27	HF RecHit energy in long and short fibers	30
3.28	Energy in long	30
3.29	Energy in short	30
3.30	$R_{S/L}$ for 2015 and 2016B data	31
3.31	No. of primary vertices for 2016 run eras	31
3.32	No. of rechits for 2016 run eras	32
3.33	RecHitEnergy distributions for 2016B,C,D,E	32
3.34	RecHitEnergy distributions for 2016B,F,G, H	32
3.35	$R_{S/L}$ vs $i\eta$ for 2016 with lower E_{long} threshold	33

3.36 $R_{S/L}$ vs $i\eta$ for 2016 with higher E_{long} threshold	33
3.37 $R_{S/L}$ vs $i\phi$ for 2016B,C,D,E	34
3.38 $R_{S/L}$ vs $i\phi$ for 2016B,C,D,E	34
3.39 Correction factors as a function of $i\eta, i\phi$	35
3.40 $R_{S/L}$ vs $i\phi$ for $i\eta = 30$ before and after corrections	35
3.41 $R_{S/L}$ vs $i\phi$ for $i\eta = 38$ before and after corrections	35
3.42 $R_{S/L}$ vs $i\phi$ with $E_{long} > 30, E_{short} > 10$	36
3.43 $R_{S/L}$ vs $i\phi$ with $E_{long} > 100, E_{short} > 10$	36
3.44 Observed no. of interactions in data and MC	37
3.45 Number of reconstructed primary vertices in data and MC	37
3.46 Number of HF rechits above 10 GeV	37
3.47 HF rechit energy in data and MC	38
3.48 $R_{S/L}$ vs $ i\eta $ with $E_{long} > 20, E_{short} > 10$ GeV	38
3.49 $R_{S/L}$ vs $ i\eta $ with $E_{long} > 40, E_{short} > 10$ GeV	39
3.50 $R_{S/L}$ vs $i\eta$ with $E_{long} > 100, E_{short} > 10$	39
3.51 $R_{S/L}$ vs $i\eta$ with $E_{long} > 50, E_{short} > 50$	39
3.52 $R_{S/L}$ vs $i\phi$ for data and MC	40
3.53 SM cross section vs SUSY cross section	41
3.54 Schematic of L1T	42
3.55 Particle interaction in CMS	42
3.56 Loose + pixel seed veto photon efficiency	46
3.57 TnP fit for MiniIso pass/fail	48
3.58 Mini-isolation efficiency and SF	48
3.59 Energy energy composition	49
3.60 Application of JEC	50
3.61 Jet p_T response with and w/o corrections	50
3.62 AK4PF jet energy resolution	51
3.63 b-jet showing b-hadron decays	51
3.64 CSVv2 output and b-tagging efficiency	52
3.65 p_T^{miss} resolution	53
4.1 SMS diagrams	56
4.2 Photon165 trigger efficiency	58
4.3 Photon90_PFHT600 trigger efficiency	59
4.4 Efficiency for SR triggers	59
4.5 Single electron CS trigger efficiency	59
4.6 0 photon VR trigger efficiency	60
4.7 $p_T^\gamma, p_T^{miss}, N_{jets}, N_{b\text{-jets}}$, and H_T^γ after baseline selection	63
4.8 MC BG vs signal in search and sideband regions	64
4.9 Optimization of bins using MC	66
4.10 Pie charts showing BG in low p_T^{miss}	66
4.11 m_T distribution for $\mu\gamma$ control region	67
4.12 Closure for lost lepton and τ_{had}	69
4.13 $\Delta R(\ell, \gamma)$ for $\mu\gamma$ and $e\gamma$ CRs	70
4.14 Q_{mult} distribution for DY, W+jets, and $t\bar{t}$	71
4.15 Fake rate closures	72
4.16 Tag & probe fits for data and MC	73
4.17 Comparing $Z(l\bar{l})\gamma$ with $Z(\nu\bar{\nu})\gamma$	74
4.18 $\text{Min}(\Delta\phi_1, \Delta\phi_2)$ in MC	76
4.19 ABCD regions	76
4.20 Closure for $\gamma +$ jets and QCD multijet	77

4.21 Closure for VR	78
4.22 Double ratio validation	78
5.1 Results: Prediction vs observation in 25 search bins	87
5.2 Exclusions for strong SMS models	88
5.3 TChiWG and TChiNG SMS digrams	89
5.4 Expected UL for EW for SUSY	90
B.1 Data vs MC for $e\gamma$ CR	99
B.2 Data vs MC for $\mu\gamma$ CR	100
B.3 $ll + \gamma$ in data vs $ll + \gamma$ in MC	101
B.4 Acceptance \times efficiency for signal	102
C.1 Data cleaning	103

List of Tables

2.1	Leptons and quarks of SM with their properties	3
2.2	Gauge bosons and higgs boson in SM with their properties	3
2.3	Chiral and gauge supermultiplets of MSSM	8
2.4	Gauge and mass eigenstates of MSSM	9
3.1	The LHC parameters	15
3.2	Characteristics of tracker	17
3.3	Collision data used for $R_{S/L}$ studies of HF	24
3.4	Photon Identification	45
4.1	Event selections	62
4.2	Signal region and sideband regions	64
4.3	TFs for lost lepton and τ_{had}	68
4.4	Fake rate SFs	72
4.5	Purity in the $Z\gamma$ control region.	74
4.6	Electroweak corrections as a function of p_T^{miss}	75
4.7	Double ratio in data and MC for validation region	77
4.8	Systematic uncertainties for signal samples	81
5.1	Results: Prediction vs observation	86
A.1	Lost lepton predictions in high $\Delta\phi$	91
A.2	Lost lepton predictions in low $\Delta\phi$	92
A.3	Fake rate parameterization	93
A.4	Fake rate predictions in high $\Delta\phi$	94
A.5	Fake rate predictions in low $\Delta\phi$	95
A.6	$Z(\nu\nu) + \gamma$ predictions in high $\Delta\phi$	96
A.7	$Z(\nu\nu) + \gamma$ predictions in low $\Delta\phi$	96
A.8	$\gamma + \text{jets}$ and QCD multijet predictions	97

Dedicated to my Parents...

Chapter 1

Introduction

Since time immemorial, human beings have wondered about the causes of natural phenomena taking place in the universe. A persistent question has been about the building blocks of the universe and what holds it together. Based on our understanding, as of today, there are four fundamental forces:

- Gravitational force: this causes apples to fall and also the planets to revolve around the sun.
- Electromagnetic force: holds atoms together, basic principle in chemistry. Almost everything, except gravity, that we come across in daily life is governed by this force.
- Weak force: β decay taking place in the nucleus is because of this force.
- Strong force: the force which holds protons and neutrons together in the nucleus.

The matter that we see around us is made up of atoms. An atom is made up of a nucleus (consisting of protons and neutrons, collectively called nucleons) and electrons. Nucleons are composed of fundamental particles called quarks. So the matter around us can be thought of as some combination of electrons and quarks, mainly. Apart from these, there are also other fundamental particles, some of which are similar to electrons and quarks but not the dominant constituents of ordinary matter, some are mediators of the fundamental forces and one is responsible for particles to acquire mass. There are 3 flavors of charged leptons, 3 flavors of neutral leptons, 3×2 flavors of quarks, 5 mediators of forces and a Higgs boson. In total there are 18 such fundamental particles which we know today. Can we put all these particles and forces into a framework and try to understand the phenomena around us? The attempt that we made so far for this purpose has led to the standard model (SM) of particle physics [1, 2, 3]. Our attempt is not complete because in the framework of SM, we could not fit gravitational force or interaction and also the mediator of gravity, the graviton. Graviton is a hypothetical particle, not experimentally detected, not included in the SM. So the SM consists of 17 fundamental particles and their mutual interactions can be explained by three fundamental forces.

The SM has successfully explained many of the experimental results; with very high degree of precision in certain cases, such as the measurement of magnetic moment of electron [4]. But the SM is not a complete story of the universe. There are many issues in the SM, such as the inability to explain dark matter [5, 6] and dark energy [7] in the universe, matter anti-matter asymmetry [8, 9] etc, and many theoretical problems such as hierarchy problem [10], imperfect gauge coupling unification etc. To address some of these questions, many extensions of SM have been proposed,

one of them being the supersymmetry (SUSY). SUSY predicts that for every SM particle, there is a superpartner similar in all the quantum numbers and properties except that the spin quantum number differs by half a unit. Failure to experimentally observe supersymmetric particles with same mass as SM particles (we did not find supersymmetric electron, called selectron or supersymmetric proton, called sproton etc), led to the idea that SUSY is broken and the sparticles are massive as compared to their SM counterparts. There are many ways of breaking SUSY, one of them being gauge mediated SUSY breaking (GMSB). In scenarios with GMSB, gravitino (the super partner of hypothetical graviton) is the lightest supersymmetric particle (LSP) and it is stable. The stability of LSP is a requirement from R-parity conservation which does not allow supersymmetric particle decay into only SM particles. LSP is weakly interacting particle and hence it does not leave any visible signature in the detector and it is a viable dark matter candidate.

The compact muon solenoid (CMS) detector at the large hadron collider (LHC), CERN is a multipurpose detector designed for testing the SM and also to carry out searches for phenomena taking place beyond SM (if there are any such phenomena), such as supersymmetric particle production at \sim TeV scale. At the LHC, proton-proton (pp) collisions take place at the center of mass energy of 13 TeV. Supersymmetric particles can be produced in these collisions if they exist and accessible at the LHC. In GMSB models, events with one or more photons, quarks of light flavor (up, down, charm and strange) or bottom flavor and missing transverse momentum are expected. Missing transverse momentum is the signature of weakly interacting LSPs (or neutrinos) in the detector which is nothing but the momentum imbalance in directions transverse to the colliding beams.

This thesis investigates the production of supersymmetric particles with at least one photon, light flavor or bottom flavor jets which originate from quarks and large missing transverse momentum using the data collected in the year 2016 with the CMS detector. Chapter 2 gives a very brief introduction to SM, its limitations and supersymmetric extensions of SM and GMSB models. Chapter 3 describes the experimental set up consisting of LHC and the CMS detector. I also discuss a new method to inter-calibrate short fibers of forward hadron calorimeter in this chapter. The analysis strategy and background estimation techniques are discussed in chapter 4. Results, summary and some possible extensions of the search are described in the final chapter 5.

Chapter 2

Standard model and supersymmetry

2.1 Standard model particles

The SM of particle physics consists of 3 *generations* of quarks and leptons (Table 2.1), gauge bosons which are mediators of strong, electromagnetic (EM) and weak force, and a scalar Higgs boson (Table 2.2).

TABLE 2.1: Leptons and quarks of SM with their properties

Leptons (spin $\frac{1}{2}$)					
Gen.	Particle	Charge	Mass (MeV)	Interactions ¹	Chiral state
1	ν_e	0	$< 2 \times 10^{-6}$	Weak	$\begin{bmatrix} \nu_e \\ e_L \end{bmatrix}, e_R$
	e	∓ 1	0.511	EM, Weak	
2	ν_μ	0	< 0.19	Weak	$\begin{bmatrix} \nu_\mu \\ \mu_L \end{bmatrix}, \mu_R$
	μ	∓ 1	105.7	EM, Weak	
3	ν_τ	0	< 18.2	Weak	$\begin{bmatrix} \nu_\tau \\ \tau_L \end{bmatrix}, \tau_R$
	τ	∓ 1	1777	EM, Weak	
Quarks (spin $\frac{1}{2}$)					
Gen.	Particle	Charge	Mass (MeV)	Interactions	Chiral state
1	u	$\pm \frac{2}{3}$	≈ 2.2	Strong, EM, Weak	$\begin{bmatrix} u_L \\ d_L \end{bmatrix}, u_R, d_R$
	d	$\mp \frac{1}{3}$	≈ 4.7		
2	c	$\pm \frac{2}{3}$	1.275×10^3		$\begin{bmatrix} c_L \\ s_L \end{bmatrix}, c_R, s_R$
	s	$\mp \frac{1}{3}$	≈ 95		
3	t	$\pm \frac{2}{3}$	173.1×10^3		$\begin{bmatrix} t_L \\ b_L \end{bmatrix}, t_R, b_R$
	b	$\mp \frac{1}{3}$	$\approx 4.18 \times 10^3$		

TABLE 2.2: Gauge bosons and higgs boson in SM with their properties

Particle	Charge	Mass (GeV)	Spin	Force mediation	Mixing fields
g	0	0	1	Strong	g
γ	0	0	1	EM	W_3, B
W	∓ 1	80.4	1	Weak	W_1, W_2
Z	0	91.2	1	Weak	W_3, B
H	0	125.2	0	-	H_u, H_d

Categorization of the quarks and leptons into 3 generations is done based on their masses [11] and properties. The first generation consists of lightest and the

¹All particles with non-zero mass have gravitational interactions. But gravity is not a part of SM.

third generation consists of heaviest particles. Neutrinos are grouped according to their interactions and their exact masses are unknown. The masses of SM particles are not predicted by the theory, but they are measured quantities in experiments. All the charged (in this thesis charge always refers to electric charge) particles can interact via EM force. Neutral leptons, neutrinos, are allowed to undergo only weak interactions. Quarks have an additional quantum number, color, which is responsible for strong interaction.

2.2 Conservation laws and symmetry

Various experimental observations in the realm of nuclear and elementary particle physics led to framing many laws of nature, which formed the basis for the development of the SM. Similar to the law of conservation of energy, linear momentum and angular momentum in basic physics, there are other laws of conservation such as charge, color charge, lepton number within each generation etc. Whenever there is a conservation law, then there is a symmetry associated with it and a symmetry also implies a conservation law. This relation between conservation law and symmetry is given by Noether's theorem [12]. Conservation of energy, linear momentum and angular momentum are connected with symmetry in time translation, space translation and rotation respectively. These symmetries can be represented mathematically using symmetry groups. For example, the group representing rotational symmetry is $SO(3)$.

Conservation of charge is associated with $U(1)$ global gauge symmetry. Under $U(1)$ group transformation, the wavefunction ψ of a charged particle transforms as $\psi \rightarrow U\psi$, where $U = e^{i\theta}$ and θ is a real number. This transformation is nothing but the change in phase of ψ . The Dirac Lagrangian is invariant under this transformation. When the local gauge transformation, $\theta(x, t)$ is imposed, the Dirac Lagrangian is no longer invariant. Dirac Lagrangian with local gauge invariance is the Lagrangian for quantum electrodynamics - Dirac fields of e^\pm interacting with Maxwell fields, photons [13]. In a similar way each of the forces described by the SM, has an associated symmetry group which describes the corresponding interactions.

2.3 Strong interactions

The strong interaction is mediated by gluons and the theory is described by quantum chromodynamics (QCD). The QCD is based on the symmetry group $SU(3)_C$, where C represents the associated quantum number, and is called color (red (R), green (G) or blue (B)), having 3 degrees of freedom and 8 generators or 8 gluon fields. This color has nothing to do with everyday color and its just an analogy for group transformations. Unlike the photons which are neutral (*chargeless*) the gluons carry color charge and they are:

$$R\bar{G}, R\bar{B}, G\bar{R}, G\bar{B}, B\bar{R}, B\bar{G}, \frac{1}{\sqrt{2}}(R\bar{R} - G\bar{G}), \frac{1}{\sqrt{6}}(R\bar{R} + G\bar{G} - 2B\bar{B})$$

$SU(3)_C$ is a non-abelian gauge group which means that the gluons have self interactions. Quarks carry one color charge (red green or blue) and gluons are bi-colored having one of the 8 colors mentioned above. All the observed hadrons and mesons are colorless ($C\bar{C}$ or RGB), in other words, isolated quarks or gluons are not observed

in nature. The strength of strong interaction increases with distance (or decreases with energy). At very large energy, the strength of strong interaction becomes very small and this behavior is named as asymptotic freedom [14][15]. As two quarks are separated from each other, quark-antiquark pair are created which results in formation of colorless mesons and hadrons.

2.4 Electro-weak interactions

The interaction between charged particles is described by quantum electrodynamics (QED) which is based on the symmetry group $U(1)$. The mediator of this interaction is massless spin-1 photon. Unlike QCD, there are no self interactions of the force mediator since photon does not carry any charge.

The neutral leptons, neutrinos, take part only in weak interactions whose description is based on $SU(2)_L$ symmetry. The mediators of this force are massive W and Z bosons. All the leptons and quarks of SM have weak interactions and neutrinos have only weak interaction. Weak theory is a chiral theory which implies that only left handed particles or right handed antiparticles participate in the interactions. A consequence of chiral theory is that there is no place for right handed neutrinos or left handed anti-neutrinos within the SM. In weak interactions, some of the quantum numbers need not be conserved, namely: parity (P), charge conjugation (C) and time reversal (T). However, there is no evidence for violation of these quantum numbers (C, P and T) in strong and EM interactions. The CPT as a whole is found to be conserved in all the three interactions.

At high energy, weak and EM interactions become indistinguishable and those interactions are described by electro-weak (EW) theory [1][16][17] which obeys the gauge group $SU(2) \otimes U(1)$.

2.5 The Higgs mechanism

Local gauge invariance demands spin-1 force mediators to be massless. Indeed, this is the case for QCD and QED in which gluon and photon are massless fields. But the weak force mediators W^\pm and Z bosons were predicted to be massive. Later, the experiments at CERN in 1983 [18][19][20][21] discovered these bosons and confirmed that they were massive. Based on the gauge principle, it is concluded that the observed γ , W^\pm and Z are mixtures of W_1 , W_2 , W_3 , and B fields,

$$W^\pm = (W_1 \mp iW_2)/\sqrt{2} \quad (2.1)$$

$$Z = -B \sin \theta_W + W_3 \cos \theta_W \quad (2.2)$$

$$\gamma = B \cos \theta_W + W_3 \sin \theta_W \quad (2.3)$$

where θ_W is called the weak mixing angle and B is such that its predictions are consistent with properties of γ [22]. To solve the problem of massive gauge bosons, a spontaneous symmetry breaking mechanism was proposed by Englert, Brout and Higgs [23][24] by which these gauge bosons can acquire mass through the interaction with a new scalar field, called the Higgs field. When the Higgs field gets non-zero vacuum expectation value, the gauge bosons acquire mass. The ratio of masses of W^\pm and Z boson is given by

$$M_W/M_Z = \cos \theta_W \quad (2.4)$$

The theory predicts a spin 0 quanta (particle) associated with the Higgs field. This particle was discovered at CERN by ATLAS and CMS experiments in 2012 [25][26] and its mass was found to be ≈ 125 GeV. The masses of quarks and leptons would have been zero, if there was no Higgs boson. If the interaction of particle is stronger with the Higgs field, then its mass is expected to be higher. Top quark is the highest mass particle in the SM and its coupling to Higgs is the strongest. The interaction term between fermions and H field is given by $\mathcal{L}_{\text{Yukawa}} = -\lambda_f \bar{\psi} \mathbf{H} \psi$ where ψ is the Dirac field of the fermion, \mathbf{H} is the Higgs field and λ_f is Yukawa coupling.

2.6 Limitations of SM

With the discovery of the Higgs (H) boson, the particle content of the SM is complete and we have a self-consistent theory which describes many of the experimental observations. Fig.2.1 shows production cross sections for various SM processes and the measurements by the CMS experiment. The agreement between experimentally measured cross section value and theoretically predicted value spans over 8-9 orders of magnitude!

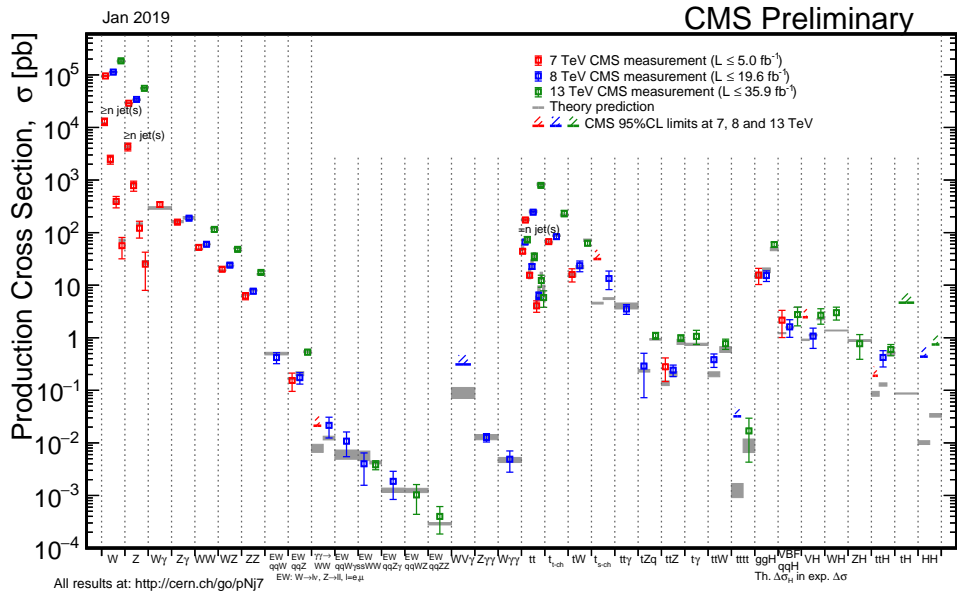


FIGURE 2.1: Summary of the cross section measurements of SM processes by CMS experiment [27].

Although H was the last piece in the SM puzzle and we have discovered it, there are many theoretical issues and experimental observations which are not explained by the SM. From the theoretical point of view, observed mass of H at 125 GeV itself is an issue and it is called as hierarchy problem which is discussed below. Some of the unsolved problems within SM framework are:

- The H boson gets corrections to its mass by loop diagram contributions, the largest contribution is coming from top quark loop diagram (Fig.2.2). This contribution is given by

$$\Delta m_H^2 = -\frac{|\lambda_t|^2}{8\pi^2} [\Lambda_{UV}^2 + \dots] \quad (2.5)$$

where λ_t is the top Yukawa coupling (~ 1) and Λ_{UV} is the ultraviolet cutoff scale above which SM is not valid and its value is close to the GUT (grand unified theory) scale², 10^{16} GeV or Planck scale, $> 10^{19}$ GeV. With these large corrections, the mass of H would have been $> 10^{16}$ GeV and not near 125 GeV. This is called hierarchy problem in SM. It is very *unnatural* to have a contribution $\sim 10^{16}$ GeV which cancels the effect shown in eqn.2.5 and get mass of Higgs as 125 GeV.

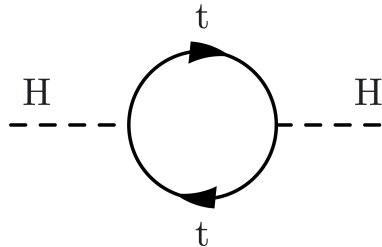


FIGURE 2.2: Top loop diagram contribution to H mass

- Gravitational interactions cannot be explained by the SM.
- Matter-antimatter asymmetry: We do not understand why we see more matter in the universe than antimatter today. At the early stages of universe, both of these must have been created in equal amount. There must be a mechanism by which matter started to dominate over antimatter.
- In SM masses of neutrinos is zero, whereas neutrino oscillations [28] indicate that they have nonzero mass.
- The universe comprises of 71.4% of dark energy, 24% of dark matter and only 4.6% is ordinary matter that we know. What is explained by SM is less than 5% of the total universe content.
- The strong, EM and weak gauge couplings are functions of energy scale. When these couplings are extrapolated to high energy, we expect all of them to unify at one energy. But this unification does not take place at one point within SM.

2.7 Supersymmetric extension of the SM

To overcome the limitations of the SM mentioned in Sec.2.6, we need extensions to SM which can address all (or some) of these issues without contradicting existing observations. One such extension is supersymmetry (SUSY) which can address some of the issues mentioned above, namely the dark matter problem, gauge coupling unification and hierarchy problem.

To tackle hierarchy problem, if we can introduce a new term in eqn.2.5 with similar correction but opposite sign, we might be able to get H mass around 125 GeV. Naively speaking, what SUSY does is exactly this - it introduces a scalar partner for every SM fermion and a fermionic partner for every bosonic SM particle and hence the corrections from superpartner loop diagrams cancel the corrections from SM particle loop diagrams. Superpartners of SM particles differ in spin by half a unit. For example, superpartner of top quark is top squark (or stop) with spin 0. The superpartners of bosons have spin $\frac{1}{2}$ and they are named with suffix *ino*, such as gluino,

²the scale at which the strength of EM, strong and weak force merge.

photino etc. Fig.2.3 shows the contributions to H mass from top loop and stop loop. The contribution from second loop diagram is given by eqn.2.6 which has similar form as eqn.2.5 but with an opposite sign.

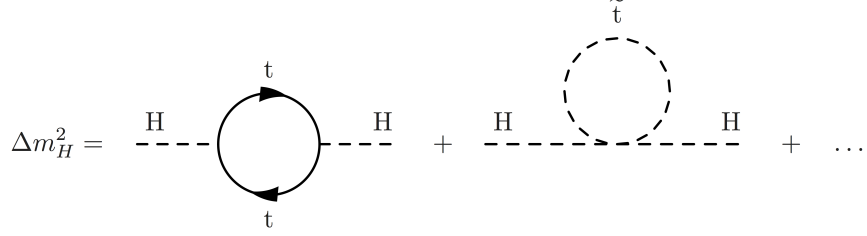


FIGURE 2.3: Corrections to H mass from top loop and stop loop.

$$(\Delta m_H^2)_{\text{SUSY}} = \frac{|\lambda_t|^2}{8\pi^2} [\Lambda_{UV}^2 + \dots] \quad (2.6)$$

We are interested in minimal supersymmetric extension of SM (MSSM) which is direct supersymmetrization of SM and has minimum number of new particle states and interactions consistent with phenomenology [29]. Table 2.3 shows fields corresponding to various particles in the MSSM. These superpartners listed are not necessarily the mass eigenstates of the theory because there can be mixing of gauginos and higgsinos [30]. The observable mass eigenstates are charginos or neutralinos, denoted by $\tilde{\chi}^{\pm, 0}$ and gluino which is not a mixture. Gauge and mass eigenstates in MSSM are listed in table 2.4.

TABLE 2.3: Chiral supermultiplets and gauge supermultiplets in the MSSM [30]

	spin 0	spin $\frac{1}{2}$
squarks, quarks (x3 families)	$(\tilde{u}_L \tilde{d}_L)$ \tilde{u}_R \tilde{d}_R	$(u_L d_L)$ u_R d_R
sleptons, leptons (x3 families)	$(\tilde{\nu} \tilde{e}_L)$ \tilde{e}_R	(νe_L) e_R
Higgs, higgsinos	$(H_u^+ H_u^0)$ $(H_d^0 H_d^-)$	$(\tilde{H}_u^+ \tilde{H}_u^0)$ $(\tilde{H}_d^0 \tilde{H}_d^-)$
	spin $\frac{1}{2}$	spin 1
gluino, gluon winos, W bosons bino, B boson	\tilde{g} $\tilde{W}^\pm \tilde{W}^0$ \tilde{B}^0	g $W^\pm W^0$ B^0

Since we have not observed supersymmetric particles at the same mass SM counterparts, SUSY is a broken symmetry and the masses of sparticles are larger than SM partners. The effective Lagrangian can be written as

$$\mathcal{L} = \mathcal{L}_{\text{SUSY}} + \mathcal{L}_{\text{soft}} \quad (2.7)$$

The first term on RHS of eqn.2.7 preserves SUSY and contains gauge and Yukawa interactions. The second term breaks SUSY and contains mass terms and coupling parameters which should vanish at very high mass scale at which SUSY is unbroken. There are multiple ways to break SUSY and some of the popular ways are, gravity

TABLE 2.4: Gauge and mass eigenstates of MSSM [30][31]

Names	Spin	Gauge eigenstates	Mass eigenstates
squarks	0	$\tilde{u}_L \tilde{u}_R \tilde{d}_L \tilde{d}_R$	same
		$\tilde{c}_L \tilde{c}_R \tilde{s}_L \tilde{s}_R$	same
		$\tilde{t}_L \tilde{t}_R \tilde{b}_L \tilde{b}_R$	$\tilde{t}_1 \tilde{t}_2 \tilde{b}_1 \tilde{b}_2$
sleptons	0	$\tilde{e}_L \tilde{e}_R \tilde{\nu}_e$	same
		$\tilde{\mu}_L \tilde{\mu}_R \tilde{\nu}_\mu$	same
		$\tilde{\tau}_L \tilde{\tau}_R \tilde{\nu}_\tau$	$\tilde{\tau}_1 \tilde{\tau}_2 \tilde{\nu}_\tau$
neutralinos	$\frac{1}{2}$	$\tilde{B}^0 \tilde{W}^0 \tilde{H}_u^0 \tilde{H}_d^0$	$\tilde{\chi}_1^0 \tilde{\chi}_2^0 \tilde{\chi}_3^0 \tilde{\chi}_4^0$
charginos	$\frac{1}{2}$	$\tilde{W}^\pm \tilde{H}_u^\pm \tilde{H}_d^\mp$	$\tilde{\chi}_1^\pm \tilde{\chi}_2^\pm$
gluino	$\frac{1}{2}$	\tilde{g}	same
Higgs bosons	0	$\tilde{H}_u^0 \tilde{H}_d^0 \tilde{H}_u^+ \tilde{H}_d^-$	$h^0 H^0 A^0 H^\pm$
gravitino	3/2	\tilde{G}	same

mediated or Planck scale mediated SUSY breaking (PMSB), anomaly mediated SUSY braking (AMSB) and gauge mediated SUSY breaking (GMSB). A brief discussion on GMSB is given in section 2.8 to motivate the search for SUSY with photon which is the topic of this thesis.

2.7.1 R-parity

A multiplicative quantum number called *R-parity* is introduced for every particle and sparticle to account for very strong experimental bounds on proton lifetime. The proton lifetime is $> 10^{33}$ years [32] which is larger than the age of the universe. R-parity is defined as

$$P_R = (-1)^{3(B-L)+2s} \quad (2.8)$$

where s is the spin, B and L are baryon number and lepton number respectively. All SM particles have even R-parity, $P_R = +1$ and supersymmetric particles have odd R-parity, $P_R = -1$. If R-parity is not conserved, then $p \rightarrow e^+ \pi^0$ via anti-squark mediation as shown in Figure 2.4.

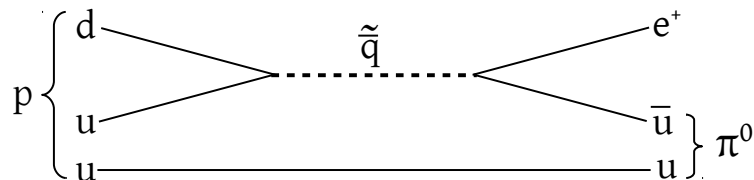


FIGURE 2.4: One of the possible modes for decay of proton via anti-squark mediation if R-parity is not conserved.

Important consequences [30] of R-parity conservation are:

- Supersymmetric particles are always produced in pairs in collider experiments and any supersymmetric particle decay should involve odd number of daughters. In other words, at any vertex, there should be even number of supersymmetric particles.

- Lightest supersymmetric particle (LSP) must be stable. If LSP is neutral and weakly interacting, then it could serve as a dark matter candidate and account for 24% (or some part of 24%) of the universe content [33].
- All the non-LSP supersymmetric particle decay chains must result in odd number (usually 1) of LSPs.

2.8 Gauge mediated SUSY breaking

In GMSB scenarios [34, 35, 36, 37, 38, 39], the communication between hidden sector, where SUSY breaking takes place, and the visible MSSM sector (consisting of chiral supermultiplets shown in table 2.4) is via the ordinary gauge interactions. In comparison with other SUSY breaking scenarios, flavor changing processes and new sources of CP violation are naturally suppressed [34] in GMSB. The messengers communicating between MSSM and hidden sector also have $SU(3)_C \otimes SU(2)_L \otimes U(1)_Y$ interactions. The soft terms in MSSM come from loop diagrams involving these messengers, whose value is given by

$$m_{soft} \sim \frac{\alpha_a}{4\pi} \frac{\langle F \rangle}{M_{mess}} \quad (2.9)$$

where $\alpha_a/4\pi$ is loop factor for Feynman diagrams involving gauge interactions, F relates to the SUSY breaking scale and M_{mess} is the messenger mass scale [30].

GMSB permits a significantly lower symmetry-breaking scale ($\langle F \rangle$) than, e.g., gravity mediation, and therefore generically predicts that the gravitino (\tilde{G}) is the LSP [37, 40, 41] whose mass is given by

$$m_{\tilde{G}} \sim \langle F \rangle / M_P \sim \text{keV} \quad (2.10)$$

where M_P is the Planck scale where gravity is expected to become strong.

2.8.1 Phenomenology of GMSB

As mentioned above, gravitino (\tilde{G}), superpartner of graviton, is the LSP, it is stable and weakly interacting and results in missing transverse momentum. The next-to-LSP (NLSP) is either a neutralino ($\tilde{\chi}_1^0$) or a chargino ($\tilde{\chi}_1^\pm$). The decay modes of the NLSP are decided by the manner in which bino, wino and higgsino components mix, and hence define the nature of this mass eigenstate [42].

- For a **bino like** NLSP, $|M_1| < |\mu|, |M_2|$, where M_1, M_2 and μ are $U(1)$ gauge mass parameter, $SU(2)$ gauge mass parameter and higgsino mass parameter respectively. The decay mode of NLSP is $\gamma/Z + \tilde{G}$ with larger branching ratio (BR) for $\gamma + \tilde{G}$. The left plot in Fig.2.5 shows BR for NLSP decay as a function of bino mass [43].

It is worth noting that the coupling of γ with \tilde{G} is at the tree-level because the gravitino has become massive after SUSY breaking and it has goldstino component [30].

Experimentally, these kind of scenarios can be targeted using collider searches with $\gamma\gamma + p_T^{miss}$ or $\gamma + p_T^{miss}$ final states, where p_T^{miss} is the magnitude of missing transverse momentum.

- For a **wino like** NLSP, $|M_2| < |\mu|, |M_1|$. In this case, $\tilde{\chi}_1^0$ and $\tilde{\chi}_1^\pm$ are nearly mass degenerate and the decay modes are

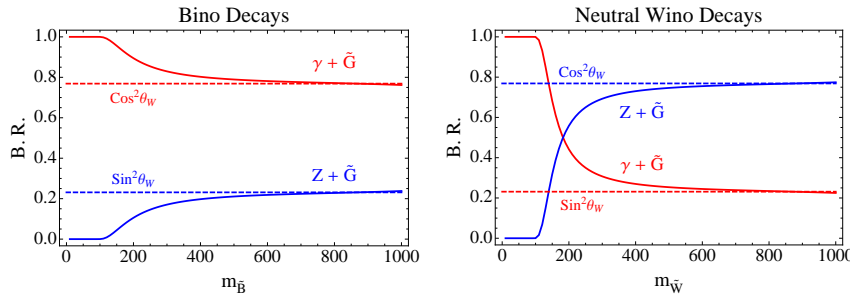


FIGURE 2.5: BR for bino and neutral wino NLSP decays. Plot is taken from Ref.[43]

$$\begin{aligned}\tilde{\chi}_1^\pm &\rightarrow W^\pm + \tilde{G} \\ \tilde{\chi}_1^0 &\rightarrow Z/\gamma + \tilde{G}\end{aligned}$$

The right plot in Fig.2.5 shows BR for $\tilde{\chi}_1^0$ decay as a function of wino mass [43]. These scenarios can result in signatures with lepton + $\gamma + p_T^{miss}$.

- For a **higgsino like** NLSP, $|\mu| < M_1, M_2$ and different NLSP decay modes are preferred depending on the value of μ .
If $\mu < 0$, then $\tilde{\chi}_1^0 \rightarrow H/\gamma + \tilde{G}$ decay is preferred.
If $\mu > 0$, then $\tilde{\chi}_1^0 \rightarrow Z/\gamma + \tilde{G}$ decay dominates.
Models with higgsino like NLSP may result in $b\bar{b}$, coming from H decay, and $\gamma + p_T^{miss}$ final states.

2.8.2 Simplified GMSB models

There are many free parameters in the theory and it is difficult to predict which exact set of parameters is realized in nature. Also, many of these possible parameter sets can give rise to similar experimental signatures. A realistic SUSY scenario, if exists and accessible at the LHC, would give signature as one or more of the following event topologies - 0 lepton, 1 lepton, 2 leptons, multiple leptons, at least one photon and 0 lepton, 2 photons and 0 lepton, 1 lepton and at least one photon, high p_T^{miss} and multiple jets. In order to cover the maximum possible theoretical phase space, the searches at CMS are designed based on these final state signatures. Once the final state is decided, certain assumptions are made on the models and they are called as simplified model scenarios (SMS) [44, 45, 46, 47, 48] which are used to design SUSY searches.

For example, one of the SMS considered in this thesis is shown in Figure 2.6. In

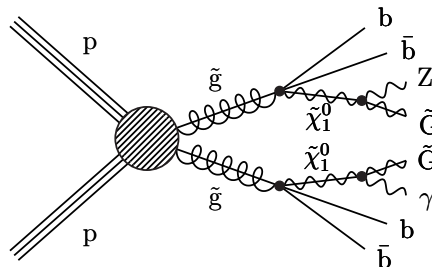


FIGURE 2.6: SMS diagram showing decay of gluino to $b\bar{b}$ and $\tilde{\chi}_1^0$. Then, $\tilde{\chi}_1^0$ decays to \tilde{G} and γ/Z .

this case, we have assumed

- Production of sparticles, pair of gluinos here, is completely defined by the QCD theory and parton distribution functions (which in turn depends on centre-of-mass energy of the colliding protons).
- All sparticles, except gluino, $\tilde{\chi}_1^0$ and \tilde{G} are very heavy and not accessible at the LHC.
- Branching fractions of the decay of sparticles to various channels are simplistically decided:

Gluino decays to $b\bar{b}$ and $\tilde{\chi}_1^0$ with 100% branching ratio (BR).

$\tilde{\chi}_1^0$ decays to $\tilde{G} + \gamma$ or $\tilde{G} + Z$ with 50% BR each.

A typical signature of this model is large p_T^{miss} , many jets and b-jets and photon. A realistic GMSB SUSY model is more complicated with many free parameters and designing a search is very difficult in those cases. If the GMSB scenario is realized in nature and gives similar final states as the one shown in Figure 2.6, then this search might be able to discover it. On the other hand, if the final state is different than what is studied here, other searches would be able to discover it. In this way it is possible to explore large phase-space easily and increase the chances of discovery. Another advantage in using SMS is that it is easy to re-interpret the results by taking a different SUSY model.

Chapter 3

The Experimental Setup

3.1 The large hadron collider

The large hadron collider (LHC) is a circular particle accelerator and collider with a 27 km circumference. The LHC is designed to accelerate protons at an energy of 7 TeV [49] and peak luminosity of about $10^{34} \text{ cm}^{-2}\text{s}^{-1}$. The LHC started its proton-proton collisions in the year 2010 with an energy of 3.5 TeV per proton beam. Later the energy was increased to 4 TeV per beam and the data was collected till early 2013. This period from 2008 - 2013 is referred to as run 1 of the LHC. One of the main reasons for starting the LHC was to discover the last missing piece of the SM, Higgs boson. This was achieved by the CMS and ATLAS collaborations [25][26] in the year 2012. The other goal of the LHC is to answer some of the fundamental questions in physics: are there any new particles yet to be discovered? Is the SM valid at TeV scale? Are there any extra dimensions? What is the nature of dark matter and can it be produced at the LHC? During the period 2013 - 2015 LHC was upgraded and

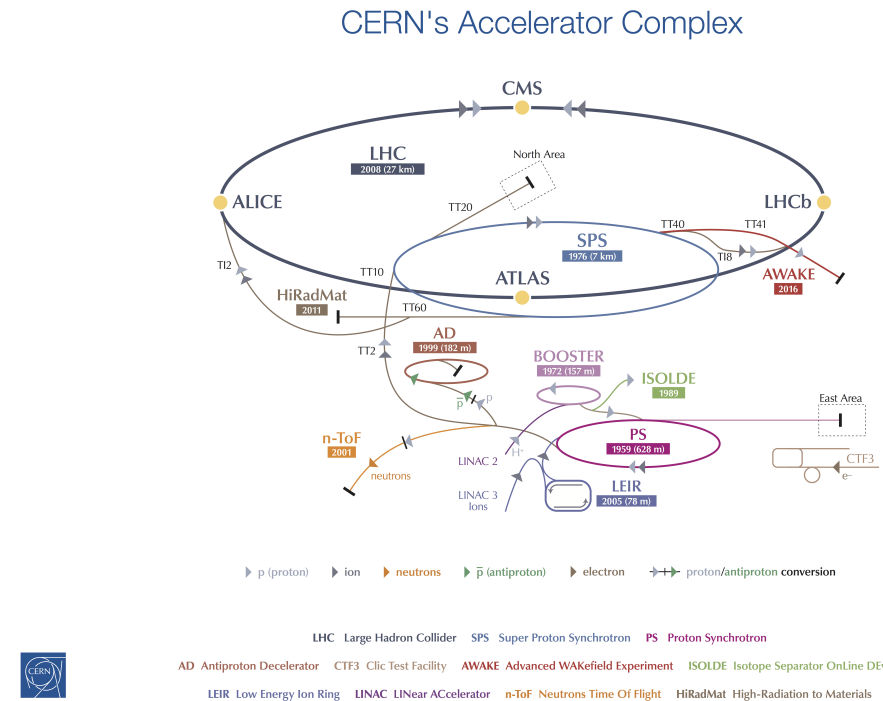


FIGURE 3.1: CERN accelerator complex

started with run 2 (2016 - 2018), in which each beam of protons were accelerated to an energy of 6.5 TeV and the total center of mass energy (\sqrt{s}) of collision was 13

TeV. The process of achieving $\sqrt{s} = 13$ TeV is done using various stages of CERN (European Organization for Nuclear Research) accelerator complex [50] shown in Fig.3.1.

Hydrogen gas is injected into duoplasmatron in which electrons from a hot cathode are used to break H₂ molecules and form H⁺ ions or protons. The protons are accelerated to 50 MeV using a linear accelerator (LINAC2). Next stage of acceleration is carried out by proton synchrotron booster (PSB) to reach 1.4 GeV. Proton synchrotron (PS) further accelerates protons to 25 GeV. In the PS, 25 ns bunch spacing is established, and PS also shortens the bunches so that they can be injected into super proton synchrotron (SPS). In the SPS protons reach energy of 450 GeV and finally they enter into the LHC ring. The LHC also accelerates heavy ions (Pb, Ar and Xe) apart from protons, but in the context of this thesis only protons are relevant.

In the LHC, 16 radio frequency (RF) cavities are used to accelerate protons. These RF cavities operate at a frequency of 400 MHz. Protons get accelerated from 450 GeV to 6.5 TeV in around 20 minutes, after passing through the cavities more than 10⁷ times. When the beam has reached right energy, an ideally timed protons do not get accelerated, whereas the protons with slightly different energy arriving early or later get accelerated or decelerated. In this way the beam is sorted into bunches and each bunch contains protons of required energy.

If the colliding beams are of the type particle-antiparticle, magnetic field in one direction can be used to bend the beams in opposite directions. Since LHC collides particle-particle beams, a twin-bore magnetic system is used instead of having two separate rings.

To steer the beam and keep in circular path, 1232 dipole magnets are used. Each of these magnets are about 15m long and made up of Niobium-Titanium (NbTi) superconducting coils. NbTi has critical temperature, T_C of 10 K and it is operated at 1.9 K. A current of 11.08 kA in these coils generates a magnetic field of 8.3 T.

Quadrupoles are used to focus the beam either horizontally or vertically. They have 4 magnetic poles arranged symmetrically around the beam pipe and also equipped with sextupole, octupole and decapole magnets to correct for small imperfections in the magnetic field.

The beams cross each other at 4 points where ALICE, ATLAS, CMS and LHCb detectors are located. Before the collision, the beams are made narrower down to 16 μm using a set of quadrupoles magnets. Table 3.1 shows various parameters of the LHC.

3.1.1 Luminosity

The number of events, N_{events} , expected for a process having cross section, σ , is given by

$$N_{events} = \sigma \int L dt \quad (3.1)$$

where L is the instantaneous luminosity and it is a property of the accelerator. The integrated term is referred to as integrated luminosity, \mathcal{L} and it is generally expressed in units of fb^{-1} (1 barn, 1 b = 10⁻²⁴ cm²). If there are n_b bunches per beam and each beam has a transverse spread of ρ_x, ρ_y in x and y directions at the interaction point, each bunch contains N protons, f is the frequency of revolution, then

$$L = \frac{n_b N^2 f}{4\pi \rho_x \rho_y} \quad (3.2)$$

TABLE 3.1: The LHC parameters [51]

Quantity	Value
Circumference	26.659 km
Dipole operating temperature	1.9 K (-271.3 °C)
Number of magnets	9593
Number of main dipoles	1232
Number of main quadrupoles	392
Number of RF cavities	8 per direction
Energy of protons (year 2016-2018)	6.5 TeV
Peak magnetic dipole field	7.74 T
Distance between bunches	~ 7.5 m
Peak luminosity (protons)	$\sim 1.2 \times 10^{34} \text{ cm}^{-2} \text{s}^{-1}$
No. of bunches per proton beam (design value)	2808
No. of protons per bunch (at start)	1.2×10^{11}
Number of turns per second	11,245
Number of collisions per second	10^9

At the LHC, beams do not collide head-on and this expression does not account for the beam crossing angle. It also assumes that the bunches are identical in transverse profile, have a Gaussian profile and independent of position along the bunch, and particle distributions remain same during bunch crossing [52].

The maximum instantaneous luminosity delivered by the LHC in the year 2016 was $\approx 1.5 \times 10^{34} \text{ cm}^{-2} \text{s}^{-1}$ [53] (which is more than the design value of $10^{34} \text{ cm}^{-2} \text{s}^{-1}$), and the total integrated luminosity is about 40 fb^{-1} . The total integrated luminosity

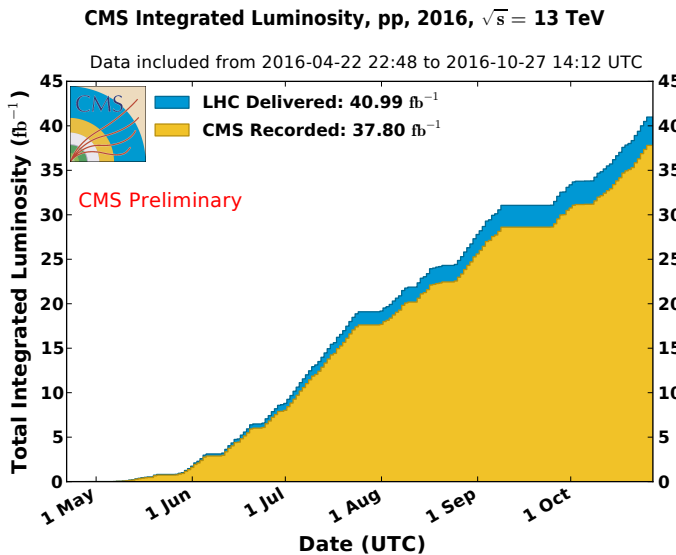


FIGURE 3.2: Total integrated luminosity as delivered by the LHC and recorded by CMS as a function of time.

(\mathcal{L}) as delivered by the LHC and recorded by the CMS detector as a function of time is shown in Fig. 3.2 for the year 2016 [53]. The total data certified as good for physics analysis corresponds to $\mathcal{L} = 35.9 \text{ fb}^{-1}$.

3.2 The compact muon solenoid

Surrounding one of the collision points of LHC is the compact muon solenoid (CMS) detector. The CMS is a general purpose detector designed to search for new phenomena, test the SM and to study properties of Higgs boson. It is a cylindrical superconducting solenoid providing 3.8 T axial magnetic field and has inner diameter of 6 m. Detailed description of the CMS detector can be found in [54]. Various sections of the CMS detector are shown in Fig. 3.3.

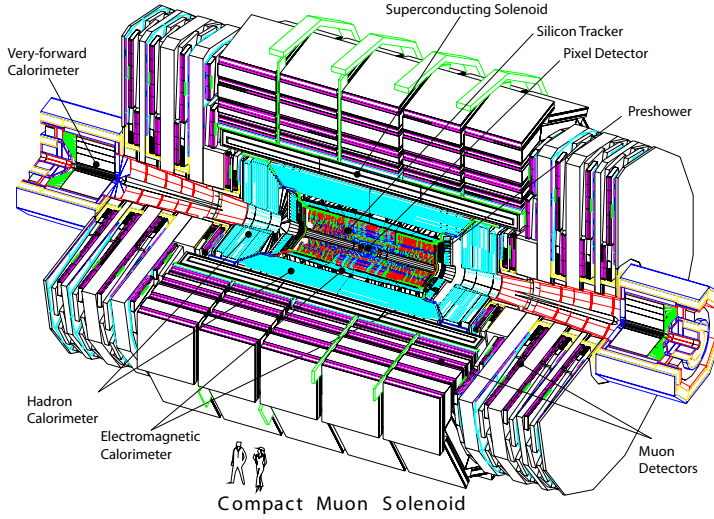


FIGURE 3.3: A view of the CMS detector [54].

3.2.1 CMS coordinate system

A right handed cartesian coordinate system adopted by the CMS has origin at the nominal collision point. The x -axis points towards inner side of the LHC ring, y points upwards and z axis is along the beam direction. The azimuthal angle ϕ is measured from x -axis in $x - y$ plane and r is the radial distance. Psudorapidity is defined as $\eta = -\ln(\tan(\theta/2))$, where θ is the polar angle measured from z -axis. Psudorapidity is an approximation of rapidity variable defined as $\frac{1}{2} \ln((E + p_z)/(E - p_z))$ in the limit $E \approx |\mathbf{p}|$, where E and \mathbf{p} are energy and momentum respectively. Some of the other quantities which are used in this work are listed below.

$$\text{Momentum transverse to beam direction } p_T = \sqrt{p_x^2 + p_y^2} \quad (3.3)$$

$$\text{Distance in } \eta - \phi \text{ plane, } \Delta R = \sqrt{(\Delta\eta)^2 + (\Delta\phi)^2} \quad (3.4)$$

3.2.2 Superconducting magnet

The 12.5 m long superconducting magnet in the CMS detector is made up of NbTi coil and capable of providing magnetic field up to 4 T (operated to provide 3.4 T). To achieve some of the goals of the LHC physics program, it is required to have a good momentum resolution of muons and other charged particles, tag tau leptons and b-quark jets etc. The magnetic field plays a crucial role in measuring the momentum of charged particles by the tracker and outer muon systems, and also in identifying

the charge of particles. The magnetic flux returns through a 10 kilo-ton iron yoke. Total energy stored in the magnet is 2.6 GJ at 4 T magnetic field and the energy stored per unit cold mass is 11.6 kJ/kg which is higher than the values of any of the magnets used in particle physics detectors.

3.2.3 Inner tracking system

The tracking system is used to measure the momentum of the charged particles, determine their trajectory and to help in locating primary pp collision vertices and vertices of certain particle decays (secondary vertices). At a luminosity of $10^{34} \text{ cm}^{-2}\text{s}^{-1}$, on an average 1000 particles pass through the tracker every 25 ns. Tracker uses about 200 m^2 of Si, has length of 5.8 m and diameter of 2.5 m and covers up to $|\eta| = 2.5$.

TABLE 3.2: Characteristics of subsystems of tracker. Pitch for the strip tracker refers to the distance between neighboring strips

Subsystem	Layers	Location (cm)	Pitch	Position resoln.
Pixel barrel	3 cylindrical	$r : 4.4 - 10.2$	$100 \times 150 \mu\text{m}^2$	$10 \mu\text{m}$ in trans.
Pixel endcap	2 disks	$z : 34.5 - 46.5$		$20 - 40 \mu\text{m}$ longt.
TIB	4 cylindrical	$r : 20 - 55$	$80 - 120 \mu\text{m}$	$13 - 38 \mu\text{m}$ in $r\phi$
TOB	6 cylindrical	$r : 55 - 116$	$122 - 183 \mu\text{m}$	$18 - 47 \mu\text{m}$ in $r\phi$
TID	3 disks	$z : 58 - 124$	$100 - 141 \mu\text{m}$	$13 - 38 \mu\text{m}$ in $r\phi$
TEC	9 disks	$z : 124 - 282$	$97 - 184 \mu\text{m}$	$18 - 47 \mu\text{m}$ in $r\phi$

It is composed of inner pixel detector consisting of 3 layers at radii 4.4 cm, 7.3 and 10.2 cm in the barrel region. The other component is the Si strip tracker which extends up to 1.1 m in barrel region with 10 layers in it. On either side of the barrel are the endcaps which have 2 disks in the pixel detector and 3 plus 9 disks in the strip tracker. There are in total 1440 modules in pixel detector with 66 million pixels; 15148 modules in strip tracker with 9.3 million strips. A part of cross sectional schematic view of the tracker [55] is shown in Fig. 3.4 with different modules namely: pixel, inner barrel (TIB), outer barrel (TOB), inner disks (TID) and endcaps (TEC). The

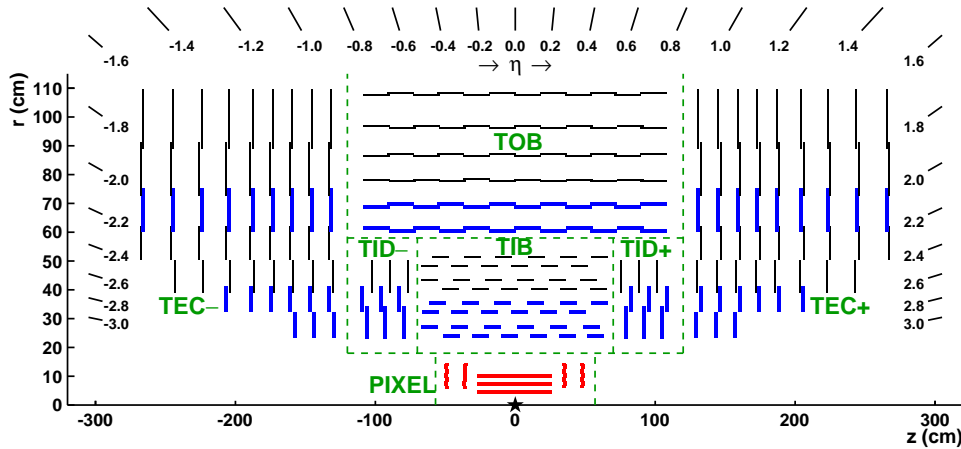


FIGURE 3.4: A schematic view of the CMS tracker in $r - z$ plane showing different modules [55]. The tracker is symmetric about $r = 0$ line and the figure shows only the upper part.

hit position resolution provided by the pixel detector is about $10 \mu\text{m}$ and $20-40 \mu\text{m}$

in transverse and longitudinal coordinate respectively and the third coordinate is determined from the sensor plane position.

The pixel and some of the strip modules (shown in thick blue lines in Fig.3.4) are capable of providing 3-D hits and the strip modules which provide 2-D hits are shown in thin black line in the figure. The strip modules which provide 3-D hits consist of 2 back-to-back strips in them.

Performance of tracker

Figure 3.5 shows the resolution of various quantities for single muons of p_T 1, 10 and 100 GeV as a function of $|\eta|$.

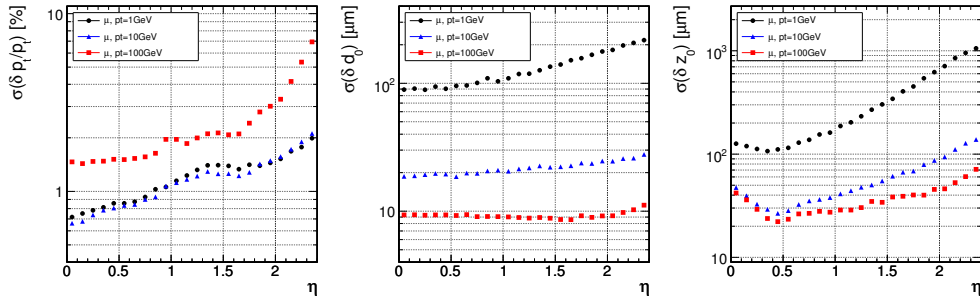


FIGURE 3.5: Resolution of various track parameters for muons with $p_T = 1$ GeV (black), 10 GeV (blue) and 100 GeV (red) . Left plot shows p_T resolution, middle plot shows transverse impact parameter resolution and right plot shows longitudinal impact parameter resolution [54].

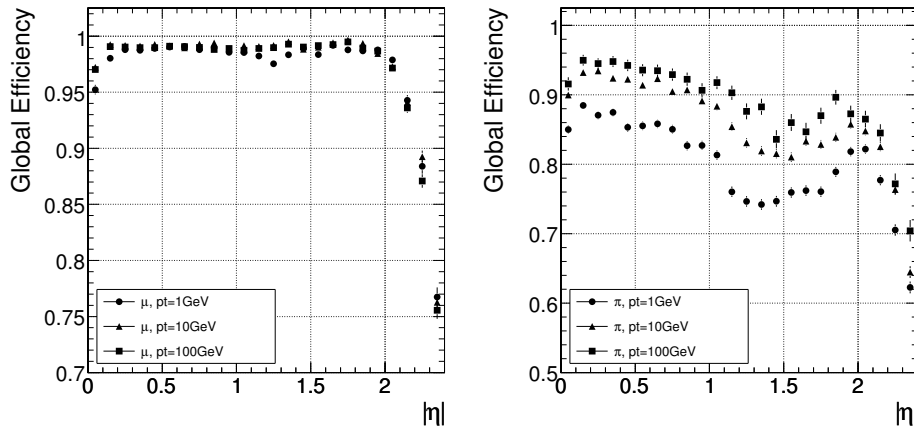


FIGURE 3.6: Global track reconstruction efficiency for muons (left) and pion (right) with p_T of 1, 10 and 100 GeV [54].

For 100 GeV muons, p_T resolution is about 1-2% up to $|\eta| \approx 1.6$. For lower p_T muons, resolution mainly is affected by multiple scattering and for high p_T this effect is about 20-30%. Multiple scattering of low p_T muons degrades the impact parameter resolution as well and this effect is reduced for high p_T muons and hence these have better impact parameter resolution.

Track reconstruction efficiency is about 99% for muons with p_T in the range 1-100 GeV (left plot in Fig.3.6) and slight degradation for some $|\eta|$ regions is because

of gaps or non-coverage of the tracker. For charged pions (right plot in Fig.3.6) the efficiency is lower because of interactions with the materials of the tracker.

Thickness t of the tracker in terms of radiation length, X_0 (left) and interaction length, λ_I (right) is shown in Fig.3.7 along with the supporting systems and beam pipe contributions using simulation. An ideal tracker should have very small X_0 and λ_I so that the particles passing through it do not deposit significant energy or do not start showering in the tracker.

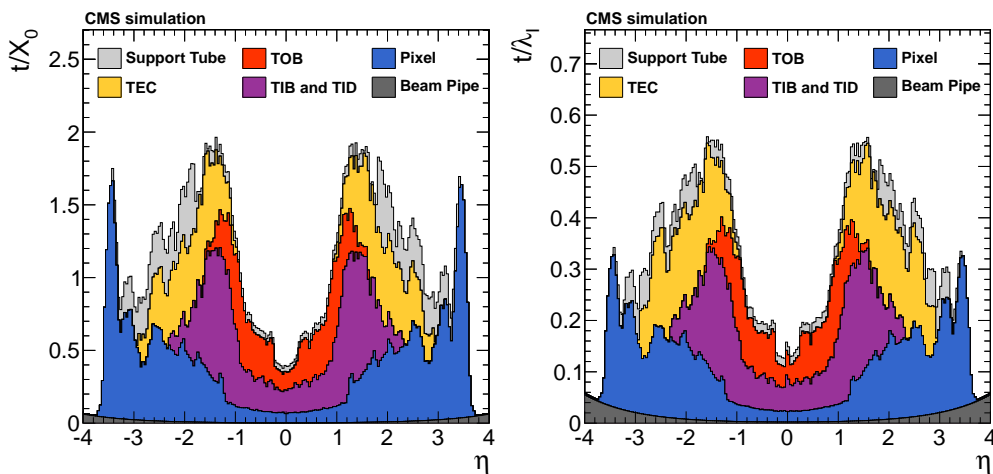


FIGURE 3.7: Thickness of tracker along with beam pipe and supporting systems in terms of radiation length, X_0 (left) and interaction length, λ_I (right) [55].

3.2.4 Electromagnetic calorimeter

The EM calorimeter (ECal) of CMS is a hermetic, compact, granular, homogeneous, radiation tolerant and total absorption calorimeter made up of lead tungstate crystals (PbWO_4). It measures energy of photons, electrons, EM component of jets and hadrons which deposit their energy in ECal. It has large dynamic range coupled with excellent linearity up to 1 TeV. It also provides triggering information and aids particle identification. The region with $|\eta| \leq 1.48$ is covered by barrel (EB) and $1.48 < |\eta| < 3$ region is covered by two endcap (EE) calorimeters. To identify neutral pions (π^0), a preshower (ES) detector is used in the endcaps with $1.653 < |\eta| < 2.6$. The radiation length of EB is $26X_0$, EE is $25X_0$ and that of ES is $3X_0$.

Incident electrons and photons produce EM showers which spread laterally over several crystals. Charged particles in these showers produce blue-green scintillation light (420-430 nm) and the amount of light is proportional to the incident particle energy. About 80% of the scintillation light is emitted in 25 ns. The crystals have radiation length of 0.89 cm and small Molière radius (2.2 cm) which help in containing showers in smaller volume. The scintillation light is collected by avalanche photo-diodes (APDs) in case of EB and vacuum photo-triodes (VPTs) in case of EE.

Fig.3.8 (left) shows the schematic layout of ECal modules, supermodules and supercrystals. The granularity of crystals in EB is 0.0174×0.0174 in $\eta - \phi$. Two rows of 5 crystals form a submodule, A supermodule is formed using 4 modules. Almost all the crystal axes are tilted by 3° with respect to the line from nominal interaction point in both η and ϕ directions to avoid any particle passing directly through the gap between crystals.

The ES detector consists of 2 lead radiators followed by a set of Si microstrips each and the strips are orthogonal to each other. The granularity of the Si detector helps in identifying 2 photons coming from a π^0 decay or a Higgs decay.

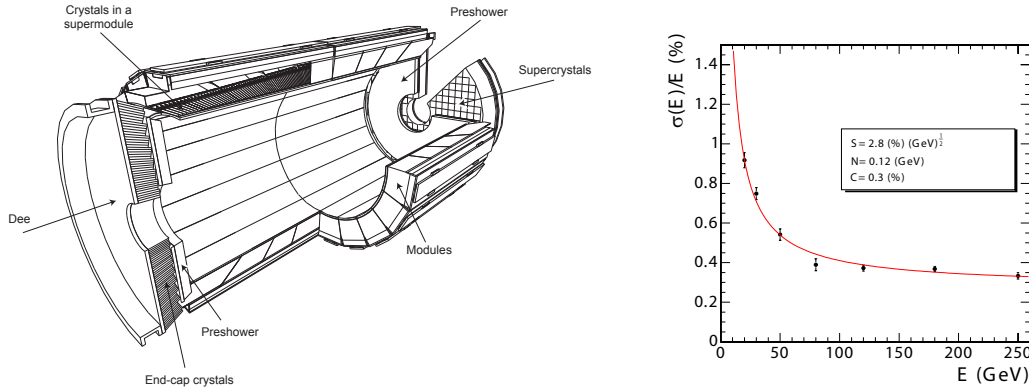


FIGURE 3.8: A schematic of ECal showing different components is shown on the left. Right plot shows resolution of ECal as a function of electron energy using test beam studies [54].

The energy resolution of ECal is given the expression,

$$\left(\frac{\sigma}{E}\right)^2 = \left(\frac{S}{\sqrt{E}}\right)^2 + \left(\frac{N}{E}\right)^2 + C^2 \quad (3.5)$$

where S is the stochastic term, N is the noise term and C is the constant term. Typical values after summing energy in 3×3 crystals are $S = 2.8\%$, $N = 0.12$, $C = 0.3\%$. The resolution as a function of electron energy, E measured in GeV is shown in Fig.3.8 using test beam studies. The EM shower of electrons and photons is similar and it consists of several bremsstrahlung radiations and e^+e^- pair productions. Event to event shower fluctuations in the lateral shower containment and photo-statistics affect S term in the energy resolution. If there is a preshower detector, then fluctuations in energy deposited in the absorber with respect to energy in the Si detector also contributes to S . For C the contributors are non-uniformity of longitudinal light collection, intercalibration errors and energy leakage from the back of the crystal. Noise from electronics, digitization and pileup contribute to noise term, N .

A laser monitoring system is used to measure the transparency loss in the crystals which occurs because of radiation damage. This system uses blue laser of wavelength 440 nm which is closer to the scintillation peak and the intensity of the output light from each of the crystals is used to correct the transparency loss and re-calibrate the crystals.

3.2.5 Hadron calorimeter

This calorimeter (HCal) is a sampling calorimeter which measures energy of the charged and neutral hadrons and extends up to $|\eta| = 5.2$. It is divided into barrel (HB), endcap (HE), forward calorimeter (HF) and outer calorimeter (HO).

The pseudorapidity coverage of HB is $|\eta| < 1.3$ with a granularity width of 0.087 in both η and ϕ . This sampling calorimeter has alternating brass (70% Cu and 30% Zn) absorber and plastic scintillators. The absorber thickness is $5.82\lambda_I$ at 90° and $10.6\lambda_I$ at $|\eta| = 1.3$. The ECal in front of HB has $1.1\lambda_I$. Fig.3.9 shows a schematic diagram of one quarter slice of HCal. Because of space constraint from the magnet,

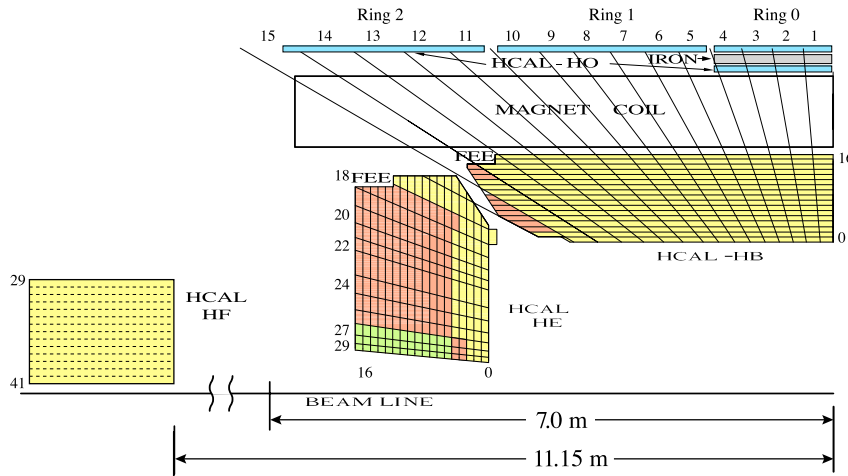


FIGURE 3.9: A schematic diagram of one quarter slice of HCAL showing HB, HE, HO and HF along with location of front end electronics (FEE) of HB and HE. The colors represent longitudinal readout scheme.

HB thickness in the low $|\eta|$ region is kept small, and to record the leakage of hadronic showers, 5 rings of HO are placed outside the magnet and the center of these 5 rings are at $z = 0, \pm 2.686$ m and ± 5.342 m. The total depth of the calorimeter system is at least $11.8\lambda_I$ including HO. About 5% of all hadrons of energy more than 100 GeV deposit energy in HO.

The scintillation light is collected by the wavelength shifting (WLS) optical fiber which is laid out on the edge of the scintillator tile. WLS fiber is spliced into clear fiber and the light is guided to hybrid photo-diode (HPD) using optical cable. HF uses Cherenkov based quartz fibers instead of scintillators and light from the quartz fibers is fed into photo-multiplier tubes (PMTs). More details about HF is discussed in later part of this chapter.

The signals from HPDs or PMTs are read by charge integration and encoding (QIE) chips. The QIE is an ADC which provides almost constant precision over large range by assigning different number of bits to different amounts of charge (which is proportional to energy) collection.

All of the subsystems have LEDs and lasers for the purpose of calibration and monitoring. Except HO, other subsystems are also equipped with radioactive source tubes.

The resolution of HCAL and ECAL setup was determined using test beam setup and it found to be of the form:

$$\frac{\sigma}{E} = \frac{a}{\sqrt{E}} \oplus b \quad (3.6)$$

where a is stochastic term of value 0.847 ± 0.016 $\text{GeV}^{\frac{1}{2}}$ and b is a constant term of value 0.074 ± 0.008 for HB and HE. For HF, $a = 1.98\text{GeV}^{\frac{1}{2}}$ and $b = 0.09$ [56].

A study on HF calorimeter performance in 2016 using energy deposits in HF quartz fibers is described in 3.3.

3.2.6 Muon chambers

Muons are detected using gas filled chambers located outside the magnet. The direction of magnetic field is opposite in direction to that of the field inside the magnet. The muon chambers have the task of identifying momentum of muons, type of charge and provide triggering information. This system consists of barrel region, up to $|\eta| = 1.2$, made up of drift tubes (DT) and two endcaps on either side, covering $0.9 < |\eta| < 2.4$, made up of cathode strip chambers (CSC). Resistive plate chambers (RPSc) are mounted in both barrel and endcap and operated in avalanche mode. They are capable of providing excellent timing resolution needed for muon triggers and they cover $|\eta| < 1.9$. Fig.3.10 shows a quarter of CMS detector with different muon chambers and their respective locations [57].

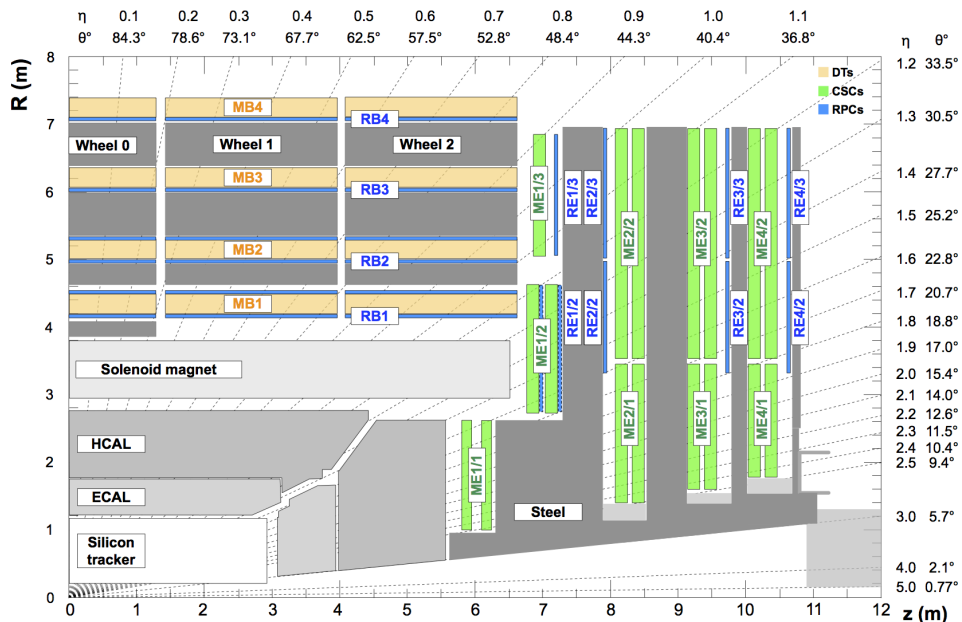


FIGURE 3.10: Schematic diagram of a quarter of CMS detector showing different components of muon chambers. Steel-flux return disks are shown as dark areas, DTs are labelled as MB, CSCs are labelled as ME, and RPCs are labelled as RB and RE. In this labelling *B* refers to barrel and *E* refers to endcap.

As the muon passes through the chambers, it ionizes gas in these chambers. Each of the DTs chambers have drift cells of size $42 \times 13 \text{ mm}^2$ in transverse direction. The CSCs are operated as standard multi-wire proportional counters. More detailed description of muon system and its performance can be found in Ref.[57, 54, 58].

The p_T resolution of muons is approximately 1% in barrel and 3% in endcap for $p_T < 100 \text{ GeV}$ [57]. The combined momentum measurement from tracker and muon system significantly improves the resolution and Fig.3.11 shows p_T resolution as a function of p_T of muon.

3.3 Energy response in long and short fibers of HF calorimeter

The HF is located at 11.3 m from the interaction point and provides a pseudo-rapidity coverage from $|\eta| > 3.0$ to $|\eta| < 5.2$. Since there is no coverage from the

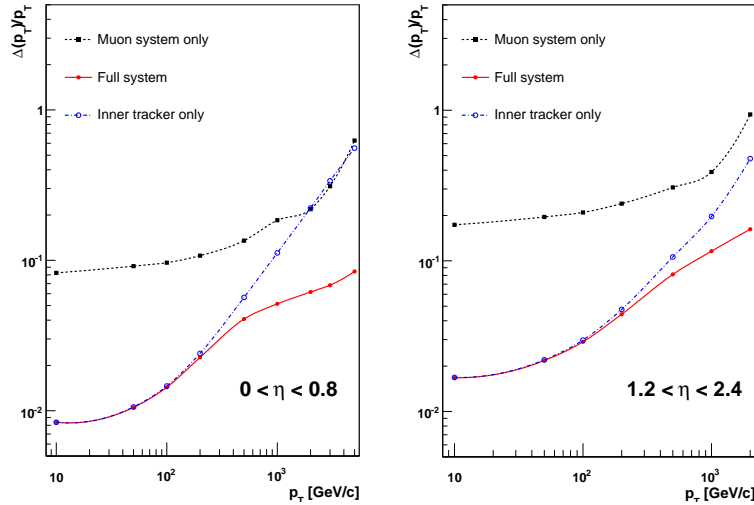


FIGURE 3.11: p_T resolution of muons as a function of p_T for $|\eta| < 0.8$ (left) and $1.2 < |\eta| < 2.4$ using tracker only, muon system only and combination of both [54].

tracker or ECAL in this region, the energy deposited in HF is used to reconstruct forward jets and also to calculate p_T^{miss} . Hence a stable performance of HF is important both for SM measurements and new physics searches.

The quartz fibers are inserted into the steel absorber plates. Half of the fibers run over the full depth of the HF (165 cm \approx 10 interaction lengths) while the remaining half of the fibers start at a depth of 22 cm from the front face of the detector. The former are called **long fibers** and latter are called **short fibers**. The energies deposited in long and short fibers are read out separately, and are called E_{Long} and E_{Short} respectively.

The signal in HF is due to the Cherenkov light produced by charged particles as they traverse through the quartz fibers. The Cherenkov light is emitted only when the particle's velocity is greater than the speed of light in that medium. This light is collected by the long and short optical fibers. The recordable signal in calorimeter is due to the electromagnetic and hadronic component of the particle showers. Since electrons or photons result in shorter showers, these result in signal mostly in long fibers. The hadronic showers, however, continue deeper and result in signal in both long and short fibers.

The ratio of energy measured in short and long fibers, $R_{S/L} = E_{Short}/E_{Long}$, depends on the energy of the incident particle which created the shower and hence on how deeply the shower has penetrated the calorimeter. However, the average $R_{S/L}$ over a period of time in a given η region is expected to depend on average energy incident on the calorimeter and accelerator run conditions (which determines the pileup, the number of pp interactions). In this section, we describe studies $R_{S/L}$ for data collected at $\sqrt{s} = 8$ TeV and $\sqrt{s} = 13$ TeV, and also the effect of pileup. Since the average $R_{S/L}$ for various channels of a given $i\eta$ ring is expected to be same, this quantity is proposed to be used to intercalibrate the short fibers across ϕ while the long fibers are calibrated using $Z \rightarrow e^+e^-$ events.

3.3.1 Data and simulation samples

These studies make use of data collected by CMS detector in the years 2012, 2015 and 2016. Each of these are divided into different parts and they are named by adding a

suffix to the year, for example 2012D is a subset of data collected in 2012. The events from these dataset are selected using triggers which are based on hadronic activity, calculated using sum p_T of all jets or using highest p_T jet in the event. The dataset which contains hadronic triggers is called as *JetHT* dataset. Only those data which are certified as good for physics analysis are used. Table 3.3 shows list of datatsets used for this study along with pp bunch spacing and integrated luminosity of the dataset. Monte-carlo (MC) simulated sample consists of QCD events generated at leading order (LO) taking $\sqrt{s} = 13$ TeV using MadGraph generator and hadronization is carried out using Pythia8.

TABLE 3.3: Collision data used for $R_{S/L}$ studies of HF. The 2012 data were taken at $\sqrt{s} = 8$ TeV and all other data were taken at $\sqrt{s} = 13$ TeV.

Data	Bunch spacing (ns)	$\mathcal{L} (\text{pb}^{-1})$
2012D	50	962
2015B		40.9
2015C	50	25.0
2015C		16.3
2015D	25	1.61×10^3
2016B		5.28×10^3
2016C		789
2016D		3.28×10^3
2016E	25	4.05×10^3
2016F		3.11×10^3
2016G		7.11×10^3
2016H		8.68×10^3

3.3.2 Energy in long and short fibers of HF

The HF starts at $|\eta|=2.853$ and extends up to $|\eta|=5.191$. On both the $\pm z$ sides, this η range is divided into 13 towers with tower index starting from $i\eta=29$ and ending at $i\eta=41$. Towers $|i\eta|=29$ to $|i\eta|=39$ have 36 divisions (10° each) in ϕ and towers $|i\eta|=40$ and 41 have 18 divisions (20° each). In total there are 864 channels. Depth segment with index 1 corresponds to long fibers and depth segment with index 2 refers to short fibers in each of these channels. If the energy in a particular channel is above the noise level, then that channel is considered to have a *rechit* (recorded hit).

All the plots and discussion till the end of section 3.3.3 correspond to 2015C-50ns data.

- Fig. 3.12 shows a typical distribution of number of rechits, with rechit energy > 10 GeV, in each of the channels in depth 1 (long fibers) and depth 2 (short fibers).
- Fig. 3.13 shows the total number of rechits distribution inclusive in $i\eta$ and $i\phi$ with rechit energy > 10 GeV.
- Fig. 3.14 shows the energy distribution in short fibers (E_{Short}) vs long fiber (E_{Long}) without any threshold on their recorded energies. This figure shows that there is correlation between E_{Long} and E_{Short} . So we use $R_{S/L}$ as a tool for studying the performance of HF.

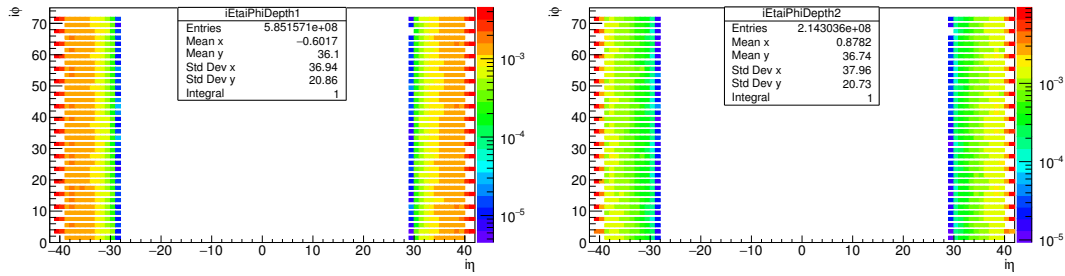


FIGURE 3.12: Channel occupancy for depth 1 (left), and depth 2 (right).

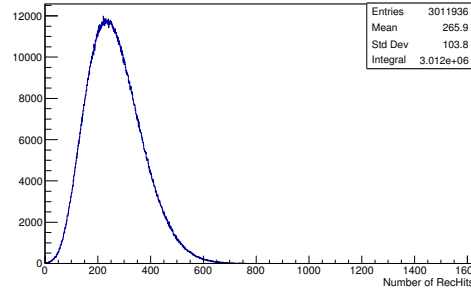


FIGURE 3.13: Total number of rechits (inclusive in $i\eta$ and $i\phi$)

There are two more important points to note from this plot: firstly, there are cases with a large E_{Long} while there is almost no energy deposited in corresponding short fiber i.e. $E_{\text{Short}} < 10 \text{ GeV}$. This can be due to EM showers. Secondly, there are cases when there is large energy deposited in short fibers while small energies in long fibers ($E_{\text{Long}} < 30 \text{ GeV}$). It is not expected to have large energy deposits in only one of the fibers if the shower originates from hadrons. One of the reasons for this could be that some of the high energy particles directly hit the glass window of PMT and resultant Cherenkov light produced in the glass gives rise to a large signal in only one of the channels. To reject such hits, thresholds are placed on reconstructed energies of rechits, $E_{\text{Short}} > 10 \text{ GeV}$ and $E_{\text{Long}} > 40 \text{ GeV}$. From this point onwards, one can assume that these threshold have been applied on E_{Short} and E_{Long} unless a different selection is explicitly mentioned.

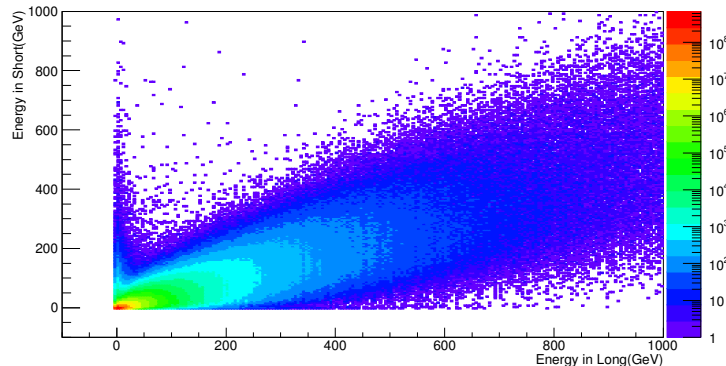


FIGURE 3.14: Distribution of E_{Short} vs E_{Long} for HF channels.

- With the energy thresholds mentioned above, $R_{S/L}$ is studied for each $i\eta$ tower. The Fig.3.15 shows distribution of the $R_{S/L}$ for the tower $i\eta = 32$ integrated over all $i\phi$ channels. Since the mean value of the distribution is sensitive to the tails, we try to fit it with an asymmetric Gaussian (eqn.3.7) and use the peak value obtained from the fit to indicate the average ratio for a given $i\eta$ ring.

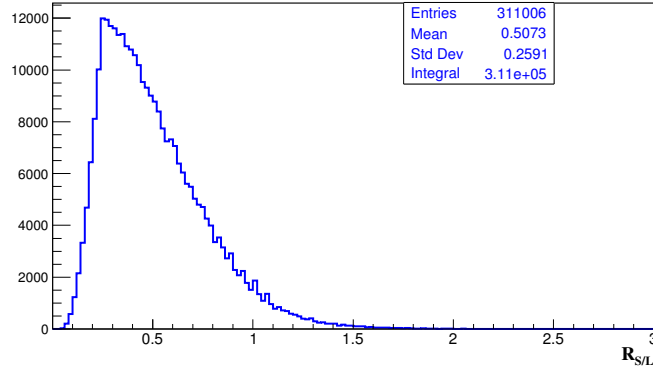


FIGURE 3.15: $R_{S/L}$ for $i\eta = 32$ tower with $i\phi$ inclusive for 2015D-50 ns.

$$f(x) = e^{-\frac{(x-\mu)^2}{2\sigma^2}} \left[1 + erf \left(\frac{x-\mu}{\sqrt{2}\sigma} \right) \right] \quad (3.7)$$

Fitting the $R_{S/L}$ with an asymmetric Gaussian works very well for smaller $i\eta$ channels (Fig. 3.16). For the channels in higher $i\eta$ regions, fitting does not work well and χ^2/dof is very large (Fig. 3.17). Changing the fit range did not improve the fits significantly. So using the peak obtained from the fits cannot be used for studying all the channels. We then use 90% truncated mean of the distribution - starting from the arithmetic peak, bin contents are added on both the sides until the total integral is 90% of the total area under the curve. From this point onward, mean refers to 90% truncated mean.

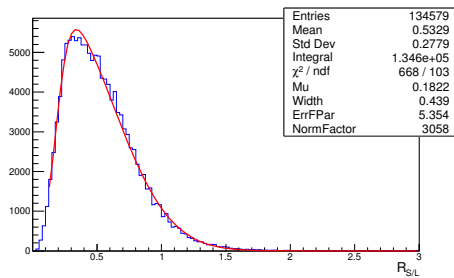


FIGURE 3.16: Asymmetric Gaussian fit for $i\eta = 30$

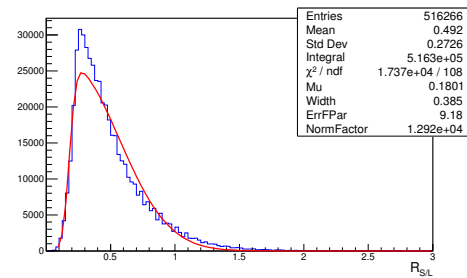


FIGURE 3.17: Asymmetric Gaussian fit for $i\eta = 39$

3.3.3 Effect of Pileup on $R_{S/L}$

The $R_{S/L}$ was studied under different pileup (PU) scenarios. If the number of good primary vertices is less than 9, it is considered as low pileup; between 11 and 16 as medium pileup and above 18 as high pileup.

Pileup is mainly dominated by low energy particles and these particles do not have enough energy to penetrate into the short fibers and hence they deposit

energy mainly in long fibers. Hence these particles give lower $R_{S/L}$ than the high energy particles. Pileup is added on top of a hard scattered events, and in hard scattered event $R_{S/L}$ is higher than PU events. Thus with increase of more and more pileup events, the $R_{S/L}$ is decreasing and that is the observation. With the high pileup, average energy deposits in long fibers is expected to be higher and as a result the $R_{S/L}$ is expected to be lower as compared to the low pileup scenario. Fig. 3.18 shows that higher pileup means lower ratio and lower pileup means higher ratio. The shaded region corresponds to all events wherein no restriction on pileup is applied.

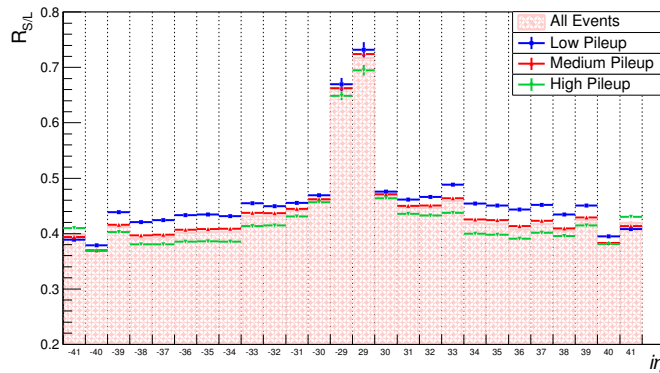


FIGURE 3.18: Effect of pileup on $R_{S/L}$ for different $i\eta$ rings (integrated over $i\phi$ channels).

3.3.4 Studying $R_{S/L}$ at $\sqrt{s} = 13$ TeV and 8 TeV data with 50 ns bunch spacing

- In 2015, LHC started 13 TeV collisions with 50 ns bunch spacing. We compared $R_{S/L}$ for 13 TeV data taken in 2015 and 8 TeV data taken in 2012.
- Used JetHT dataset for 13TeV data and 8 TeV with all the events (no trigger based selection of events) for this study.
- Average pile up was similar (Fig.3.19) in 8 and 13 TeV datasets.

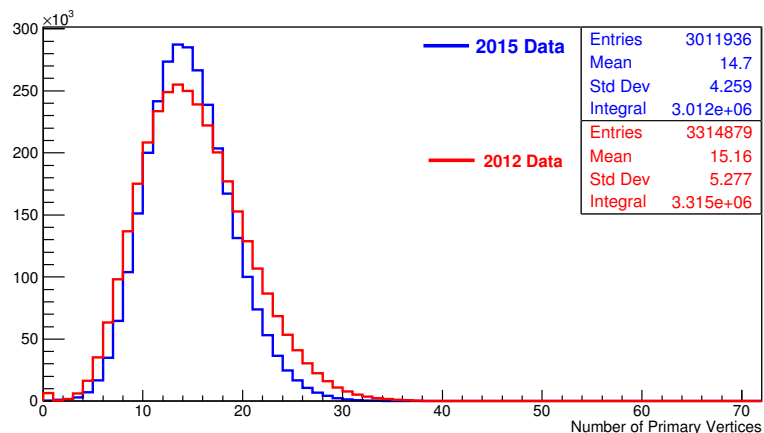


FIGURE 3.19: Pileup comparison for 2015 data and 2012 data

- Fig. 3.20 and 3.21 show the distributions of energies in long and short fibers, for 2012D and 2015C, with $E_{\text{Long}}, E_{\text{Short}} > 10 \text{ GeV}$.

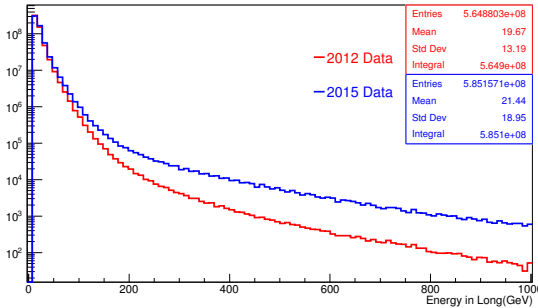


FIGURE 3.20: Energy in long fibers for 2012 and 2015 data

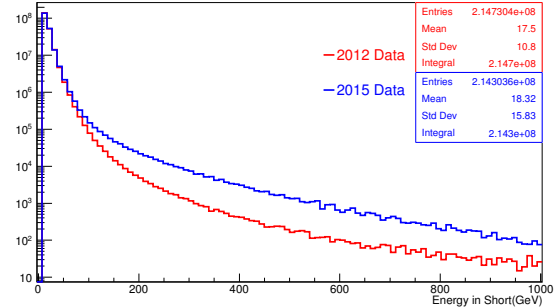


FIGURE 3.21: Energy in short fibers for 2012 and 2015 data

In 2015 p-p collisions, the \sqrt{s} was 13 TeV and in 2012 it was only 8 TeV. Because of the increased energy of the collisions, the outgoing particles will have higher energy and hence these particles can penetrate deeper into the calorimeter giving larger energy in short fibers. So the $R_{S/L}$ is expected to be higher in 13 TeV data as compared to 8 TeV data. $R_{S/L}$ was determined for different $i\eta$ towers, with $i\phi$ inclusive and it was compared for 2012D data, 2015B data and 2015C data (fig. 3.22). For most of the $i\eta$ towers, $R_{S/L}$ of 2015 data is higher than that of 2012. With the increase of \sqrt{s} , average energy of particles is also increasing, consequently the $R_{S/L}$ is increasing. The reason for differences in 2015 and 2012 data could be because of increased beam energy in p-p collisions and (or) the response of the fibers has changed. $R_{S/L}$ for $|i\eta| = 29$ is much higher as compared to other $|i\eta|$ towers. This is because, this tower is behind $|i\eta| = 28$ of HE. EM shower energy is already deposited in HE. HF receives only hadronic shower energy and this energy is deposited in both long and short. Hence $R_{S/L}$ is higher for these towers. $R_{S/L}$ as a function of $i\phi$ for each $i\eta$ was also studied.

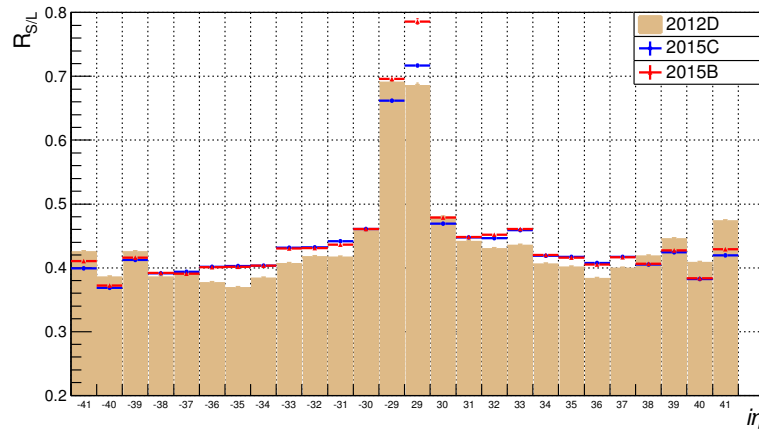
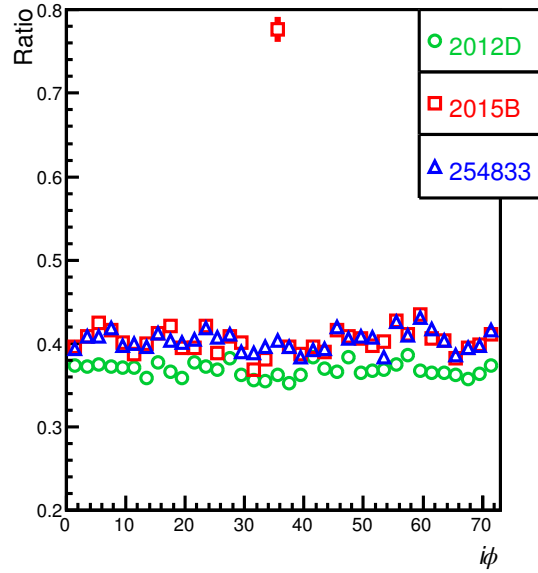


FIGURE 3.22: $R_{S/L}$ vs $i\eta$ for 3 different run conditions

Fig. 3.23 shows $R_{S/L}$ vs $i\phi$ for $i\eta = -35$. From this plot one can see whether a particular channel is problematic or not. In this figure, channel with $i\phi$ index 35 shows very high ratio in 2015B run. Also in most of the $i\phi$ s, $R_{S/L}$ for 2012 data is slightly lower than 2015 data $R_{S/L}$.

FIGURE 3.23: $R_{S/L}$ vs $i\phi$ plot for $i\eta = -35$

3.3.5 $R_{S/L}$ for 2015 Data and 2016 Data

Data taken in 2015 with 25ns bunch spacing was compared with the 2016 data (25ns bunch spacing) using JetHT dataset and requiring at least one jet with $p_T > 450$ GeV at trigger level. This comparison is useful to understand the problems or changes in 2016 in HF, if any, with respect to the previous data taking.

Pileup conditions for 2015 and 2016B were different (Fig.3.24). As discussed in sec.3.3.3, if the pileup is high, then the $R_{S/L}$ is expected to be smaller since more energy goes into the long fibers.

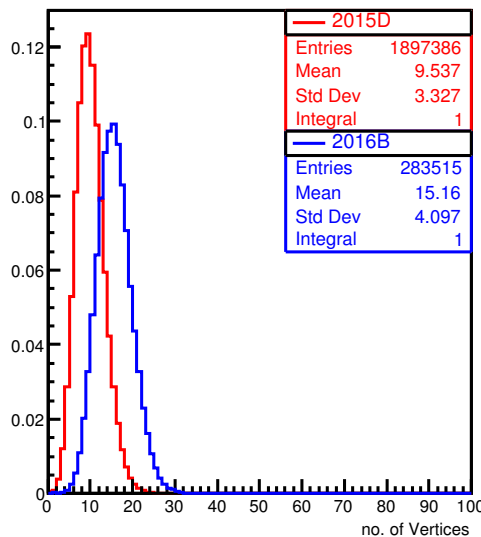


FIGURE 3.24: Number of primary vertices before re-weighting

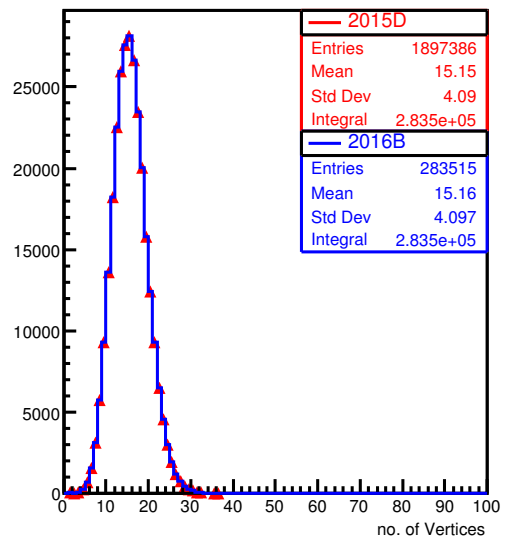


FIGURE 3.25: Number of primary vertices after re-weighting

In order to compare the data taken with these different conditions, events had to be reweighted according to the pileup. In this case, number of primary vertices (PV) distribution in 2015D was re-weighted to match PV distribution of 2016B. This

was done by simple division of 2016B histogram by 2015D histogram. The resulting histogram gives the pileup weights for 2015D as a function of different PVs. Fig. 3.25 shows the PV distribution after the reweighting. In Fig. (3.26-3.29) some of the HF parameters such as number of RecHits above 10 GeV, RecHit energy in long and short fibers for these runs are compared. These runs show very similar behavior with respect to these parameters.

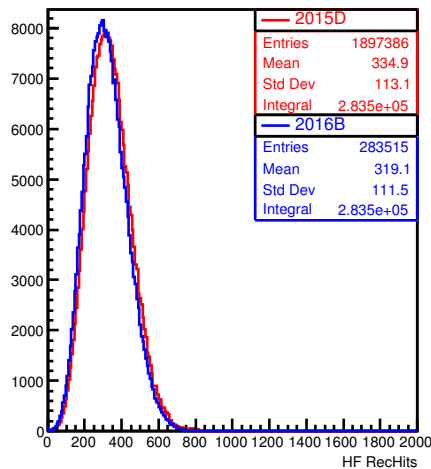


FIGURE 3.26: No. of HF RecHits above 10 GeV

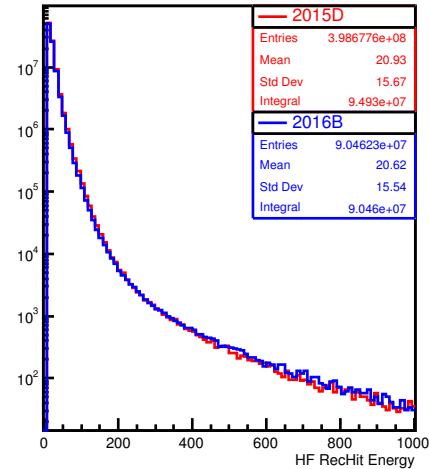


FIGURE 3.27: HF RecHit energy in long and short fibers

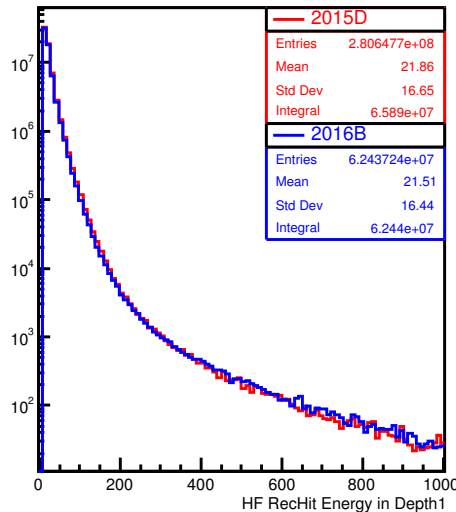


FIGURE 3.28: Energy in long

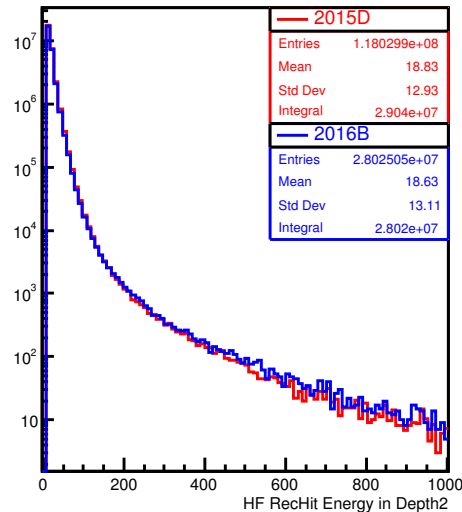
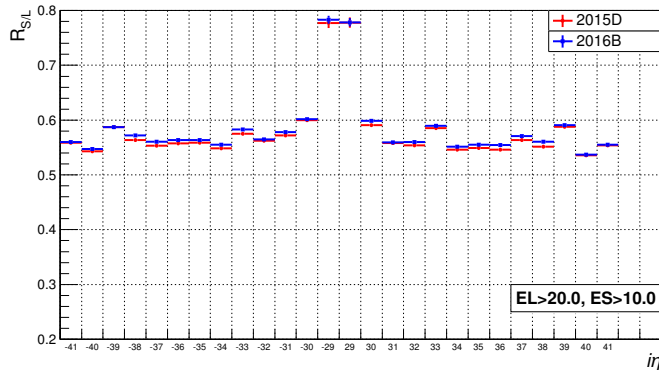


FIGURE 3.29: Energy in short

$R_{S/L}$ as a function of different $i\eta$ for 2015 data and 2016B data are compared in Fig.3.30. The plot shows that both the datasets have similar ratio and the agreement between these datasets is within 1-2%. It was found that the choice of a different hardonic trigger does not affect $R_{S/L}$ features seen in this plot.

FIGURE 3.30: $R_{S/L}$ for 2015 and 2016B data

3.3.6 Performance of $R_{S/L}$ in 2016 Data

In this section, different run eras of 2016 data (era B to H) are compared using JetHT dataset and events with at least one jet with $p_T > 450$ GeV at trigger level. Different run eras of 2016 had different pileup scenarios and 2016B has the smallest pileup among these. This can be clearly seen from the distributions of number of primary vertices (Fig. 3.31). If the pileup is higher, then the number of rechits are also higher. So larger pileup runs have higher mean number of rechits as shown in Fig. 3.32. All these distributions are normalized to unit area.

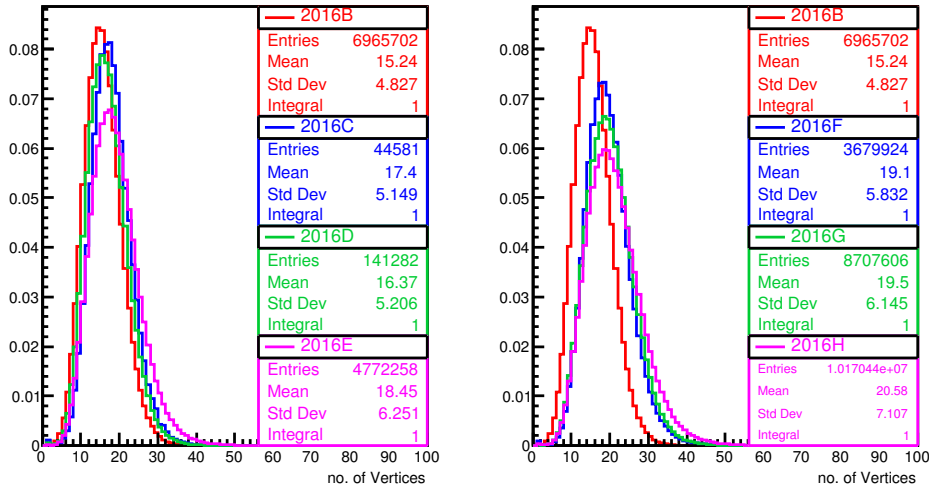


FIGURE 3.31: Number of primary vertices (left) for 2016B,C,D,E, and (right) for 2016B,F,G,H.

RecHit energy distributions for all run eras of 2016 show similar features (Fig. 3.33 - 3.34). Any differences seen in these distributions are because of the different pileup scenarios. In case of run 2016C and D, because of lower statistics (only a part of whole dataset was used), energy distributions show small variations. Run 2016B has lower pileup as compared to others and hence, energy distributions are slightly different from other runs. Runs 2016F to 2016H have very similar pileup and hence their energy distributions show better agreement (Fig. 3.34).

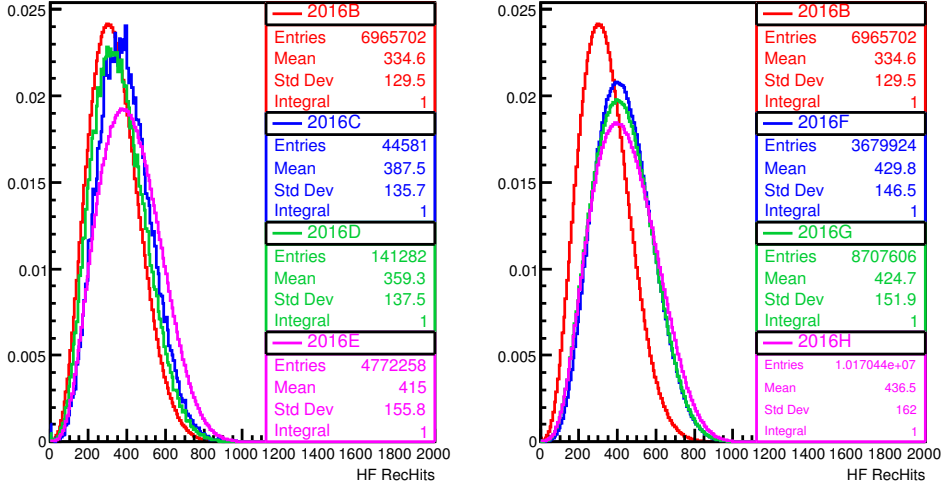


FIGURE 3.32: Number of RecHits (left) for 2016B,C,D,E, and (right) for 2016B,F,G,H.

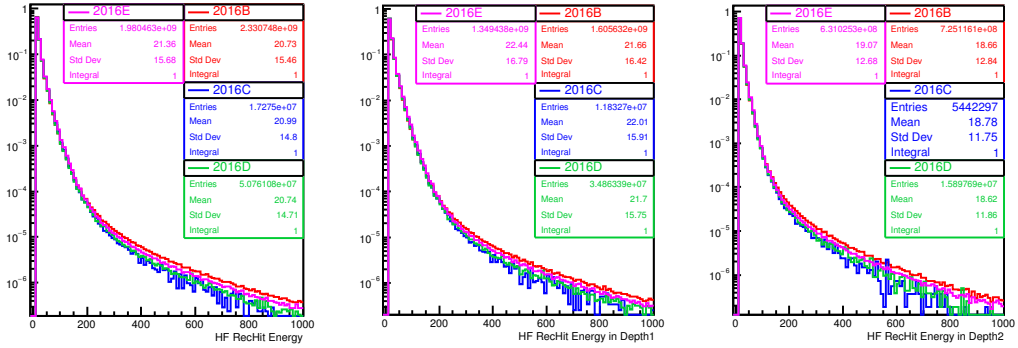


FIGURE 3.33: RecHitEnergy distributions for 2016B,C,D,E

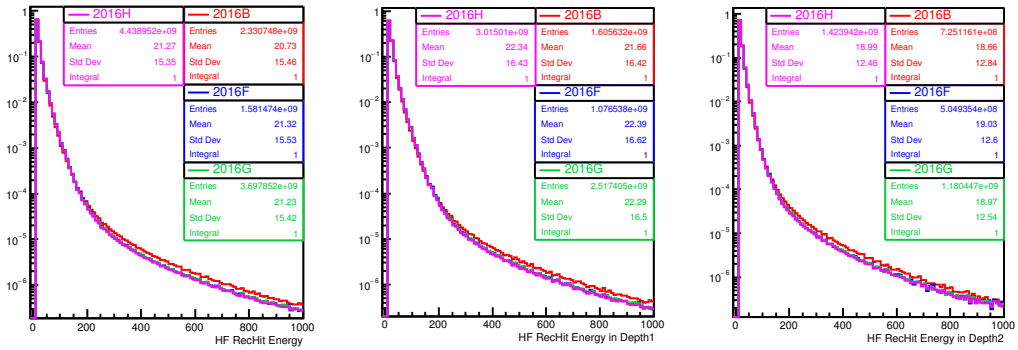


FIGURE 3.34: RecHitEnergy distributions for 2016B,F,G, H

Stability of R_{S/L} in 2016 Data

In order to check the stability of R_{S/L} across different $i\eta$ channels, mean R_{S/L} as a function of $i\eta$ is plotted for all the run eras of 2016 (Fig.3.35). Higher energy thresholds are also used to compare R_{S/L} of different run eras across various $i\eta$ channels.

Fig. 3.36 shows $R_{S/L}$ as a function of $i\eta$ with $E_{long} > 50$ GeV and $E_{short} > 10$ GeV. $R_{S/L}$ is found to be stable across all these run eras and also for different energy thresholds.

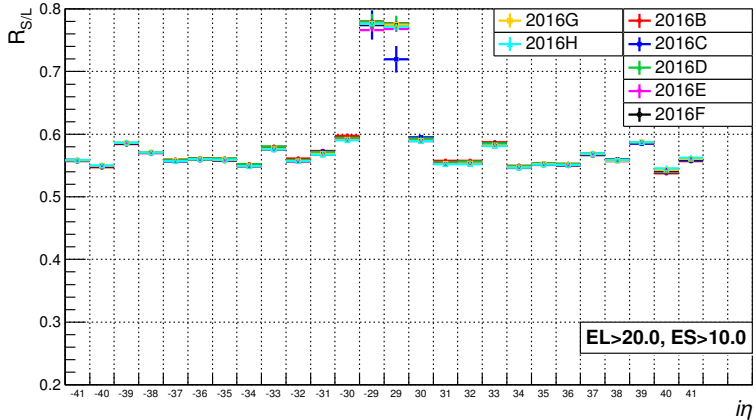


FIGURE 3.35: $R_{S/L}$ vs $i\eta$ for 2016 with lower E_{long} threshold

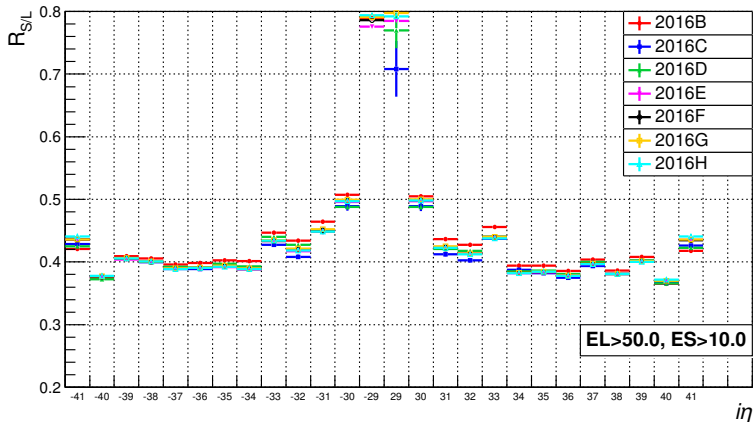


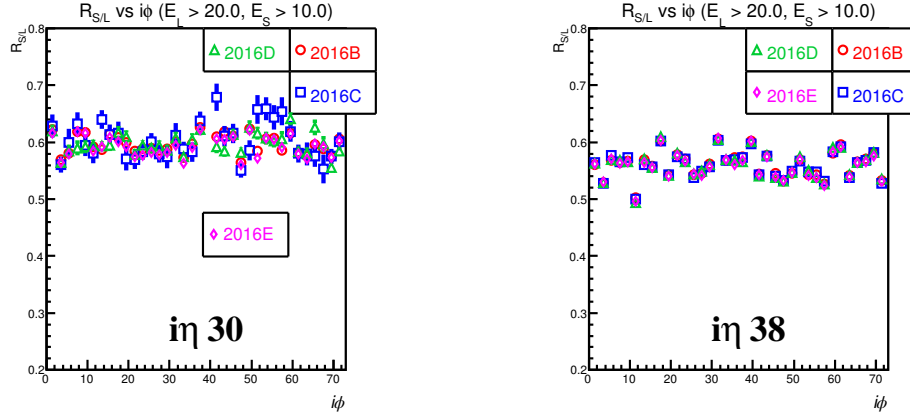
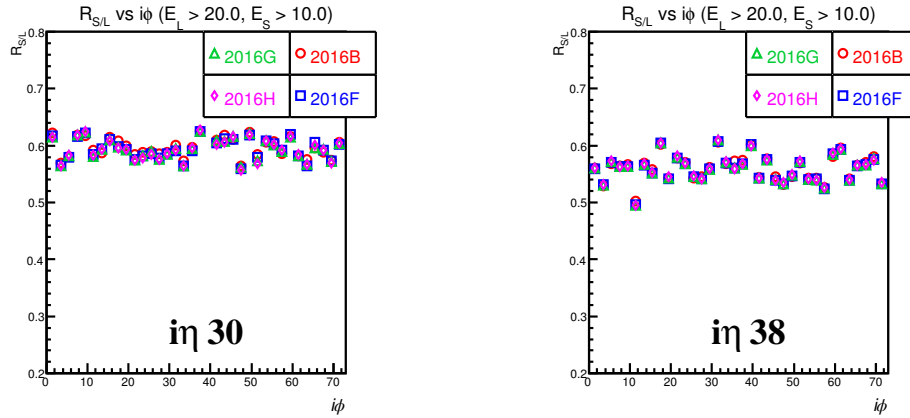
FIGURE 3.36: $R_{S/L}$ vs $i\eta$ for 2016 with higher E_{long} threshold

Corresponding to each $i\eta$ channels, there are 36 divisions in HF. ($|i\eta| = 40, 41$ have 18 divisions). $R_{S/L}$ as a function of $i\phi$ for a given $i\eta$ channel is also studied and a few such plots are shown in Fig.3.37 and Fig.3.38. Across all the channels for all these run eras, $R_{S/L}$ show consistent features. These plots clearly indicate that $R_{S/L}$ is stable across different run eras.

To make sure that there is no bias involved in using the JetHT dataset, comparison of $R_{S/L}$ for JetHT and a dataset consisting of muons (triggered by a muon with $p_T > 50$ GeV) is done. These two datasets showed very similar $R_{S/L}$.

3.3.7 Corrections for the $R_{S/L}$ Based on ϕ Symmetry

All the physics processes are symmetric in the azimuthal, ϕ direction (or the transverse x-y plane). So $R_{S/L}$ is also expected to be symmetric or flat across all ϕ channels for a given η or $i\eta$. Based on this symmetry, corrections are derived for the ratio such

FIGURE 3.37: $R_{S/L}$ vs $i\phi$ for 2016B,C,D,EFIGURE 3.38: $R_{S/L}$ vs $i\phi$ for 2016B,C,D,E

that $R_{S/L}$ is constant across all the ϕ channels for a given η . The corrections are derived as follows:

- Fit the $R_{S/L}$ vs $i\phi$ plot of 2016B with line of 0 slope, and intercept k .
- Correction for a channel is nothing but original $R_{S/L}$ times the intercept.

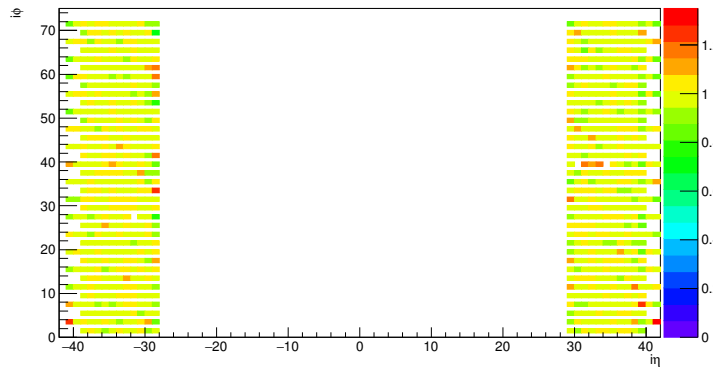
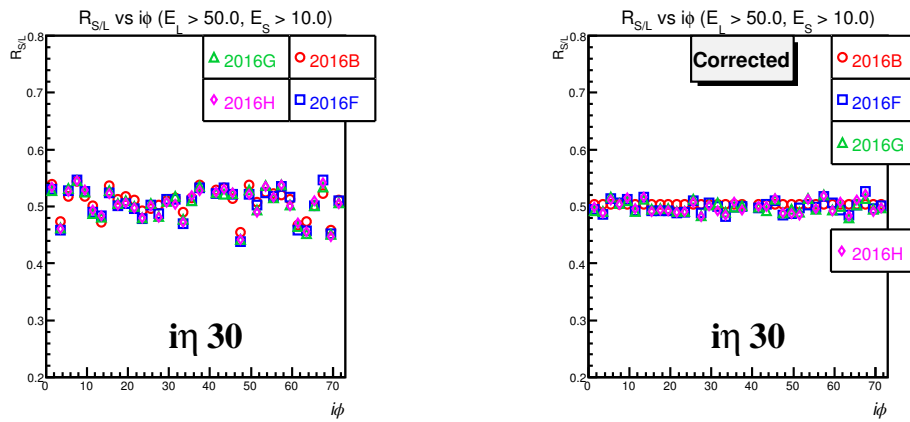
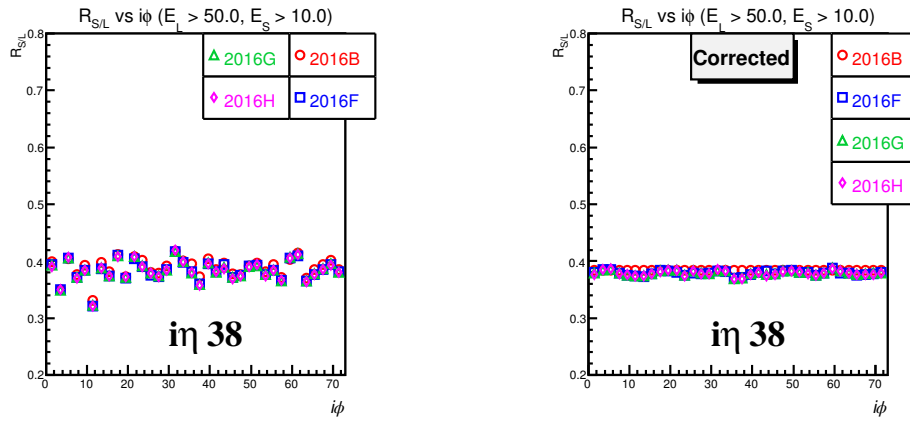
$$\text{Correction}(i\eta, i\phi) = k_{i\eta} \times R_{S/L} \quad (3.8)$$

$$\text{Corrected ratio}(i\eta, i\phi) = R_{S/L}^{\text{Corr}} = \text{Correction}(i\eta, i\phi) \times R_{S/L} \quad (3.9)$$

These corrections are obtained for all the channels of HF using 2016B dataset with $E_{long} > 50 \text{ GeV}$ and $E_{short} > 10 \text{ GeV}$. The corrections factors as a function of η and $i\phi$ are shown in Fig. 3.39. These corrections are applied to 2016B and the remaining 2016 run eras with the same threshold on E_{long} and E_{short} . (The errors on the correction factors are dependent on the error on the mean $R_{S/L}$ and the fit uncertainty. These errors are less than 1% for almost all the channels, except for $|i\eta|=29$)

Fig. 3.41 shows the comparison of ratio plots before correction (left) and after correction (right). Similar features are seen for other run eras i.e., 2016C,D and E.

Corrections derived so far had energy threshold on long as 50 GeV and almost no energy threshold on short energy (10 GeV). Using 50 GeV threshold on long makes the corrections less prone to pileup dependencies. To check the dependency of the corrections on energy thresholds used, these corrections are also used for the ratio plots with different thresholds on long for the same dataset 2016B. Fig. 3.42 and 3.43

FIGURE 3.39: Correction factors as a function of $i\eta, i\phi$ FIGURE 3.40: $R_{S/L}$ vs $i\phi$ for $i\eta = 30$ for (left) current detector, and (right) after corrections for 2016B,F,G,HFIGURE 3.41: $R_{S/L}$ vs $i\phi$ for $i\eta = 38$ for (left) current detector, and (right) after corrections for 2016B,F,G,H

show the ratio plots before and after corrections for the energy thresholds $E_{long} > 30 \text{ GeV}$ and $E_{long} > 100 \text{ GeV}$. The corrections are derived from 2016B with $E_{long} > 50 \text{ GeV}$. The corrected points are multiplied by a factor of 1.3 so that they can be visualized in the same plots.

It is clear from the Fig.3.41-Fig.3.43 that using the corrections on the ratio, improves the symmetry in ϕ .

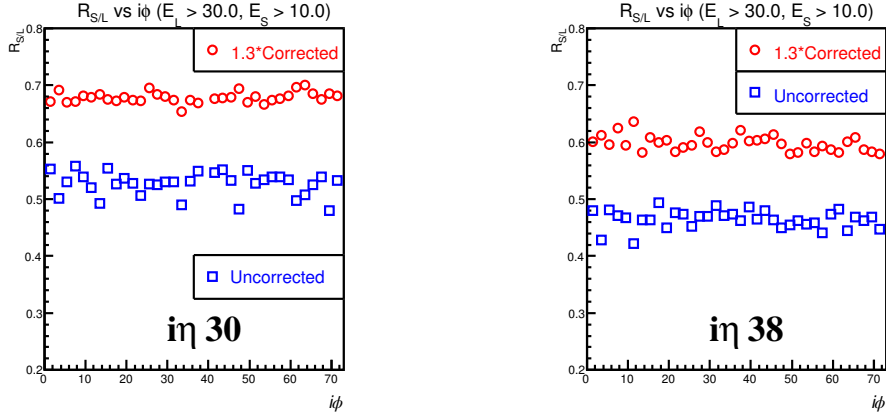


FIGURE 3.42: $R_{S/L}$ vs $i\phi$ before and after corrections for 2016B with $E_{long} > 30, E_{short} > 10$

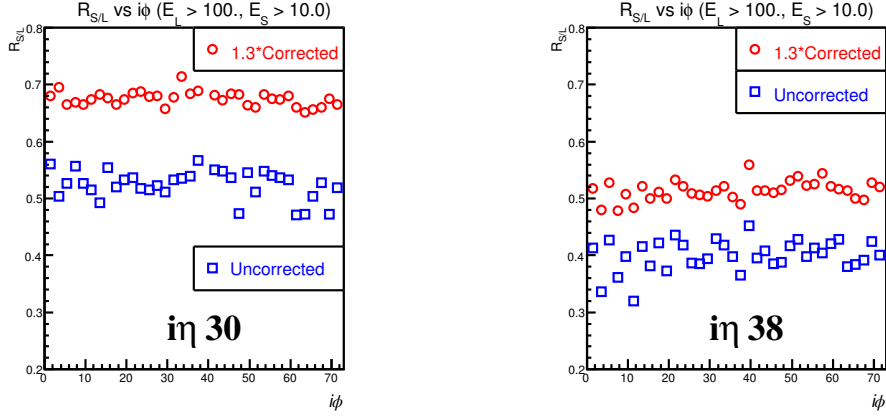


FIGURE 3.43: $R_{S/L}$ vs $i\phi$ before and after corrections for 2016B with $E_{long} > 100, E_{short} > 10$

The long fibers are calibrated using $Z \rightarrow e^+ + e^-$ events. The plots shown indicate that $R_{S/L}$ is stable across different runs and it improves the ϕ symmetry. So $R_{S/L}$ can be used as a tool to inter-calibrate the short fibers.

3.3.8 Performance of $R_{S/L}$ in data & MC

In this section comparison of QCD MC sample with data is done. JetHT dataset of 2016E is used for the studies. Trigger used to select events in the data is found to be $\approx 100\%$ efficient for jet $p^T > 500$ GeV. There is no trigger requirement for the MC samples. Apart from this selection, the event must contain (in both data and MC) at least one jet with $p^T > 600$ GeV and within $|\eta| < 2.4$. Nominal HF rechit filters are also used.

Data and MC have different number of observed interactions or different pileup (Fig.3.44). So MC is re-weighted such that the observed number of interactions in data and MC match. Solid blue line corresponds to the observed interactions in MC before PU re-weighting and dotted blue refers to observed interactions in MC after PU re-weighting.

MC is scaled to integrated luminosity of the data ($= 4.05 \text{ fb}^{-1}$). After this scaling of MC, MC had more events (integral) than data (about 20% higher). So MC is scaled down so that the integrals in data and MC match.

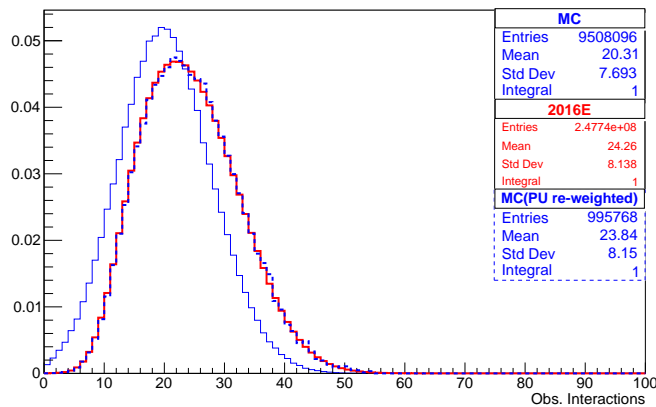


FIGURE 3.44: Observed number of interactions in data and MC (Solid blue line-
MC before PU re-weighting, dotted blue-after PU re-weighting).

Fig. 3.45 shows the number of reconstructed primary vertices and Fig. 3.46 shows the number of HF rechits above 10 GeV (after all MC re-weightings mentioned above).

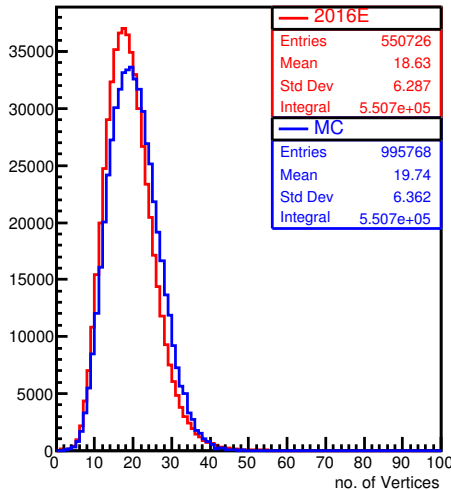


FIGURE 3.45: Number of reconstructed primary vertices in data and MC

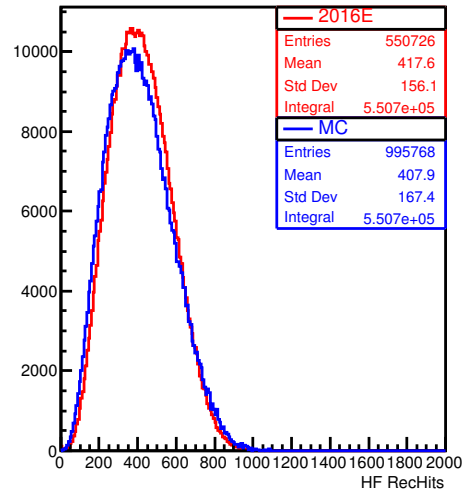


FIGURE 3.46: Number of HF rechits above 10 GeV

Fig. 3.47 (left) shows the energy distribution in HF. The energy distributions in data and MC show different behavior. Fig. 3.47 (middle) shows energy in long and fig.3.47 (right) shows the energy in short. The energy distributions in long fibers show more discrepancies as compared to the ones in short. In data, energy falls more rapidly than the ones shown by MC.

$R_{S/L}$ vs $i\eta$

Average $R_{S/L}$ is determined for data and MC with different energy thresholds on E_{long} and E_{short} and they are plotted as a function of $i\eta$ (Fig. 3.48 - Fig. 3.50). If the energy threshold is low (Fig. 3.48), data and MC show large discrepancies. If

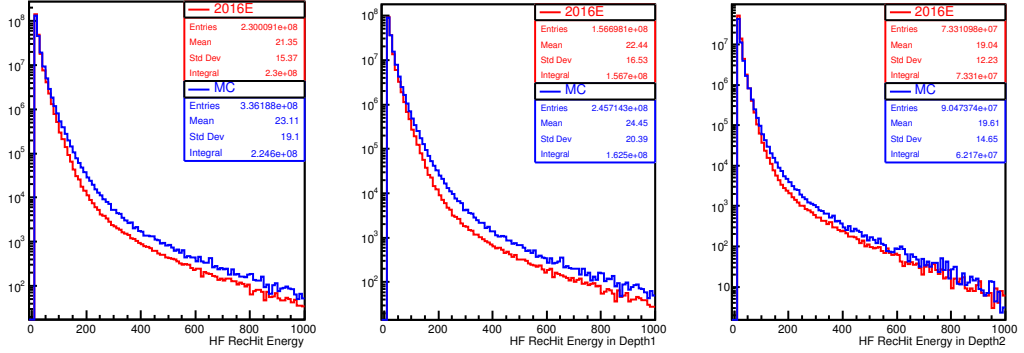


FIGURE 3.47: Distribution of energies in (left) all HF rechits, (middle) long fibers or depth 1, and (right) in short fibers or depth 2.

higher E_{long} threshold is used, then the agreement is better (Fig. 3.49). However increasing the E_{long} threshold to very high values also shows discrepancies (Fig. 3.50). Increasing short energy threshold along with long threshold gives better agreement (Fig. 3.51) between data and MC. The differences are present at long and short energy itself (Fig. 3.47). If data and MC agree for certain thresholds, then it because the differences in long and short cancel to some extent.

As the energy thresholds are varied, shape of the distributions in these plots also change. One reason is that, shape of $R_{S/L}$ distribution is different for different $i\eta$ (fig.3.16 and fig.3.17). The other reason is because of the correlation between long and short energies. Any threshold on long or short affects the energy in the other. In fig.3.51, the threshold on long and short are same (50GeV). This energy threshold will not select many of EM showers since E_{short} is very high. In other words, different thresholds select different EM and hadronic components.

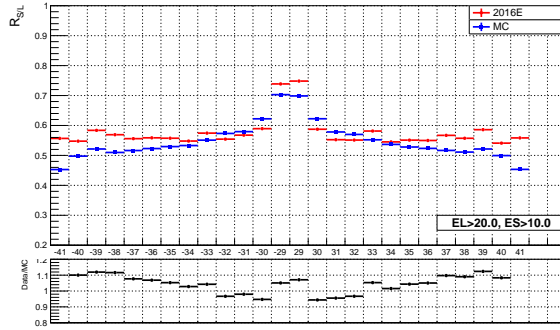
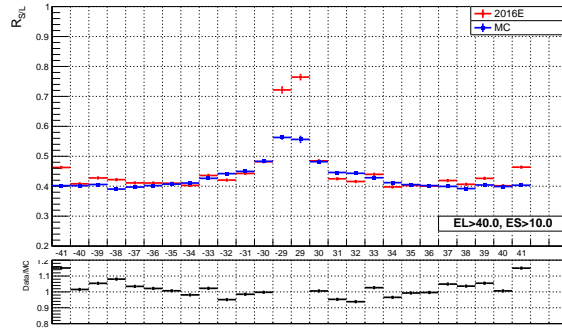
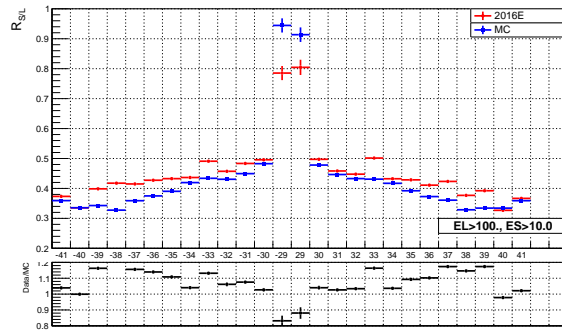
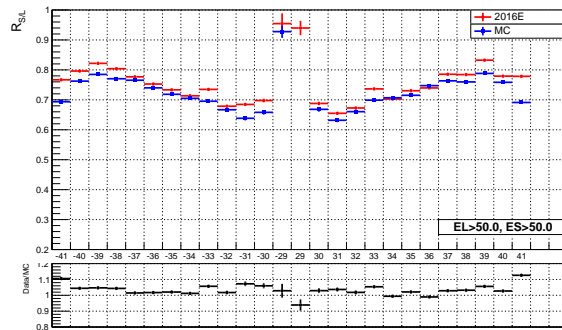


FIGURE 3.48: $R_{S/L}$ vs $|i\eta|$ with $E_{long} > 20, E_{short} > 10$ GeV

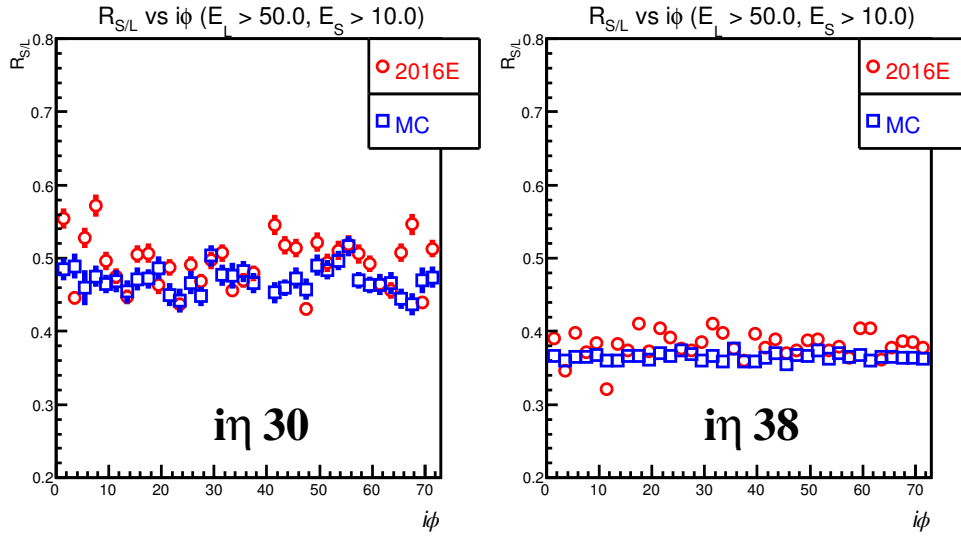
$R_{S/L}$ vs $i\phi$

Since $R_{S/L}$ vs $i\eta$ plots for data and MC show differences, it is obvious that $R_{S/L}$ does not agree for different $i\phi$ s as well (Fig. 3.52). However, it can be seen that $R_{S/L}$ is flat (constant across all $i\phi$) for a given $i\eta$.

FIGURE 3.49: $R_{S/L}$ vs $|i\eta|$ with $E_{long} > 40, E_{short} > 10$ GeVFIGURE 3.50: $R_{S/L}$ vs $i\eta$ with $E_{long} > 100, E_{short} > 10$ FIGURE 3.51: $R_{S/L}$ vs $i\eta$ with $E_{long} > 50, E_{short} > 50$

3.3.9 Summary of HF studies using $R_{S/L}$

Study of performance of hadron forward (HF) calorimeter was done using ratio of energy deposited in short to long fibers ($R_{S/L}$) of HF. Data collected by CMS in 2012 with $\sqrt{s} = 13$ TeV was compared with 2015 data using $R_{S/L}$. For most of the $i\eta$ towers, 2012 showed lower $R_{S/L}$ than 2015, which might be because of increased \sqrt{s} or radiation damage. Affect of pileup on $R_{S/L}$ was studied and with increased pileup, $R_{S/L}$ was found to decrease. Comparison of 25ns bunch spacing 2015 data and 2016 data was done and $R_{S/L}$ showed similar features. Different run eras of 2016 also showed similar $R_{S/L}$, which indicates the stability of $R_{S/L}$ across these run eras. For a given $i\eta$, different $i\phi$ s showed small variations in $R_{S/L}$. Corrections were obtained using 2016B to make the $R_{S/L}$ constant (flat) across these ϕ channels and these corrections improved flatness of $R_{S/L}$. Assuming that long fibers are well calibrated within a given $i\eta$, these corrections can be used intercalibrate short fibers.

FIGURE 3.52: $R_{S/L}$ vs $i\phi$ for data and MC

Comparison of data and MC was also done and these shows differences in terms of energy distribution in long and short fibers. $R_{S/L}$ also shows differences for many of the channels. The agreement in terms of $R_{S/L}$ is better for higher enrgy threholds.

3.4 Trigger system

In CMS, two levels of triggering system is used to reduce the rate of data flow from various detectors. The first level trigger (L1) is hardware based and the second level is software based (high level or HLT). The trigger system is inevitable since there is several orders of magnitude difference between inelastic pp cross section and other SM and SUSY processes, and it is not possible to collect, store and process all of the pp collision data because of limiting factors in terms of the rate of writing into a disk and storage capacity. Figure 3.53 shows the cross section (on left y-axis) for various SM processes, and SUSY processes which are theoretically calculated [59]. Only those events which are of potential interest to LHC physics are saved.

The pp collision frequency is 40 MHz. The L1 trigger (L1T) system uses custom hardware made using field programmable gate arrays (FPGAs) and GaAs application-specific integrated circuits (ASICs). The output rate is adjusted depending on the LHC luminosity and it is maintained below 100 kHz which is the upper limit imposed by readout electronics. It takes about $4\mu\text{s}$ for L1T to make a decision and the detector data is stored in front-end pipelines. The L1T selects events containing various candidate objects or a combination of the objects - ionization deposits consistent with muon, or ECAL energy clusters for electrons/photons, or energy deposits in calorimeters expected from τ , jet, or missing transverse momentum obtained by vectorially summing the objects and using transverse component. A schematic diagram of L1T is shown in Fig.3.54 [60]. The data from calorimeters is processed regionally and globally forming regional and global calorimeter trigger (RCT and GCT). Global muon trigger (GMT) is formed by taking hits from various muon systems by making use of pattern comparator or segment and track finder. The global trigger (GT) makes the final decision about the event by combining GCT and GMT. This decision is sent to CMS subdetectors via trigger timing and control (TTC). The DAQ (data acquisition system) reads data from subsystems for offline processing.

HLT performs reconstruction and identification of objects similar to offline, but faster and less precise. It makes use of several computers which run various algorithms in a predefined order and increasing complexity and takes about 160 ms to make a decision. Selections based on the information from calorimeters and muon chambers is carried out first and then the CPU intensive tracking reconstruction. The output data flow from HLT is about 400 Hz and it is used for offline storage.

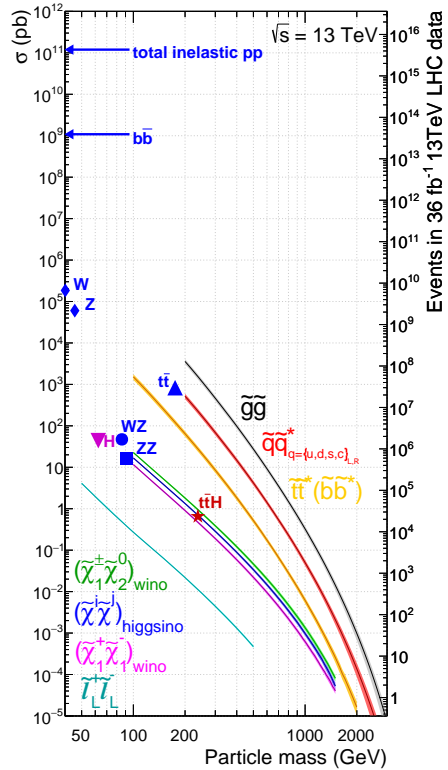


FIGURE 3.53: Comparison of cross section for various SM processes and SUSY processes.

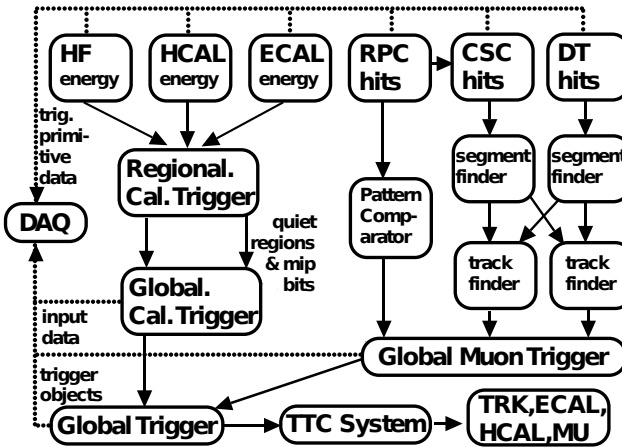


FIGURE 3.54: A schematic diagram of L1T [60].

3.5 Object reconstruction

The identification and reconstruction of various physics objects is done using the information from subdetectors using particle-flow (PF) algorithm [61]. Fig.3.55 shows the interaction of different particles in a transverse slice of CMS detector. The charged

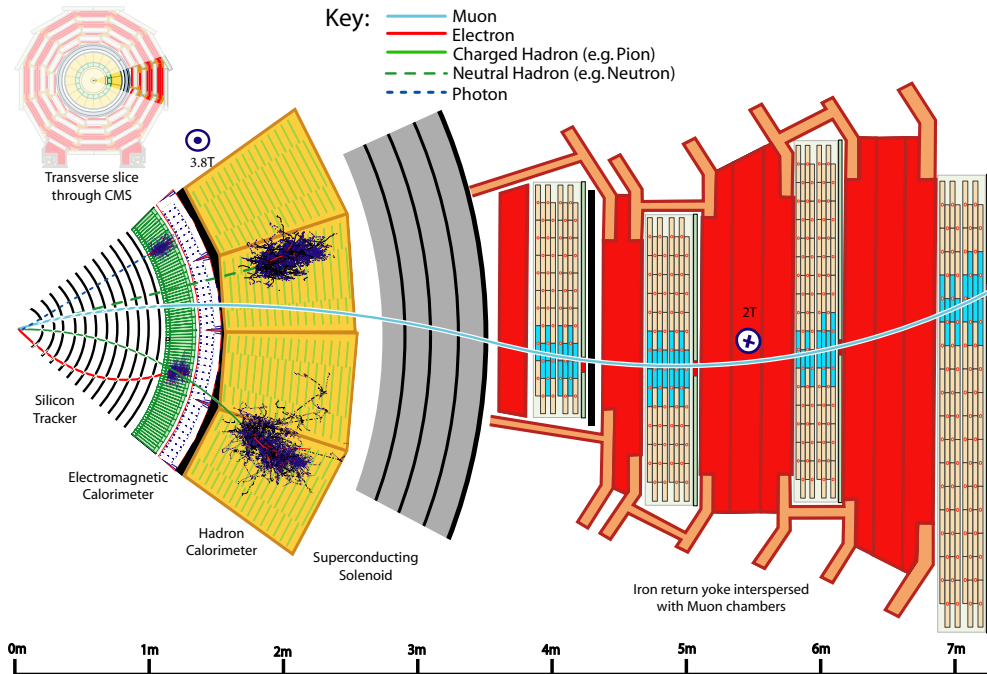


FIGURE 3.55: A sketch showing interaction of particles in a slice of CMS detector

particles leave signatures in various layers of the inner tracker because of 3.8 T magnetic field provided by the solenoid. Muon, being charged and minimum ionizing particle, bends in magnetic field and gives hits in the tracker and outer muon chambers. Electrons give hits in tracker and deposit almost all their energy in the ECAL.

Photons can be identified if there is energy deposit in ECAL, but no track associated with this energy deposit. Hadrons deposit most of the energy in HCAL and distinction of neutral and charged hadron is done by the presence of track.

3.5.1 Tracking

Track reconstruction takes place using a combinatorial track finder (CTF) algorithm based on Kalman filtering (KF). Full tracking is an iterative process starting with the easiest tracks and then proceeding to find more difficult tracks. After each iteration, hits compatible with the tracks are removed and this reduces the number of hits to use for the next iteration. There are 4 steps in an iteration.

- **Seed generation:** Finding track candidates using 2-3 hits compatible with charged particle trajectory.
- **Track finding:** Extrapolate the trajectory of the seeds to find compatible hits in the other layers using KF technique.
- **Track fitting:** Perform fitting to smooth the trajectory and find track parameters - origin, p_T and direction.
- **Track selection:** Apply selection criteria on the tracks based on number of layers with a hit, number of layers with missing hits, number of 3D hits, goodness of fit (χ^2) and impact parameters of the track.

For the next iteration, hits used in this iteration are removed and some of the selection criteria are changed in order to reconstruct more difficult tracks which originate because of missing hits in the pixel detector, particle interactions and decays, high p_T jets with collimated particles etc.

The basic idea in tracking of electrons is extrapolation of tracks to ECAL energy clusters. The iterative tracking mentioned above is efficient for non-radiating electrons. Because of non-negligible tracker material (Fig.3.7), electrons radiate photons. Depending on the energy of the radiated photon, values of χ^2 and number of hits may vary. In these cases, Gaussian-sum filter (GSF) technique [62] is used instead of KF. GSF fitting allows for sudden change in momentum of the tracks as the electron passes through various layers of tracker. Finally, a requirement is applied on the score of a boosted decision tree (BDT) classifier which uses various parameters of the KF and GSF tracks.

3.5.2 Interaction vertices

When the pp bunches collide at the LHC, multiple pp interactions can take place. The goal of vertex reconstruction is to locate the position of such interactions along with the uncertainties associated with it. This process involves 3 steps [63]:

1. selection of tracks: tracks passing quality criteria based on transverse impact parameter relative to the beam spot, number of hits and normalized χ^2 .
2. clustering of tracks which seem to originate from same vertex: the z-coordinates of the selected tracks measured from center of the beam spot to the point of closest approach are used for clustering. The algorithm should be able to resolve very close vertices, but not split a genuine single vertex into many. Deterministic annealing (DA) algorithm [64] [63] is used for this purpose.

3. fitting the position of each vertex using its associated tracks with the help of adaptive vertex filter [65].

After all interaction vertices are reconstructed, the primary pp interaction vertex is selected as the vertex with the largest p_T^2 sum of all physics objects. The physics objects used in this calculation are produced by a jet-finding algorithm [66, 67] applied to all charged-particle tracks associated to the vertex, plus the corresponding p_T^{miss} computed from those jets.

3.5.3 Muons

Since the calorimeters absorb energy of EM objects and hadrons, hits in muon spectrometer can be used to reconstruct muons. These muons which are reconstructed using muon systems only are called *standalone muons*.

If the standalone muon track is compatible with the track from the inner tracker, a new *global muon* track is fitted to the hits from both the systems.

If at least one muon segment matches with the extrapolated track from inner tracker, corresponding muon is called *tracker muon*.

The performance of global muon is better than standalone or tracker muon since it uses information from inner tracker and muon system.

The momentum of muon is determined using *Tune-P* algorithm [68]. The reconstructed muons are fed into PF algorithm which combines information from other subdetectors of CMS and applies various quality criteria. The identification of muons uses criteria on track fit χ^2 , number of hits in tracker or muon chambers or both, compatibility of tracker tracks and hits/tracks in muon chambers and also the compatibility with primary vertex. Detailed muon reconstruction procedure and its performance in 2015 and 2016 data is described in ref. [57].

3.5.4 Electrons and photons

Electrons and photons interact in similar way in ECAL. The material in the tracker lead to conversion of photons in to e^+e^- pairs and electrons can emit bremsstrahlung photons, photons again convert etc.

When an electron radiates photon, energy is spread in ϕ direction because of the magnetic field and there is negligible spread in η direction. The amount of energy radiated depends on η and it varies from 33% to 86% [69].

An electron candidate is seeded from a GSF track, provided the corresponding ECAL cluster is not linked to 3 or more additional tracks. A photon candidate is seeded from a ECAL energy cluster with transverse energy, $E_T > 10$ GeV with no link to GSF track.

Two algorithms, *hybdrid* for the barrel (EB) and *multi 5x5* for endcap (EE) [69] are used to collect the energy of the radiated photons in case of electron reconstruction or converted photons in case of photon reconstruction. Clustering is performed on intercalibrated, reconstructed signal amplitudes after taking care of several detector effects. Clustering starts with a seed crystal which is the highest E_T crystal in its neighborhood. In EB, clusters are centered on the seed crystal and have a fixed width of 5 crystals in η . In the ϕ direction, adjacent strips of 5 crystals are added. Further η aligned crystals may be seeded and added if they lie within ϕ window of ± 17 crystals. At each step of clustering, predefined thresholds on energy are applied. Clustering in EE is carried out using fixed 5x5 crystal matrices. After identifying the seed crystal, more matrices are added if their centroid lies in η of 0.07 and ϕ distance of about 0.3 radians. These matrices are partially allowed to overlap. If the photons

do not convert, then superclusters resulting from these algorithms are simply 5x5 matrices. More details about electron and photon reconstruction and performance can be found in ref. [69, 70].

Photon Identification

The collection of photons derived from PF algorithm have very loose criteria on their properties. For the purpose of analyses, more tighter requirements are placed on photons. The main idea is to get highest efficiency for prompt isolated photons and reject non-prompt photons which are coming from π^0 decays or part of hadronization process. Several properties of PF photons are studied to distinguish prompt and non-prompt photons. Prompt photons generally have smaller energy spread in ECAL and very less energy deposit in HCAL. Non-prompt photons are associated with charged or neutral hadrons nearby and they deposit energy in HCAL and sometimes a part of their energy in ECAL leading to larger ECAL clusters. Table 3.4 shows a list of variables and their values used for selecting photons in this SUSY search. Description of variables used for photon identification:

TABLE 3.4: A list of variables used for identification (ID) of photons in barrel and endcap. Prompt photon properties should not exceed any of the values listed in this table. Bottom 2 rows show the efficiency for signal (prompt photons) and background (non-prompt photons).

Property	Max value in EB	Max value in EE
H/E	0.05	0.05
$\sigma_{i\eta i\eta}$	0.0102	0.0274
PF h^\pm iso	3.32	1.97
PF h^0 iso	$1.92 + 0.014p_T + 0.000019p_T^2$	$11.86 + 0.0139p_T + 0.000025p_T^2$
PF γ iso	$0.81 + 0.0053p_T$	$0.83 + 0.0034p_T$
Efficiency	EB (%)	EE (%)
Signal	90	90
Background	16	18

- H/E: Ratio of energy in HCAL tower behind ECAL supercluster to energy of supercluster.
- $\sigma_{i\eta i\eta}$: This is a shower shape variable which is the second moment of the energy distribution along the η coordinate.

$$\sigma_{i\eta i\eta}^2 = \frac{\sum_i^{5\times 5} w_i (i\eta_i - i\eta_{seed})^2}{\sum_i^{5\times 5} w_i}, \quad w_i = \max(0, 4.7 + \ln \frac{E_i}{E_{5\times 5}}) \quad (3.10)$$

The summation runs over 5x5 crystal matrix around most energetic crystal in the supercluster. Prompt photons deposit large fraction of the energy in the seed crystal with a small spread around the seed crystal. Non-prompt photons and hadrons which deposit energy in ECAL, tend to have energy spread over several crystals near the seed crystal. In this way shower shape variable helps in identification of prompt photons and reject background more efficiently.

- PF h^\pm iso: PF charged hadron isolation variable which is defined as sum of p_T of all PF charged hadrons which are associated to the primary vertex, not in the footprint of the candidate photon, and within a cone of $\Delta R = 0.3$.
- PF h^0 iso: Pileup corrected PF neutral hadron isolation defined as sum of E_T of all PF neutral hadrons which are not in the footprint of the candidate photon and are within a cone of $\Delta R = 0.3$.
- PF γ iso: Pileup corrected PF photon or γ isolation is defined as sum of E_T of all PF photons which are not in the foot-print of the candidate photon and are within a cone of $\Delta R = 0.3$.

The PF h^0 and γ isolations are corrected for pileup contributions using $\text{Iso}_{\text{corr}} = \text{Iso}_{\text{original}} - \rho \text{EA}$, where ρ is the energy density of the event calculated using FastJet package [67] which is a measure of pileup activity in the event per unit area and EA is the effective area.

Inefficiency in electron track reconstruction and quality criteria on tracks may result in electron being mis-identified as photon; but there might have been hit(s) in the pixel detector. If the ECAL energy cluster is associated with hit(s) in the pixel detector then the corresponding electron or photon is said to have pixel seed. To reject mis-identification of electrons into photons, an additional criteria called *pixel seed veto* is also used.

This identification criteria shown in table 3.4 with pixel seed veto is called *loose ID + pixel seed veto*. The efficiency for this selection is shown in figure 3.56. This efficiency is determined using simulation with data to simulation corrections applied.

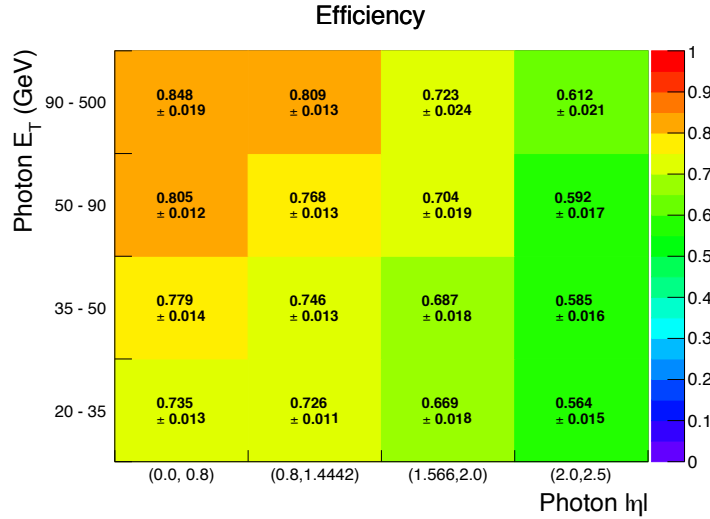


FIGURE 3.56: Efficiency for loose ID + pixel seed veto photons determined from simulation. The uncertainty includes statistical and systematic.

Electron Identification

Various quality criteria are applied to PF electrons in a similar way as photons. Since electron also has a track, electron ID makes use of track based variables apart from photon ID variables. In this analysis, we use *mini-isolation*, $I_{\text{mini}} < 0.1$ instead of

isolation calculated using fixed cone size of $\Delta R = 0.3$.

$$I_{mini} = \frac{\sum_R p_T(h^\pm) + \max(0, \sum_R p_T(h^0) + p_T(\gamma) - \rho E A (\frac{R}{0.3})^2)}{p_T(e)} \quad (3.11)$$

The variables used in this equation are same as the ones used for photon and its calculation is similar to the way fixed cone isolation is calculated, except that the isolation cone size is dependent on p_T of the electron [71]. The size of the cone varies as:

$$R = \begin{cases} 0.2 & \text{if } p_T < 50 \text{ GeV} \\ 10 \text{ GeV}/p_T & \text{if } 50 < p_T < 200 \text{ GeV} \\ 0.05 & \text{if } p_T > 200 \text{ GeV} \end{cases}$$

In case of boosted $t\bar{t}$ events involving $W \rightarrow ev$, b-jet from top decay may be very close to the electron. The fixed cone isolation becomes inefficient in identifying these kind of electrons. Since the cone size is smaller for large p_T electrons in case of mini-isolation, the efficiency for identification of such electrons is high with mini-isolation.

To measure the efficiency of an identification or isolation criteria, *tag & probe* (TnP) technique can be used. The decay of Z boson can give a pair of electrons and one the electrons serves as the tag and the other as the probe. By using the 4-momenta of electrons, invariant mass of Z boson can be reconstructed and the distribution of invariant mass has a peak at the mass of Z boson. TnP technique can measure the efficiency of an electron selection both in data and MC simulation. If there are differences in data and MC efficiencies, corrections are applied to MC and these corrections are called as scale factors (SFs). The procedure used to obtain SFs for mini-isolation is described below:

Tag object: It is a well identified electron with very strict criteria on its properties. This object needs to have $p_T > 30$ GeV and $|\eta| < 2.17$ and matched with any of the electron HLT trigger objects. The matching criteria is $\Delta R(\text{Tag}, \text{HLT object}) < 0.3$.

Probe object: It is the electron whose selection efficiency needs to be measured and it has charge opposite to that of tag. This object is required to pass a multivariate technique based electron identification criteria which does not use isolation variables.

The invariant mass of tag and probe pairs should fall within 60 - 120 GeV so that these pairs are more likely to arise from the decays of Z bosons. Figure 3.57 shows the invariant mass distribution of tag and probe pairs in data collected in 2016 for events with probe $p_T \in 35 - 50$ GeV and $\eta < 0.8$. The left distribution corresponds to events in which probe object passes min-isolation criteria and right distribution corresponds to events in which probe fails mini-isolation criteria.

This distribution is fitted with a signal function plus background function as shown in red. The signal function used is MC template with Gaussian smearing, and the background function is CMS shape function which is shown in blue. The CMS shape function is a product of falling exponential and error function [72]. The efficiency is given by

$$\epsilon = \frac{\text{Events with passing probe}}{\text{Events with passing probe} + \text{Events with failing probe}} \quad (3.12)$$

The number of events passing or failing probe can be determined by taking the area under the signal function from left and right distributions shown in figure 3.57. The efficiency is found to be 0.97 with negligible statistical uncertainty. The efficiency in

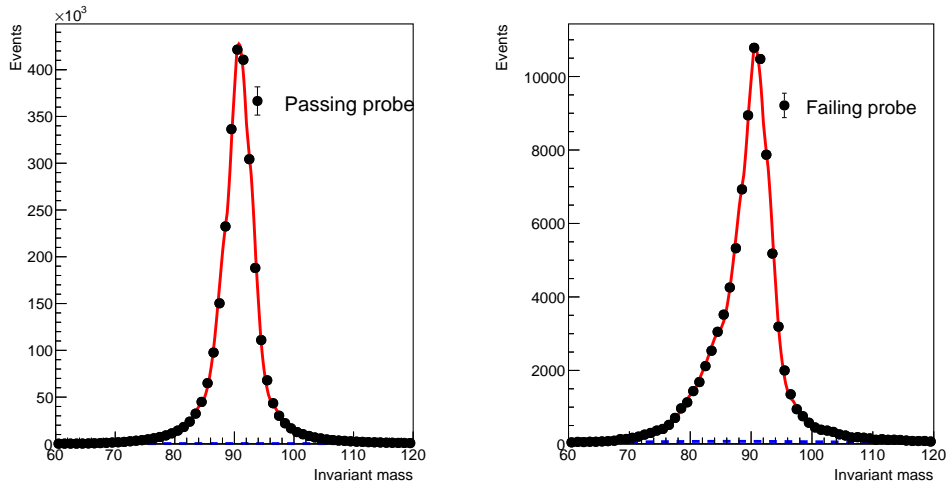


FIGURE 3.57: The left (right) plot shows the invariant mass distribution of tag and probe passing (failing) mini-isolation criteria.

MC can be obtained by using the template, or using generator level information to select events from Z boson decays.

The whole procedure can be repeated by taking other $p_T - \eta$ ranges and calculate the efficiency. To evaluate the systematic uncertainty, refitting is done using different signal function (Crystal-Ball with Gaussian smear) and background function (exponential). Systematic uncertainty because of the choice of tag is evaluated by making a different tag selection. Figure 3.58 shows the efficiency (top panel) and SFs (bottom panel) for various η regions as a function of p_T .

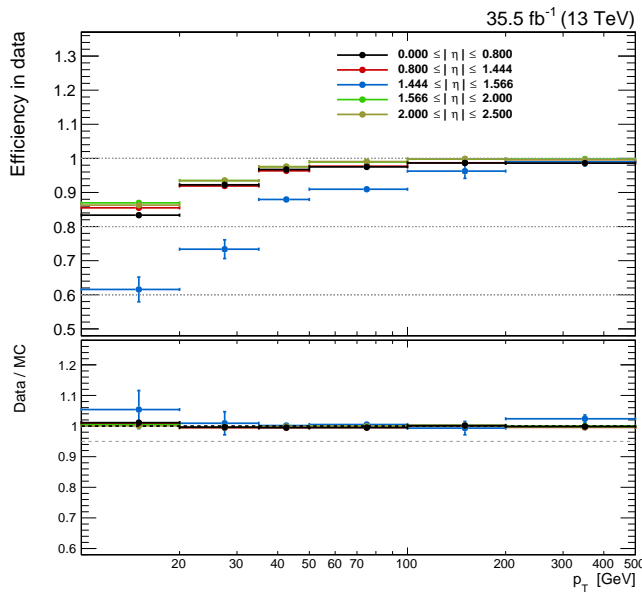


FIGURE 3.58: The efficiency of mini-isolation in data (top panel) as a function of electron p_T for various η regions and the bottom panel shows the SFs. The error bars include systematic and statistical uncertainties.

These SFs account for any discrepancies in data and MC and they are applied on

MC. In a similar way the SFs are derived to account for discrepancies at track reconstruction level, identification, and isolation (as mentioned here for mini-isolation). Wherever needed, these type of corrections are applied to other physics objects as well.

3.5.5 Jets

Hadronization of quarks and gluons results in formation of many mesons and baryons which is referred to as a jet, deposits its energy mostly in HCAL. On an average 65% of the total energy of the jet is carried by charged hadrons, 25% by photons and 10% neutral hadrons. Figure 3.59 shows the jet energy fraction as a function of p_T in data and simulation. The lower panel shows the difference in data and simulation.

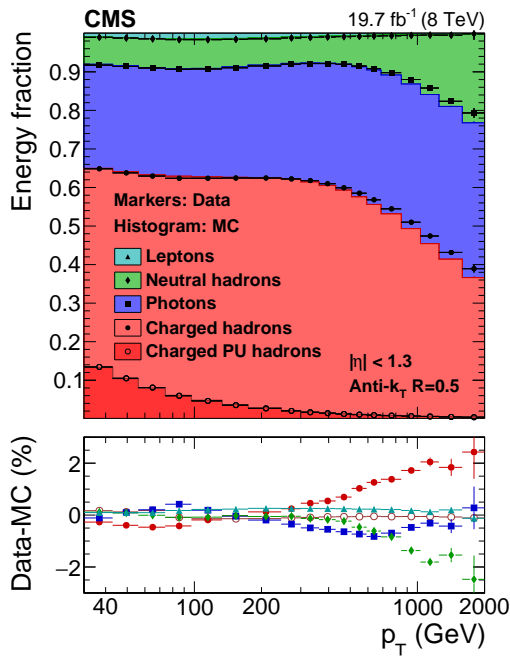


FIGURE 3.59: Energy composition in jets as a function of jet p_T in data and MC simulation [61].

Jets are reconstructed using PF candidates using anti- k_T algorithm [66, 67] with a size parameter of 0.4. These jets are called as AK4PF jets. They are also subject to pileup mitigation using charged hadron subtraction (CHS). In CHS, charged hadrons associated to vertices apart from primary vertex are removed from PF candidates. To remove remaining energy due to charged hadrons and neutral hadrons, jet area based pileup corrections are applied on an event by event basis. The distance parameters used in jet clustering are:

$$d_{ij} = \min(p_{Ti}^{2n}, p_{Tj}^{2n}) (\Delta_{ij}^2 / R^2) \quad (3.13)$$

$$d_{iB} = p_{Ti}^{2n} \quad (3.14)$$

$$\text{where } \Delta_{ij}^2 = (y_i - y_j)^2 + (\phi_i - \phi_j)^2 \quad (3.15)$$

The values of R and n for AK4 jets are 0.4 and -1 respectively. d_{ij} is the distance between entities (particles or pseudojets) i and j , d_{iB} is the distance between i and the beam (B), y_i is rapidity and ϕ_i is the azimuthal angle of i th particle. The jet clustering proceeds iteratively by combining *nearest* particles. In the case of anti- k_T ,

the d_{ij} between similarly separated soft particles is higher than the d_{ij} between a hard particle and soft particle. The soft particles in this algorithm do not modify the shape of the jet, but the hard ones do.

The measured energy or the p_T of the jet needs to be corrected so that its measured 4-momentum is close to parton level 4-momentum. There are several reasons for imperfect measurement of jet energy such as pileup energy contribution, non-uniformity of detector response to different jet energy etc. The jet energy corrections (JECs) aim to correct the jets and determine the momentum of the initial parton. The

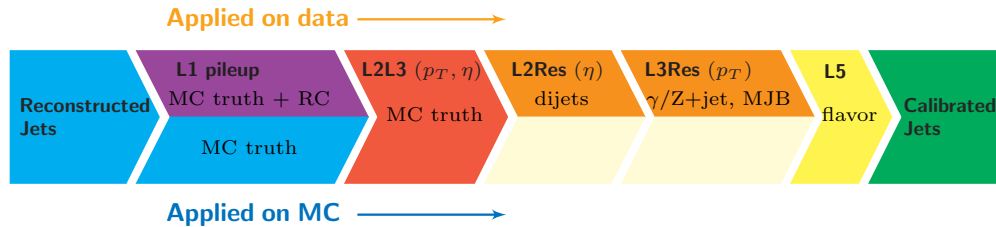


FIGURE 3.60: Pictorial representation of various steps in application of JECs on data and MC simulation [73].

corrections are derived at different levels (L1, L2 and L3) and the output of each level becomes the input for the other, in other words a factorized approach is followed for applying the corrections. Figure 3.60 shows a pictorial representation of different steps in applying JECs both on data and MC simulation. The corrected 4-momenta of the jet can be written as [74]:

$$p_\mu^{corr} = \mathcal{C} p_\mu^{raw} \quad (3.16)$$

where $\mathcal{C} = C_{\text{offset}}(p_T^{\text{raw}}) \cdot C_{\text{MC}}(p'_T, \eta) \cdot C_{\text{rel}}(\eta) \cdot C_{\text{abs}}(p''_T)$ (3.17)

The offset correction, C_{offset} removes extra energy due to pileup and noise, MC calibration factor, C_{MC} removes bulk of non-uniformity in η and non-linearity in p_{T} , C_{rel} and C_{abs} are relative and absolute energy scale corrections which account for small differences in data and MC. In the expression for \mathcal{C} , p'_{T} is the p_{T} of the jet after offset correction, p''_{T} is the p_{T} of the jet after all previous corrections. Figure 3.61 shows the average jet p_{T} response with and without corrections at a few stages of JEC application. The p_{T} response is defined as the average value of ratio of measured jet p_{T} to particle-level jet p_{T} , $p_{T,\text{ptcl}}$.

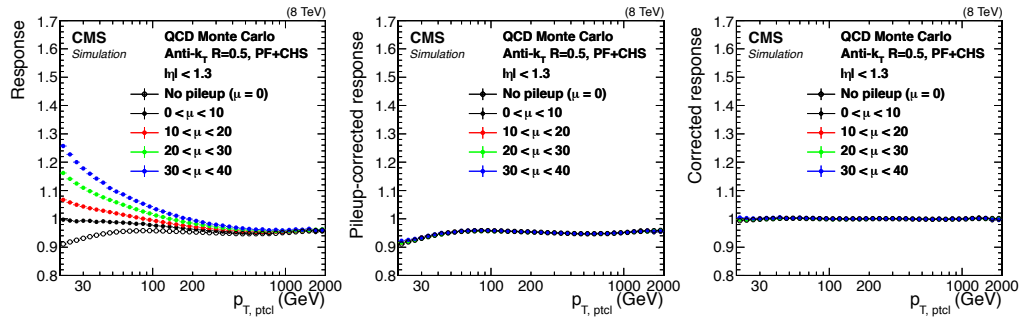


FIGURE 3.61: Average jet p_T response in QCD MC at different stages of JECs. The left plot is without any corrections, middle plot is for after pileup offset corrections and the right plot is after applying all the JECs. μ refers to the average number of pileup interactions per bunch crossing.

The resolution of AK4PF jet as a function of ref jet is shown in 3.62. The uncertainty in the jet energy correction is about 2% for barrel region jets with p_T of 30 GeV [75].

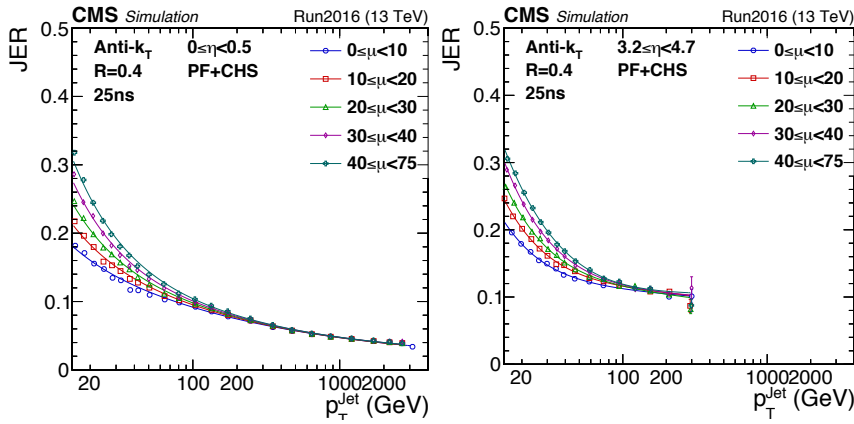


FIGURE 3.62: Resolution of PF jets as a function of p_T in the barrel and endcap regions [76].

3.5.6 Tagging of b-quark jet

The mass of b-quark is about 4.2 GeV and the hadrons formed from b-quark have masses of 5-6 GeV. The lifetime, τ of b-hadrons is about 1.5 ps and this corresponds to $c\tau$ value of 0.45 mm. If the momentum of b-hadron is about 200 GeV, the mean decay length is about 2 cm in the lab frame and this increase in decay length is because of Lorentz-boost. With the high position resolution of tracker, it is possible to identify such decays which take place away from the primary vertex (PV). These decay vertices are called secondary vertices and the impact parameter (IP) for such decays is high. In many cases, b-hadron decays result in a soft lepton. Figure 3.63 illustrates a b-jet containing a soft lepton and a secondary vertex (SV).

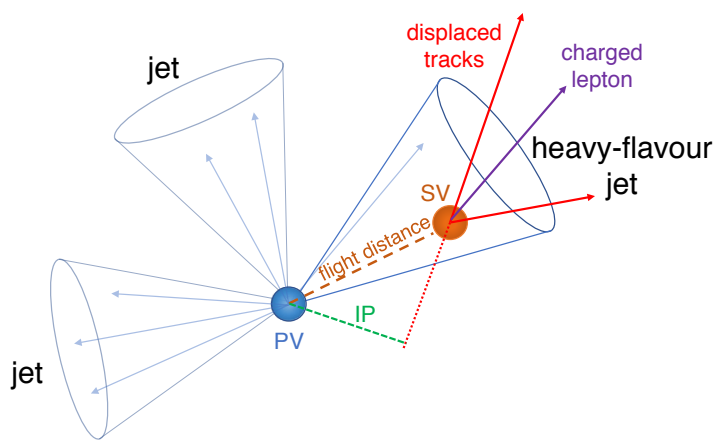


FIGURE 3.63: Illustration of a b-jet showing the decay of a b-hadron and a soft lepton inside the jet [77].

The algorithm used for identifying whether a jet is b-jet or not, is called combined SV version-2 (CSVv2) algorithm [77] which combines information about the displaced tracks and the SVs associated with a jet using a multivariate technique.

The output of the CSVv2 algorithm is shown in figure 3.64 (left) for u, d, s or gluon jets, c-jets and b-jets in simulated $t\bar{t}$ events. A neural network based CSVv2 tagger (DeepCSV) is also used by CMS.

The plot on the right side of figure 3.64 shows the efficiency for b-tagging using CSVv2 and DeepCSV as a function of particle-level jet p_T . These efficiencies are obtained from simulation after applying data to simulation corrections. The b-tagged jets (or b-jets) used in this search use CSVv2 - medium working point which has a 55% efficiency to correctly identify b-jets with $p_T \approx 30$ GeV. The corresponding misidentification probabilities are 1.6% for gluon and light-flavor quark jets, and 12% for charm quark jets.

The efficiency of b-tagging is low at low p_T because of multiple Coulomb interactions and lower Lorentz-boost making the SV closer to PV. At high jet p_T , tracks in the jets are collimated and the curvature of the tracks are small which may cause close-by tracks to create overlapping hits in the tracker and hence the efficiency decreases.

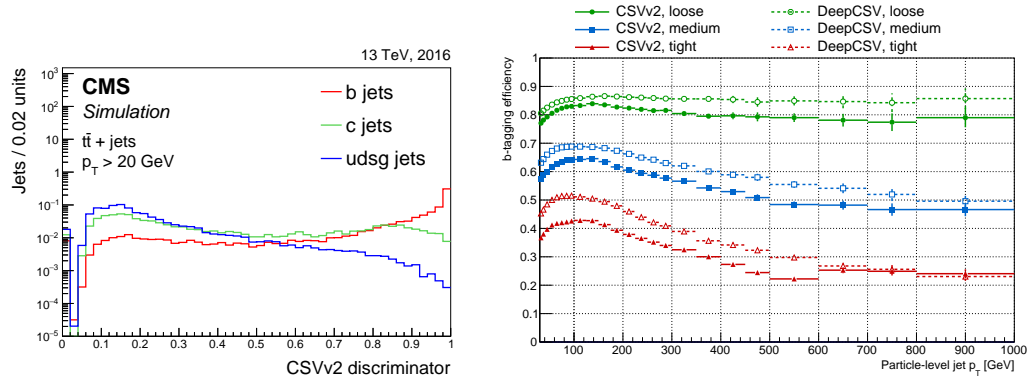


FIGURE 3.64: The output of the CSVv2 algorithm for different flavor jets (left) [77]. The right plot shows the efficiency of b-tagging for CSVv2 and DeepCSV as a function of particle-level jet p_T [78].

3.5.7 Missing transverse momentum

The protons are accelerated in z direction and hence the momentum before the collision in x and y directions, transverse direction, is zero. From momentum conservation, final momentum after the collision in transverse direction should be zero. If there are n PF candidates each of them having a transverse momentum vector \vec{p}_T^i , and a neutrino with transverse momentum vector \vec{p}_T^ν , we have

$$0 = \sum_i^n \vec{p}_T^i + \vec{p}_T^\nu \quad (3.18)$$

$$\vec{p}_T^\nu = - \sum_i^n \vec{p}_T^i \quad (3.19)$$

$$p_T^{miss} = |\vec{p}_T^\nu| = \left| - \sum_i^n \vec{p}_T^i \right| \quad (3.20)$$

The transverse momentum of neutrino, \vec{p}_T^ν is nothing but the negative vector sum of all PF candidates. Magnitude of this vector is referred to as p_T^{miss} and it gives the exact p_T of neutrino if we detect and reconstruct all other particles and measure their transverse meomentum accurately. If there are multiple neutrinos or new particles

which do not interact with detector, then their momenta get added vectorially and their net effect is reflected in p_T^{miss} . If PF algorithm is not able to reconstruct and

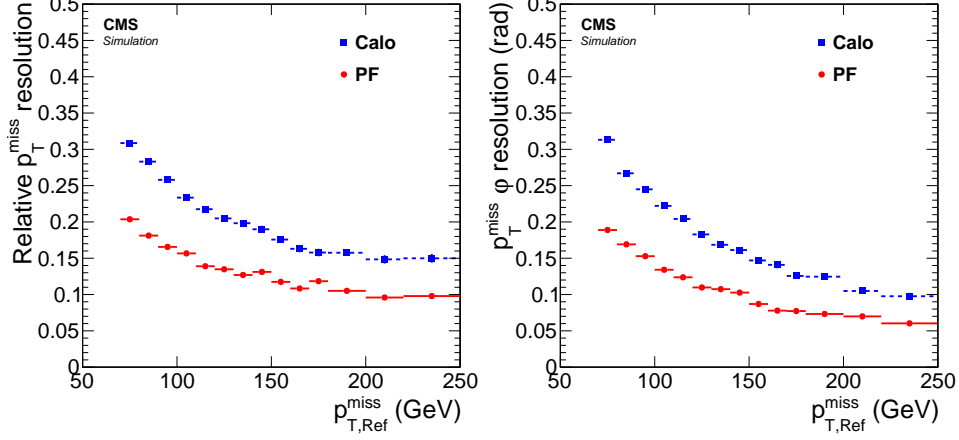


FIGURE 3.65: Relative p_T^{miss} resolution (left) and $p_T^{miss}-\phi$ resolution as a function of $p_{T, \text{ref}}^{miss}$ in simulated $t\bar{t}$ sample [61].

get accurate measurement of momenta all the particles, either because of detector imperfections or finite resolution while measuring momenta of various objects, we get incorrect measure of p_T^{miss} . The amount of *incorrectness* is termed as fake p_T^{miss} . As discussed, earlier, jets need various types of corrections to estimate their true 4-momenta. Once the jets are corrected, these corrections need to be propagated to p_T^{miss} since corrections on jets do not affect PF candidates. The corrected p_T^{miss} is given by

$$\vec{p}_T^{miss, corr} = \vec{p}_T^{miss} - \sum_{\text{jets}} (\vec{p}_{T,jet}^{\text{corr}} - \vec{p}_{T,jet}) \quad (3.21)$$

This p_T^{miss} is called *type1 corrected* p_T^{miss} and it uses all jets with $p_T > 15$ GeV and having ECAL energy not more than 90% of the total jet energy. If there is a muon in the jet, then 4-momenta of the muon is subtracted from the jet, corrections are applied, 4-momenta of muon is added back to the corrected jet [79].

All the physics objects, electrons, muons, photons, muons and jets (to large extent), play a role in resolution of p_T^{miss} . Figure 3.65 shows the relative resolution of p_T^{miss} (left) and $p_T^{miss}-\phi$ (right) as a function of $p_{T, \text{ref}}^{miss}$, where $p_{T, \text{ref}}^{miss}$ is calculated using all stable particles, except neutrinos, from the event generator [61].

Chapter 4

Search for supersymmetry in events with a photon, jets, b-jets, and missing transverse momentum

4.1 Introduction

This chapter describes a search for SUSY in events with one photon, large missing transverse momentum (p_T^{miss}), and large hadronic activity. The targeted production mechanism is described by simplified models of gluino and stop production as depicted in Figure 4.1, though the analysis is more generically applicable to other production scenarios. This analysis focuses on SUSY models in which R-parity is conserved forcing the lightest supersymmetric particle (LSP), to be stable weakly interacting, leading to potentially large p_T^{miss} .

In general, gluinos and squarks will decay to at least one colored SM particles and the LSP through some number of supersymmetric particles in the form of cascades. Other SM particles, such as vector bosons or Higgs boson, can be produced in these cascades. Massive SM boson decay predominantly to hadronic final states. In particular, the Higgs boson decays predominantly to a pair of b-quarks. In addition to heavy flavor from Z and Higgs bosons, heavy flavor quarks can come from top and bottom squarks. These cases are particularly motivated by naturalness arguments, where squarks at least partially cancel the leading contributions of virtual corrections to the Higgs mass from SM particles (Figure 2.3).

Given the reasons stated above, final states with high jet and b-jet multiplicities and at least one photon are particularly well-motivated by the GMSB symmetry breaking mechanism and naturalness considerations. Depending on the topology, these jets can arise from either light-flavored quarks (u, d, s, c) or b quarks. We study four simplified models; example diagrams depicting these models are shown in Fig. 4.1. Three models involve gluino pair production (prefixed with T5), and one model involves top squark pair production (prefixed with T6). For the gluino models, we assume all supersymmetric particles apart from gluino, neutralino and gravitino, are very heavy (generally the mass is chosen to be 100 TeV) and inaccessible at the LHC. In the top squark model, we assume all supersymmetric particle masses are very large, except the mass of top squark, neutralino and gravitino. In the T5qqqqHG model, each gluino decays to a pair of light-flavored quarks ($q\bar{q}$) and a neutralino. The T5bbbbZG and T5ttttZG models are similar to T5qqqqHG, except that the each pair of light-flavored quarks is replaced by a pair of bottom quarks ($b\bar{b}$) or a pair of top quarks ($t\bar{t}$), respectively. In the T5qqqqHG model, the $\tilde{\chi}_1^0$ decays either to an SM Higgs boson and a \tilde{G} or to a photon and a \tilde{G} . The $\tilde{\chi}_1^0 \rightarrow H \tilde{G}$ branching fraction is assumed to be 50%, and the smallest $\tilde{\chi}_1^0$ mass considered is 127 GeV. In

the T5bbbbZG and T5tttZG models, the neutralinos decay to $Z\tilde{G}$ and $\gamma\tilde{G}$ with equal probability. The T6ttZG model considers top squark pair production, with each top squark decaying into a top quark and a neutralino. The neutralino can then decay with equal probability to a photon and a \tilde{G} or to a Z boson and a \tilde{G} . For the models involving the decay $\tilde{\chi}_1^0 \rightarrow Z\tilde{G}$, we probe $\tilde{\chi}_1^0$ masses down to 10 GeV. All decays of supersymmetric particles are assumed to be prompt i.e. the decays take place much before the first layer of detector.

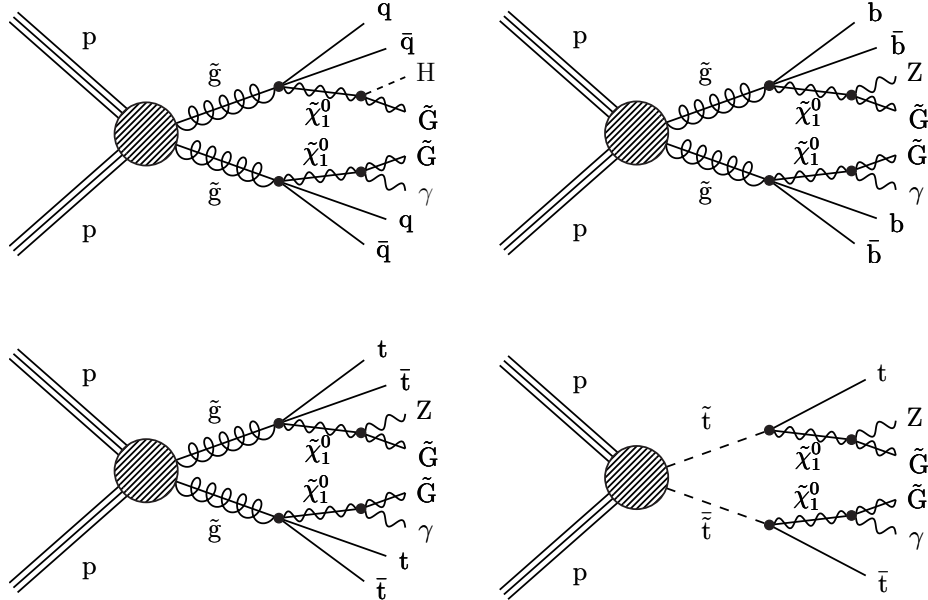


FIGURE 4.1: Example diagrams depicting the simplified models used, which are defined in the text. The top left diagram depicts the T5qqqHG model, the top right diagram depicts the T5bbbbZG model, the bottom left diagram depicts the T5tttZG model, and the bottom right depicts the T6ttZG model.

In all models, the mass \tilde{G} is fixed to be 1 GeV, to be consistent with other published results of CMS experiment. To estimate the impact of \tilde{G} mass on the kinematics of photon and \tilde{G} , the mass of \tilde{G} was changed to 1 MeV and 1 keV. The p_T spectrum of photon, the p_T of \tilde{G} and the transverse component of total momentum of gravitinos were found to be similar in all the three \tilde{G} mass scenarios. The mass of gluino is large and hence $\tilde{\chi}_1^0$ has large momentum which results in high momentum decay products irrespective of 1 GeV or 1 MeV or 1 keV \tilde{G} mass. The lowest $\tilde{\chi}_1^0$ mass considered for this study is 10 GeV. There *may be* significant impact on the search if very low $\tilde{\chi}_1^0$ masses (~ 1 GeV) are considered. However in those cases, actual physics models instead of SMS need to be considered because the branching ratio for $\tilde{\chi}_1^0 \rightarrow \gamma + \tilde{G}$ can be higher than 50%. For the *parameter space explored in this search*, the kinematic properties do not depend strongly on the exact value of \tilde{G} mass.

The analysis presented here [80] is an extension of existing single photon analysis previously [81], by taking full advantage of p_T^{miss} , large hadronic activity, and heavy flavor content. The analysis will search for large p_T^{miss} events in various regions of jet multiplicity and b-jet multiplicity, motivated by several SMS scenarios. The SM backgrounds are estimated from data control regions with as little reliance on simulations as possible. Section 4.2 discusses the SM and signal simulations used in the analysis. The triggers used for both the signal and control regions are described in Section 4.3. Event selections are detailed in Section 4.4. The background estimation techniques are discussed in Section 4.6. Signal systematic uncertainties are described

in Section 4.7. Finally, results and a description of our statistical modeling of data and the inferred limits are described in chapter 5.

4.2 MC simulation samples

Monte Carlo simulation is used to design the analysis, to provide input for background estimation methods that use data control regions, and to predict event rates from simplified models. Simulated SM background processes include jets produced through the strong interaction, referred to as quantum chromodynamics (QCD) multijets, $t\bar{t}$ +jets, W +jets, Z +jets, γ + jets, $t\bar{t}\gamma$, $t\gamma$, and $V\gamma$ + jets ($V = Z, W$). The SM background events are generated using the `MADGRAPH5_aMC@NLO` v2.2.2 or v2.3.3 generator [82, 83, 84] at leading order (LO) in perturbative QCD, except $t\bar{t}\gamma$ and $t\gamma$, which are generated at next-to-leading order (NLO). The cross sections used for normalization are computed at NLO or next-to-NLO [82, 85, 86, 87]. The QCD multijets, diboson ($V\gamma$), top quark, and vector boson plus jets events are generated with up to two, two, three, and four additional partons in the matrix element calculations, respectively. Any duplication of events between pairs of related processes—QCD multijets and γ + jets; $t\bar{t}$ +jets and $t\bar{t}\gamma$; W +jets and $W\gamma$ + jets—is removed using generator information.

The NNPDF3.0 [88] LO (NLO) parton distribution functions (PDFs) are used for samples simulated at LO (NLO). Parton showering and hadronization are described using the PYTHIA 8.212 generator [89] with the CUETP8M1 underlying event tune [90]. Partons generated with `MADGRAPH5_aMC@NLO` and PYTHIA that would otherwise be counted twice are removed using the MLM [91] and FxFx [92] matching schemes in LO and NLO samples, respectively.

Signal samples are simulated at LO using the `MADGRAPH5_aMC@NLO` generator and their yields are normalized using NLO plus next-to-leading logarithmic (NLL) cross sections [93, 94, 95, 96, 97]. The decays of gluinos, top squarks, and neutralinos are modeled with PYTHIA.

The detector response to particles produced in the simulated collisions is modeled with the GEANT4 [98] detector simulation package for SM processes. Because of the large number of SUSY signals considered, with various gluino, squark, and neutralino masses, the detector response for these processes is simulated with the CMS fast simulation [99, 100]. The results from the fast simulation generally agree with the results from the full simulation. Where there is disagreement, corrections are applied, most notably a correction of up to 10% to adjust for differences in the modeling of p_T^{miss} .

4.3 Triggers

The analysis phase space is partly driven by the availability of single photon triggers. We make use of two single photon triggers for both the signal region and all control regions. For the fake-rate background prediction, which relies on extrapolating from single electron events, we also make use of single electron triggers. For validating the multijet backgrounds, where p_T^{miss} is dominated by jet mis-measurement, we make use of a zero photon control region, which is triggered using the inclusive H_T triggers.

These three triggering strategies and studies of their efficiencies are discussed in the following sections.

4.3.1 Signal triggers

The signal events for are triggered using a logical OR of HLT_Photon90_CaloIdL_PFHT600 and HLT_Photon165_HE10 which require either a photon with $p_T > 90$ GeV photon and $H_T > 600$ GeV, or a photon with $p_T > 165$ GeV respectively. In addition, photons need to have $H/E < 0.10$. Both of these triggers are seeded by level-1 triggers that are based on energy deposited in the ECal. The trigger efficiencies are studied using MET dataset by taking OR of inclusive p_T^{miss} triggers : HLT_PFMET*_PFMHT*_IDTight, where * corresponds to 90, 100, 110 & 120. Efficiency of the trigger is given by

$$\epsilon = \frac{\text{Events passing photon trigger(s) \& MET triggers}}{\text{Events passing MET triggers}} \quad (4.1)$$

Figure 4.2 shows the efficiency of the Photon165 trigger versus p_T^γ for different data-taking eras and for all 2016 data. No conditions are imposed on kinematic variables, except that the events should have at least one photon with $p_T > 100$ GeV. This trigger becomes fully efficient for $p_T^\gamma > 190$ GeV and has a plateau efficiency of 97.6%.

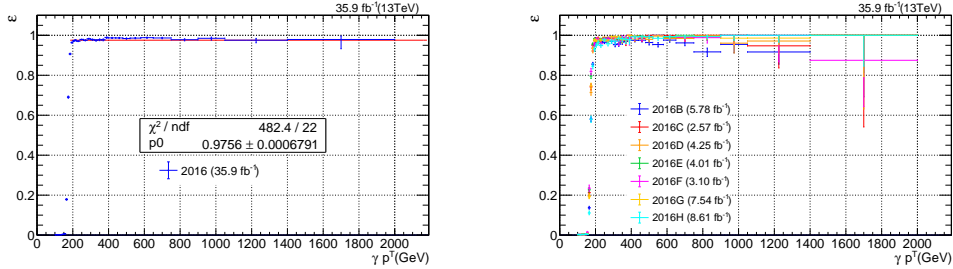


FIGURE 4.2: Efficiency of Photon165 trigger versus p_T^γ for all eras (left) and split by eras (right).

For measuring the efficiency of the Photon90_PFHT600 trigger as a function of p_T^γ , $H_T^\gamma > 900$ GeV is used. To measure the efficiency as a function of H_T^γ , $p_T^\gamma > 100$ GeV is used. Figure 4.3 shows the efficiency of the Photon90_PFHT600 trigger versus both p_T^γ , for events with $H_T^\gamma > 900$ GeV , and versus $H_T^\gamma (p_T^\gamma + \sum_{\text{jets}} p_T^{\text{AK4}})$, for events with $p_T^\gamma > 100$ GeV. Efficiencies are presented both separated by eras and for all 2016 data combined. The trigger is fully efficient for $H_T^\gamma > 800$ GeV, but has an inefficiency at high H_T^γ . This inefficiency is ultimately recovered by the Photon165 trigger. The Photon90_PFHT600 is found to be fully efficiency for $p_T^\gamma > 100$ GeV for high H_T^γ events. At plateau, the efficiency is > 95% as a function of H_T^γ or p_T^γ .

The combined efficiency from the OR of the Photon165 and Photon90_PFHT600 triggers is shown in Figure 4.4. This efficiency is measured by considering events with at least 2 jets and the following condition: ($H_T^\gamma > 500$ & $p_T^\gamma > 190$) OR ($H_T^\gamma > 800$ & $p_T^\gamma > 100$). The average efficiency is found to be 98% with a negligible statistical uncertainty. The kinematic dependence of the efficiency amounts to a roughly 2% variation and is taken as a systematic uncertainty, where relevant.

The single (tight) electron control region, used for estimating the fake photon background, is also triggered using a logical OR of the Photon165 and Photon90_PFHT600 triggers. To ensure that there is no trigger bias in our estimations, we measure the trigger efficiency for events with a single tight electron, shown in Figure 4.5.

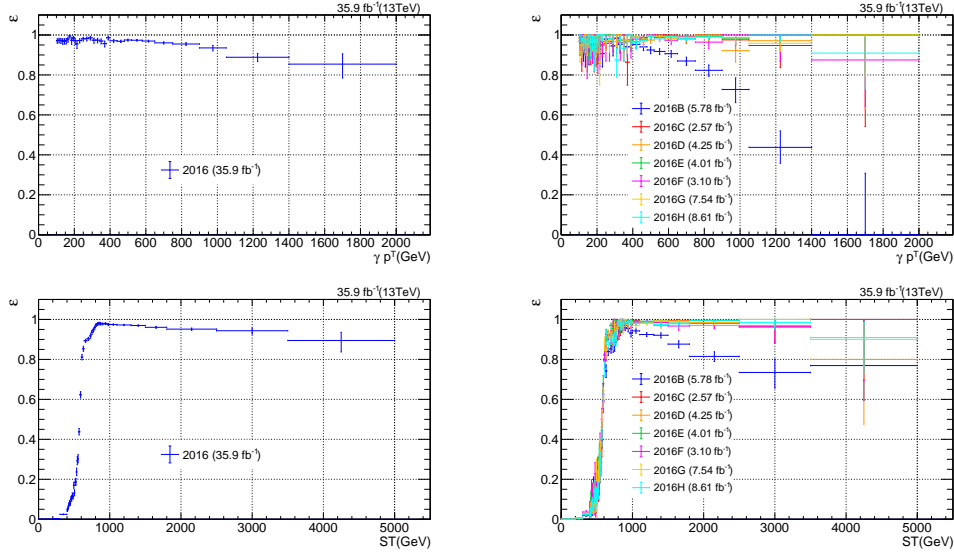


FIGURE 4.3: Efficiency of Photon90_PFHT600 trigger versus p_T^γ (top) and H_T^γ (bottom) for all eras (left) and split by eras (right).

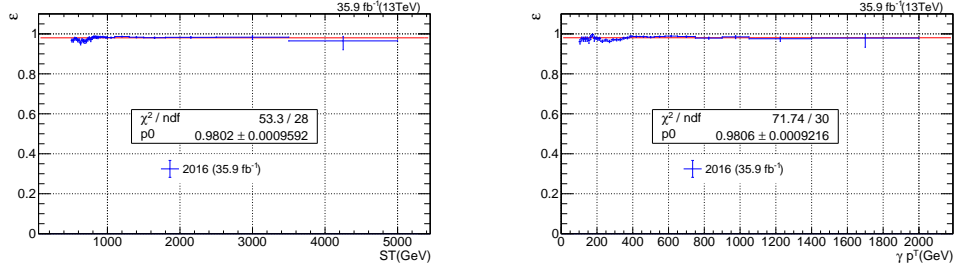


FIGURE 4.4: Efficiency of the OR of the Photon165 and Photon90_PFHT600 triggers versus H_T^γ (left) and p_T^γ (right).

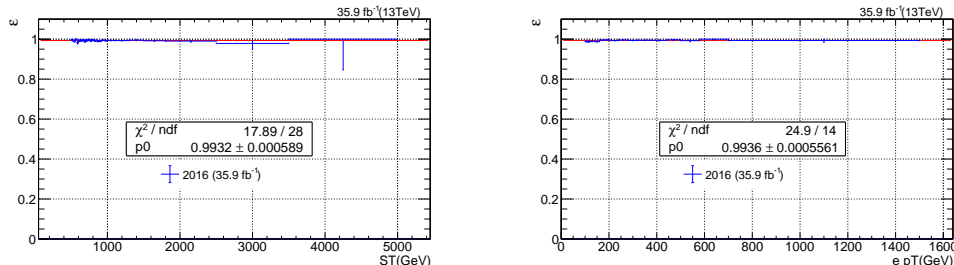


FIGURE 4.5: Efficiency of the OR of the Photon165 and Photon90_PFHT600 versus H_T^γ (left) and p_T^γ (right) for events with one tight electron.

4.3.2 Multijet triggers

Events with zero photons are used to validate the multijet background predictions. These events are triggered using an OR of the PFHT800 and PFHT900 triggers. The former HLT path is used only for the early data taking, and the later was used throughout 2016 data-taking without any prescaling. These triggers are observed to be inefficient at high H_T . To recover this inefficiency, a single jet trigger is also included, HLT_CaloJet500_NoJetID. The efficiency for these triggers is shown in Figure 4.6, which is measured using events which pass the inclusive PFMET*_PFMHT*_ triggers. The efficiency is found to plateau for at 98% for $H_T > 1000$ GeV. The systematic uncertainty on this is taken to be +2%/-1%.

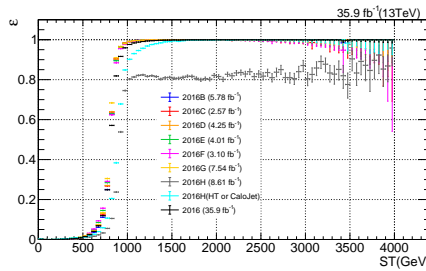


FIGURE 4.6: Efficiency of HLT_PFHT800 trigger for eras B-G, and HLT_PFHT900 OR HLT_CaloJet500_NoJetID for era H for zero photon events.

4.4 Event selection

The search regions for the analysis require large p_T^{miss} , large H_T^γ , one high energy photon, and no leptons. Jets used in this analysis are reconstructed from charged-hadron subtracted particle-flow (PF) candidates using the anti- k_T algorithm [66] with the distance parameter 0.4. The PF algorithm is used to individually identify and reconstruct all particles produced in the collision (PF candidates); namely charged hadrons, photons, neutral hadrons, muons, and electrons [61]. The following requirements define the baseline selection:

- $H_T^\gamma > 500$ GeV for events with $p_T^\gamma > 190$ GeV, and $H_T^\gamma > 800$ GeV for events with $p_T^\gamma > 100$ GeV, where $H_T^\gamma = p_T^\gamma + \sum_{\text{jets}} p_T^{\text{AK4}}$. The photon reconstruction and identification is described in the following.
- Photons: Photons are selected using ID criteria described in 3.5.4. Photon candidates whose supercluster is found to be in the pseudorapidity range of $1.44 < |\eta| < 1.56$, which is the EB-EE transition region are not considered. Photons are required to have $p_T > 100$ GeV and $|\eta| < 2.5$.
- AK4PF jets used in this analysis are required to have $p_T > 30$ GeV, $|\eta| < 2.4$ and pass the loose jet ID requirements [101]:
 - For jets with $|\eta| < 2.4$:
 - neutral hadron fraction < 0.99 ,
 - neutral EM fraction < 0.99 ,
 - number of constituents > 1 ,
 - charged hadron fraction > 0 ,

- charged multiplicity > 0 ,
- charged EM fraction < 0.99

Jets that are matched to isolated photons, within $\Delta R < 0.3$ are not subject to these requirements.

- Tagging of b-jets:

Although not used for a selection criterion, the number of selected jets satisfying the combined inclusive secondary vertex b-tagging algorithm at the medium working point ($\text{CSVv2M} > 0.8484$) is used as a discriminating variable [77] and is used for deciding which signal region an event belongs to.

- $p_T^{\text{miss}} > 200 \text{ GeV}$ for signal region and the region $100 - 200 \text{ GeV}$ p_T^{miss} is used in estimation of $\gamma + \text{jets}$ background.
- Angular cut: The majority of $\gamma + \text{jets}$ and QCD multijet events in our high- p_T^{miss} search region have jets with undermeasured momenta and thus a spurious momentum imbalance. A signature of such an event is a jet closely aligned in direction with the p_T^{miss} vector. To suppress this background, we reject all events in which either of the two highest- p_T jets lie within 0.3 radians of the p_T^{miss} vector in the azimuthal coordinate i.e. $\Delta\phi(\vec{p}_T^{\text{miss}}, \vec{p}_{\text{T}}^{\text{jet}}) < 0.3$ for first two leading jets.
- Muon veto: Muon candidates are selected using medium-ID muon selection [57] with the additional requirements on impact parameters (IPs):

$$\begin{aligned} d_{xy}(\mu, \text{PV}) &< 0.2 \text{ cm} \\ d_z(\mu, \text{PV}) &< 0.5 \text{ cm} \end{aligned} \quad (4.2)$$

Muon candidates are required to have $p_T > 10 \text{ GeV}$ and $|\eta| < 2.4$. To distinguish between prompt muons and muons from b-hadron decays, muons are required to satisfy an isolation requirement, $I_{\text{mini}} < 0.2$, where I_{mini} is the mini-isolation variable, whose description is similar to the one in 3.5.4 for electrons. Any event with a muon satisfying all of the above criteria is vetoed.

- Electron veto:

Electron candidates are selected using very loose criteria on its properties, called veto selection. They are required to have $p_T > 10 \text{ GeV}$ and $|\eta| < 2.5$ and satisfy an isolation requirement of $I_{\text{mini}} < 0.1$. Any event with an electron satisfying all of the above criteria is vetoed.

- Isolated track vetoes:

Following the event selection described above, including the muon and electron event vetoes, there is still some background in the search regions from $t\bar{t}$, single-top, and $W+\text{jets}$ events with one $W \rightarrow \ell\nu$ decay. In about half these background events, the W boson decays to a τ lepton and the τ lepton decays hadronically, while in the other half, an electron or muon is not identified or does not satisfy the criteria for an isolated electron or muon candidate given above. To suppress these backgrounds, we reject events with one or more isolated charged track.

The requirements for the definition of an isolated track differ slightly depending on whether the track is identified as leptonic or hadronic by the PF algorithm. For leptonic tracks, we require:

- $p_T > 5 \text{ GeV}$,
- $I_{\text{tk}} < 0.2$,

where I_{tk} is the scalar p_T sum of other charged tracks within $\Delta R < 0.3$ of the primary track, divided by the p_T value of the primary track. For hadronic tracks, we apply slightly tighter requirements:

- $p_T > 10 \text{ GeV}$,
- $I_{\text{tk}} < 0.1$.

Isolated tracks are considered only if they satisfy

$$m_T(\text{tk}, p_T^{\text{miss}}) = \sqrt{2p_T^{\text{tk}} p_T^{\text{miss}} (1 - \cos \Delta\phi)} < 100 \text{ GeV}, \quad (4.3)$$

where p_T^{tk} is the transverse momentum of the track and $\Delta\phi$ is the azimuthal separation between the track and \vec{p}_T^{miss} .

To reduce the influence of tracks from extraneous pp interactions (pileup), isolated tracks are considered only if their nearest distance of approach along the beam axis to a reconstructed vertex is smaller for the primary event vertex than for any other vertex.

- Event cleaning:

We reject events with a jet that satisfies $p_T > 30 \text{ GeV}$ and $|\eta| < 2.4$ if the jet fails the loose jet ID criteria given above. We apply event filters designed to reject events with spurious p_T^{miss} signals [79].

In almost all cases there is a jet matched to a photon within $\Delta R < 0.3$. Since this jet contains photon plus the activity near it, $p_T^{\text{jet}} \geq p_T^\gamma$. Any event which does not have a jet matched to the leading photon or the matching jet p_T is less than p_T^γ is also rejected. This criteria, $p_T^{\text{jet}} \geq p_T^\gamma$, helps in cleaning the data if there are any photon reconstruction failures (Appendix C).

Table 4.1 summarizes various event selections applied to the search region.

TABLE 4.1: List of event selections applied to the search regions.

Variable/object	Selection
Photon	$p_T > 100 \text{ GeV}, \eta < 2.4$
μ	Veto, if $p_T > 10 \text{ GeV} \& \eta < 2.4 \& I_{\text{mini}} < 0.2 \& \text{IP cuts}$
e	Veto, if $p_T > 10 \text{ GeV} \& \eta < 2.5 \& I_{\text{mini}} < 0.1$
Isolated e, μ tracks	Veto, if $p_T > 5 \text{ GeV} \& I_{\text{tk}} < 0.2 \& m_T < 100 \text{ GeV}$
Isolated π^0 tracks	Veto, if $p_T > 10 \text{ GeV} \& I_{\text{tk}} < 0.1 \& m_T < 100 \text{ GeV}$
p_T^{miss}	$> 200 \text{ GeV}$
N_{jets}	$\geq 2, p_T^{\text{jet}} > 30 \text{ GeV}, \eta^{\text{jet}} < 2.4$
H_T^γ	$(> 800 \text{ GeV}) \parallel (> 500 \text{ GeV} \text{ if } p_T^\gamma > 190 \text{ GeV})$
$\min(\Delta\phi_1, \Delta\phi_2)$	> 0.3
Event cleaning filters	Pass

4.5 SM background and search regions

The dominant backgrounds for these high p_T^{miss} , single photons events typically involve either fake p_T^{miss} , from γ -multijet events, or leptonic decays of weak vector bosons, which produce neutrinos. In electroweak events, photons can either arise from a genuine photon, either prompt or non-prompt, or from an electron faking a photon. While prompt and non-prompt photons are not distinguished in this analysis, fakes from electrons are estimated separately. Since photons can be produced from both simulations of matrix elements and parton shower models, via Pythia, MC simulations are often broken up based on whether or not the matrix element includes photons or not.

Figure 4.7 shows the expected distributions of p_T^γ , p_T^{miss} , N_{jets} , $N_{\text{b-jets}}$, and H_T^γ for SM backgrounds and several signal points after the baseline selection mentioned in previous section.

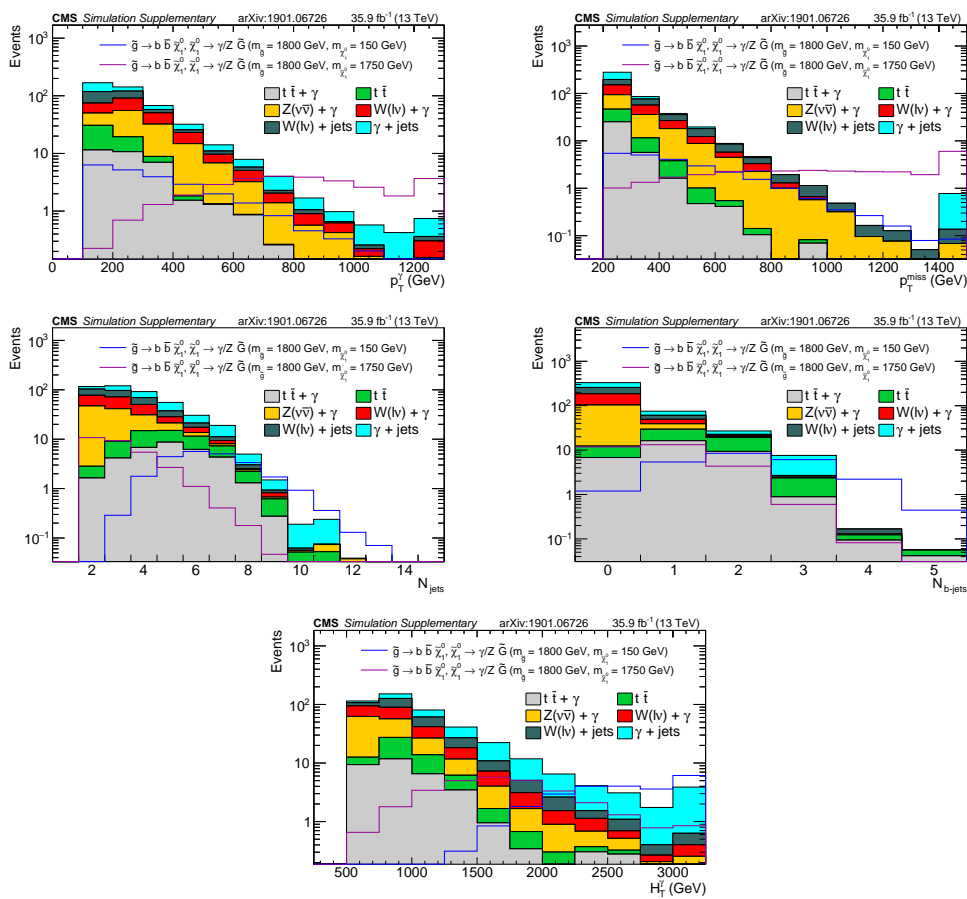


FIGURE 4.7: Distributions of p_T^γ , p_T^{miss} , N_{jets} , $N_{\text{b-jets}}$, and H_T^γ after baseline selection. Filled, stacked histograms represent SM backgrounds, taken directly from simulation, open histograms show two examples of T5bbbbZG signals, one with a high mass (1750 GeV) NLSP and one with a low mass (150 GeV) NLSP. The gluino mass for both signals is 1800 GeV.

Figure 4.8 shows the expected distributions of event yields for SM backgrounds and a few signal model points after the baseline selection. The final statistical interpretations are made using 25 independent signal regions. These regions are defined by N_{jets} , $N_{\text{b-jets}}$, and p_T^{miss} selections. Six groups are defined based on N_{jets} and $N_{\text{b-jets}}$, they are listed in table 4.2 along with 6 sideband regions which are used for fake p_T^{miss}

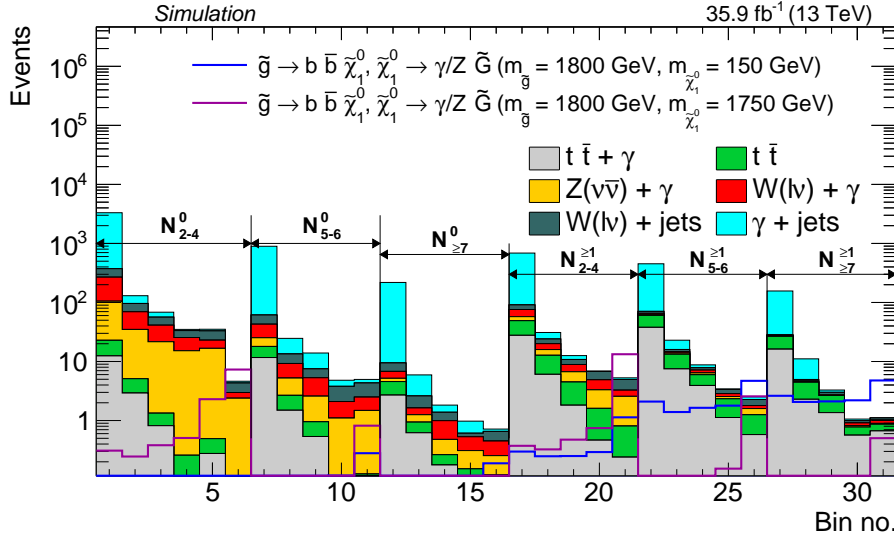


FIGURE 4.8: Distributions of events after baseline selection. Filled, stacked histograms represent SM backgrounds, taken directly from simulation, open histograms show two examples of T5bbbbZG signals, one with a high mass (1750 GeV) NLSP and one with a low mass (150 GeV) NLSP. The gluino mass for both signals is 1800 GeV. The lowest p_T^{miss} bin is not used for final limit calculations.

($\gamma + \text{jets}$ and QCD multijet) background. The sideband regions are not used for the interpretations. Each of these regions, $N_{\text{jets}}^{\text{b-jets}}$, is further divided into 5 p_T^{miss} regions whose boundaries are defined by, $100 < p_T^{\text{miss}} < 200$ (sideband), $200 < p_T^{\text{miss}} < 270$, $270 < p_T^{\text{miss}} < 350$, $350 < p_T^{\text{miss}} < 450$, and $p_T^{\text{miss}} > 450$ GeV. In N_{2-4}^0 the highest p_T^{miss} bin is further split such that the highest p_T^{miss} region corresponds to $p_T^{\text{miss}} > 750$ GeV. The first bin in each of the 6 groups in Figure 4.8 corresponds to $100 \text{ GeV} < p_T^{\text{miss}} < 200 \text{ GeV}$ sideband used for estimation of fake p_T^{miss} background.

TABLE 4.2: Signal region and sideband regions

$N_{\text{b-jets}}$	N_{jets}	Notation ($N_{\text{jets}}^{\text{b-jets}}$)	Bin number	
			Sideband	Signal region
0	2-4	N_{2-4}^0	1	2 - 6
	5-6	N_{5-6}^0	7	8 - 11
	≥ 7	$N_{>7}^0$	12	13 - 16
≥ 1	2-4	$N_{2-4}^{\geq 1}$	17	18 - 21
	5-6	$N_{5-6}^{\geq 1}$	22	23 - 26
	≥ 7	$N_{>7}^{\geq 1}$	27	28 - 31

4.5.1 Optimization of search bins

The above signal region definitions were optimized by maximizing sensitivity to some of the SMS models shown in Figure 4.1. For a given gluino mass if the mass of NLSP is close to mass of gluino mass, then the event has large p_T^{miss} and soft jets leading to low jet multiplicity. On the other hand, if the mass of NLSP is much less than mass of gluino, then there is small p_T^{miss} , but large hadronic activity leading to

many jets in the final state. To cover both of these scenarios, search region is divided in bins of N_{jets} , $N_{\text{b-jets}}$ and p_T^{miss} . Adding $N_{\text{b-jets}}$ binning along with N_{jets} and p_T^{miss} bins gives higher sensitivity if there are any b quarks in the signal model. So these 3 variables are chosen to obtain higher sensitivity. 3 regions are defined based on N_{jets} : 2-4, 5-6 and ≥ 7 . These regions can be represented as N_{2-4} , N_{5-6} , $N_{\geq 7}$. Each of these regions is subdivided into 3 regions based on $N_{\text{b-jets}}$: 0, 1 and ≥ 2 (represented as N^0 , N^1 , $N^{\geq 2}$). This gives total of 9 regions; all these 9 regions are further divided in p_T^{miss} dimension with the following bin boundaries : 100-120, 120-160, 160-200, 200-270, 270-350, 350-450, ≥ 450 . In total there are 63 search bins. This binning can give very good sensitivity, but there will not be enough statistics in the control regions to predict the background. In this analysis, single electron + γ control sample (CS), used for lost electron estimation, is one of the smallest control samples. These 63 bins need to be merged in N_{jets} , $N_{\text{b-jets}}$ or p_T^{miss} to avoid too many bins with 0 CS events; without sacrificing too much on sensitivity. Different ways of merging the bins is studied and for each of them expected exclusion curve is plotted in figure 4.9 for T5qqqqHG (left) and T5bbbbZG (right) models.

In the legends, numbers shown in subscript refers to N_{jets} and superscript refers to $N_{\text{b-jets}}$. These 63 bins are represented as $(N_{2-4}, N_{5-6}, N_{\geq 7}) \times (N^0, N^1, N^{\geq 2})$ with each of these regions subdivided into 7 p_T^{miss} bins.

In figure 4.9, red curve (corresponding to 63 bins) gives the best exclusion, but it has many bins with low CS events. Next best exclusion is obtained with orange curve which corresponds to 7 p_T^{miss} bins \times 3 bins in N_{jets} \times 2 bins in $N_{\text{b-jets}}$. Based on this scenario final search bins are determined. To increase the sensitivity for compressed scenario (mass of gluino is close to mass of NLSP), last p_T^{miss} bin in N_{2-4}^0 is further divided into 450-750 and ≥ 750 GeV.

These optimization studies are done based on MC samples, by considering MC statistical uncertainties and additional 20% uncertainty for each bin and for each of the MC samples, including signal samples.

The final search region starts at $p_T^{\text{miss}} \geq 200$ GeV, whereas in these studies, regions ≥ 100 GeV are also considered. This does not affect the optimization, since $100 < p_T^{\text{miss}} < 200$ GeV region is background enriched and does not contribute to sensitivity.

4.6 Background Estimation

In order to have a robust background prediction over all analysis bins, it is necessary to individually estimate the various background components since the composition is expected to vary dramatically in various bins (Figure 4.10). Low p_T^{miss} regions have more $\gamma + \text{jets}$ background, high p_T^{miss} regions with low N_{jets} or $N_{\text{b-jets}}$ is dominated by processes involving Z or W, and the high p_T^{miss} , high N_{jets} , high $N_{\text{b-jets}}$ region is mainly t \bar{t} +jets or t $\bar{t}\gamma$ dominated.

There are four main sources of background events: events with a lost lepton (lost e/ μ) or a hadronically decaying tau leptons, events in which an electron from a $W \rightarrow e\nu$ decay fakes a photon, $Z \rightarrow \nu\bar{\nu}$ events produced in association with a γ , and fake p_T^{miss} events.

The lost lepton background arises from events in which the charged lepton from a leptonically decaying W, produced directly or from the decay of a top quark, fails to be identified by being out of acceptance, or failing the identification or isolation requirements. For example, in events with high p_T top quarks, the top quark decay products will be collimated, forcing the b-jet to be closer to the charged lepton. In

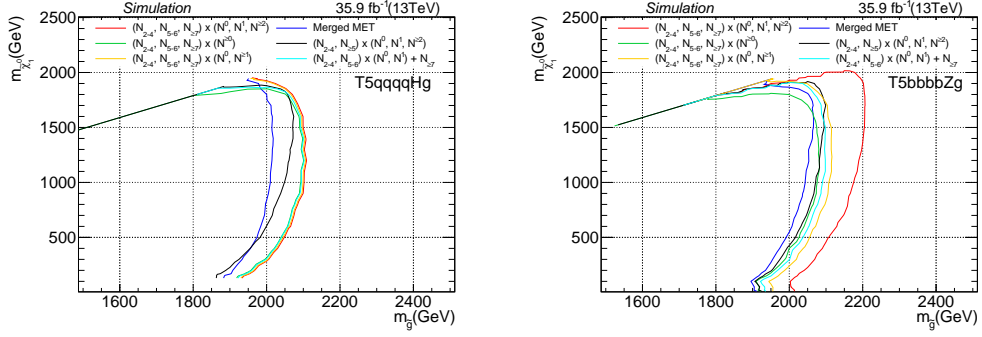


FIGURE 4.9: Expected exclusion curves for different types of binning for T5qqqqHG (left) and T5bbbbZG (right). In the legends, subscript j in N_j^i refers to number of jets and superscript i refers to number of b-tagged jets. The red curve corresponds to 63 search bins defined as $(N_{\text{jets}} = 2-4, 5-6, \geq 7) \times (N_{b\text{-jets}} = 0, 1, \geq 2) \times (7 p_T^{\text{miss}} \text{ bins})$. Other curves are obtained by combining these 63 bins in either N_{jets} or $N_{b\text{-jets}}$ or p_T^{miss} or any combination of these variables. The final binning of the analysis is based on orange curve defined as $(N_{\text{jets}} = 2-4, 5-6, \geq 7) \times (N_{b\text{-jets}} = 0, \geq 1) \times (7 p_T^{\text{miss}} \text{ bins})$.

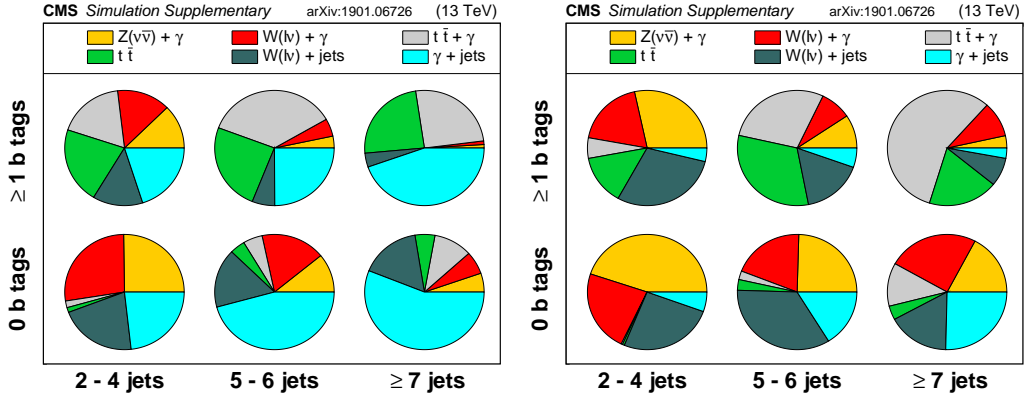


FIGURE 4.10: Pie charts showing relative background composition in various N_{jets} and $N_{b\text{-jets}}$ regions for p_T^{miss} of 200 - 350 GeV on left and $p_T^{\text{miss}} \geq 350$ GeV on right.

these cases, events are more likely to fail the isolation requirements. These events are estimated by studying events with both a well-identified photon and lepton (e/μ) in both data and simulation.

The hadronic- τ background arises from events in which τ leptons from W decays decay to mesons and neutrinos, which occurs $\sim 65\%$ of the time. Due to lepton universality, the fraction of hadronically decaying τ events can be estimated from single muon after correcting for reconstruction differences and for the hadronic- τ branching fraction.

Fake photon events primarily arise from electrons from W decays faking photons. This can happen when a pixel seed fails to be associated with the photon candidate. Given a fake rate, which relates events with well-identified electrons with events with well-identified photons, the fake photon background can be estimated from a single electron (zero photon) control region. The fake rate will be estimated in MC and data/MC corrections are studied to account for any MC mismodeling.

Invisible Z decays constitute a major background for low $N_{b\text{-jets}}$ or N_{jets} multiplicity, high p_T^{miss} events. These events have a natural counter part, $Z(\mu\mu)$ and $Z(ee)$

events, which can be studied in both data and MC to predict the $Z(\nu\nu)$ contribution.

Fake p_T^{miss} events occur primarily in events with a single photon and jets, where one of the jets' energy is mismeasured. These events primarily contribute to the low p_T^{miss} phase space. These events are greatly reduced by requiring events to have a large angle, in the transverse plane, between p_T^{miss} and the leading and subleading jets, $\Delta\phi > 0.3$. There are several control regions that will be used to estimate these events, events with zero photons, events with a photon, but after inverting the $\Delta\phi$ cuts, finally, the whole method will be anchored to the high $\Delta\phi$, photon signal region with low p_T^{miss} . Region $\Delta\phi(p_T^{miss}, \vec{p}_T^{\text{jet}}) > 0.3$ for first two leading jets is defined as high $\Delta\phi$ and low $\Delta\phi$ is the region with does not pass this criteria (one of the jets or both of the jets are aligned, $\Delta\phi < 0.3$, with p_T^{miss}).

4.6.1 Lost lepton estimation

The lost lepton background is estimated from single lepton prompt (e,μ) plus photon control regions. The definition of electrons and muons are the same as those used for the signal region veto defined in Section 4.4. Both the control regions require exactly one lepton (e,μ) and veto the opposite flavor lepton (μ,e). In order to reduce the effect of signal contamination from signals with W bosons, for example, events in the control region are also required to satisfy $m_T = \sqrt{2p_T^\ell p_T^{miss}(1 - \cos(\Delta\phi))} < 100$ GeV. Figure 4.11 shows the distribution of m_T for $\mu\gamma$ events for SM processes and representative signal models (signal is scaled up by a factor of 10). For standard model events, m_T is constrained by the W boson mass, whereas for the signal, missing transverse momentum from the gravitinos is included in m_T . The region with $m_T < 100$ GeV provides a background-enriched sample with very small signal contamination.

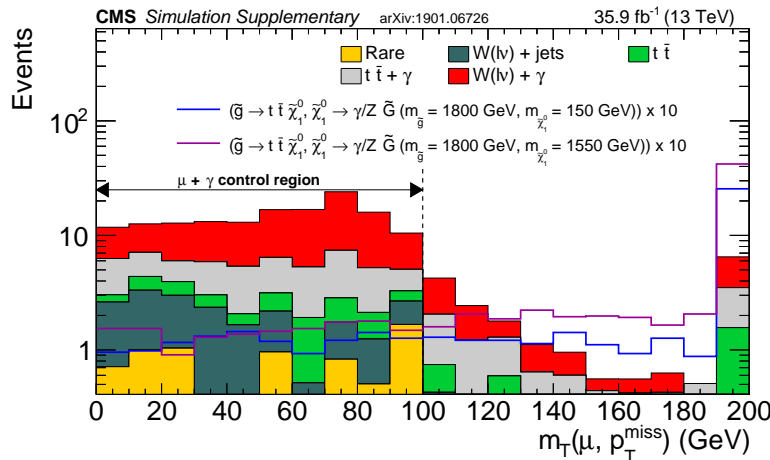


FIGURE 4.11: The transverse mass, m_T distribution for $\mu\gamma$ events. Standard model processes are shown as filled histograms, representative signals of T5tttZG model are shown as solid lines, and the signal is scaled up by a factor of 10 for better visualization.

All other selections for the control region, isolated track vetos, H_T^γ , p_T^{miss} , N_{jets} , and $\Delta\phi$ are the same as the signal region. The control region events are triggered using the same triggers as the signal region and the same trigger efficiency correction/efficiencies are applied.

TABLE 4.3: Parameterization of transfer factors for lost-e and lost- $\mu + \tau_{\text{had}}$ events.

$N_{\text{jets}}^{\text{b-jets}}$	p_T^{miss}	Event weight			
		High- $\Delta\phi$		Low- $\Delta\phi$	
		Lost-e	Lost- $\mu + \tau_{\text{had}}$	Lost-e	Lost- $\mu + \tau_{\text{had}}$
N_2^0	100-150	0.55 ± 0.06	1.05 ± 0.07	0.23 ± 0.04	0.75 ± 0.10
	≥ 150	0.42 ± 0.04	0.84 ± 0.06	0.24 ± 0.04	0.66 ± 0.10
N_3^0	100-150	0.30 ± 0.04	0.81 ± 0.06	0.20 ± 0.04	0.59 ± 0.12
	≥ 150	0.30 ± 0.04	0.67 ± 0.06	0.21 ± 0.04	0.54 ± 0.13
N_4^0	100-150	0.29 ± 0.06	0.62 ± 0.10	0.26 ± 0.08	0.43 ± 0.12
	≥ 150	0.64 ± 0.06	1.23 ± 0.08	0.20 ± 0.04	0.67 ± 0.07
N_{5-6}^0	100-150	0.30 ± 0.02	0.97 ± 0.05	0.16 ± 0.03	0.60 ± 0.07
	≥ 150	0.36 ± 0.03	0.79 ± 0.05	0.11 ± 0.02	0.43 ± 0.05
$N_{\geq 7}^0$	100-150	0.25 ± 0.03	0.64 ± 0.04	0.17 ± 0.03	0.54 ± 0.07
	≥ 150	0.33 ± 0.08	0.73 ± 0.10	0.17 ± 0.05	0.59 ± 0.20
$N_{2-4}^{\geq 1}$	100-150	0.51 ± 0.05	0.87 ± 0.09	0.43 ± 0.06	0.98 ± 0.18
	≥ 150	0.39 ± 0.04	0.70 ± 0.07	0.21 ± 0.06	0.81 ± 0.15
$N_{5-6}^{\geq 1}$	100-150	0.44 ± 0.08	0.64 ± 0.09	0.27 ± 0.09	0.45 ± 0.17
	≥ 150	0.57 ± 0.05	1.11 ± 0.10	0.27 ± 0.04	0.68 ± 0.10
$N_{\geq 7}^{\geq 1}$	100-150	0.35 ± 0.04	0.79 ± 0.07	0.25 ± 0.04	0.54 ± 0.07
	≥ 150	0.36 ± 0.06	0.67 ± 0.10	0.25 ± 0.06	0.53 ± 0.10

The method relies on weighting single lepton events. Event weights are derived from simulations for electron and muon control samples separately. The event weights are derived according to,

$$N_{\text{lost}-\ell}^{\text{pred}} = N_{\ell}^{\text{data}}(p_T^{\text{miss}}, N_{\text{jets}}, N_{\text{b-jets}}) \cdot T^{\text{MC}}(p_T^{\text{miss}}, N_{\text{jets}}, N_{\text{b-jets}})$$

where $T^{\text{MC}}(p_T^{\text{miss}}, N_{\text{jets}}, N_{\text{b-jets}}) = N_{\text{lost}-\ell}^{\text{MC}}(p_T^{\text{miss}}, N_{\text{jets}}, N_{\text{b-jets}}) / N_{\ell}^{\text{MC}}(p_T^{\text{miss}}, N_{\text{jets}}, N_{\text{b-jets}})$

(4.4)

N_{ℓ}^{data} and T^{MC} are the observed yields in the control region and the simulation-derived event weight for a corresponding search region. For the muon ($\ell = \mu$) transfer factors, we include events with zero e, μ , but at least one hadronic- τ in the numerator of the transfer factor.

Table 4.3 shows the event weights for the two lost-lepton control regions. These weights are typically 0.5 (0.75) for the e (μ) control regions.

To test the parameterization of the event weights, the lost lepton method is evaluated on simulated data. Figure 4.12 shows comparisons of the predicted event yield in each of the search regions and the true event yield from simulation for the electron and $\mu + \tau_{\text{had}}$ events. The event weight parameterization is found to predict the true event yield for each of the search regions with the largest observed deviation corresponding to a 30% discrepancy, which is consistent with expectations from statistical fluctuation only. The uncertainty on the event weights from limited MC statistics is propagated to the final predictions. Any non-closure seen in the tighter p_T^{miss} region will be covered by the control sample statistical uncertainty in data.

To model the uncertainty on the prediction due to limited statistics from the single lepton control regions, each prediction will have a prior distribution modeled by a gamma distribution that uses the observed control region statistics and the average transfer factor. The average transfer factor is defined to be the prediction divided by the raw observed control region event yield. In bins where there are no events

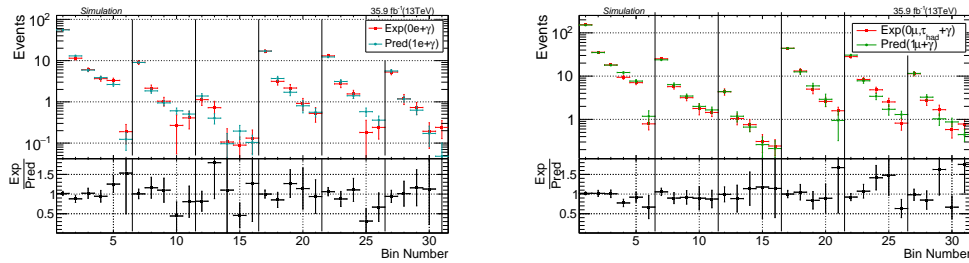


FIGURE 4.12: Expected closure of lost electron (left) and lost $\mu + \tau_{\text{had}}$ (right) predictions where simulated event yields are treated like data.

observed, the average transfer factor is computed based on MC events yields.

Other sources of systematic uncertainty correspond to effects related to:

- lepton scale factors
- b-tagging scale factors
- PDF and scale uncertainties
- modeling of m_T in simulations
- modeling of colinear photons

The PDF and scale uncertainties are studied by varying the MC weights according to 101 and 9 weight sets respectively. For each variation the average transfer factor for all signal regions combined is computed. The maximum variation of the lost $\mu + \tau_{\text{had}}$ average transfer factor is found to be 1.3% and 0.7% for the PDF and scale variations, respectively. The maximum variation of the lost $\mu + \tau_{\text{had}}$ average TF is found to be 1.3% and 0.7% for the PDF and scale variations respectively. For the lost-e, 4.8% and 1.0% variations were found in TF because of the PDF and scale variations, respectively. The maximum variation of these alternative weights is added as a systematic uncertainty on the lost-lepton and τ_{had} prediction. A single nuisance parameter is used to model this uncertainty, correlating all signal regions and correlating the effect of PDF and scale uncertainties for both lost-e and lost- $\mu + \tau_{\text{had}}$ predictions.

The effect of JEC uncertainties are studied by varying both jet p_T and p_T^{miss} . This variation can cause events to migrate below the minimum p_T^{miss} or H_T^γ thresholds, or above the maximum m_T threshold for single lepton events. No trends are observed versus the various signal region. There is a 2% (0.6%) effect on the lost-e (lost- $\mu + \tau_{\text{had}}$) transfer factor, averaged over all signal regions. The 2% effect for the lost-e prediction is applied as a systematic uncertainty. The effect on the lost- $\mu + \tau_{\text{had}}$ prediction is neglected. The same correlation model as used for the PDF and scale uncertainties is applied for the JEC uncertainty systematic.

The modeling of the m_T distribution is potentially effected by generator level cuts in MC samples, but this effect is found to be less than 1% and is neglected.

The effect of uncertainties on the lepton scale factors are propagated to the lost-e and lost- $\mu + \tau_{\text{had}}$ transfer factors. These are found to have a 2% effect, which is assumed to be correlated among common p_T^{miss} bins.

Finally the effect of b-tagging scale factor uncertainties was checked. It was found to have < 1% effect on the lost-lepton transfer factors and is neglected.

Comparisons between simulation and data for single lepton events show a systematic mismodeling of events with small angle between the e/ μ and the photon.

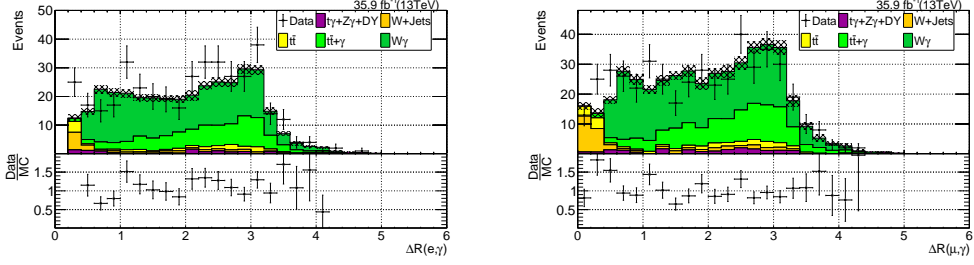


FIGURE 4.13: Distribution of $\Delta R(\ell, \gamma)$ for single electron (left) and single muon (right) events.

This is due to generator level cuts on the angle between photons and partons, in Madgraph $W/t\bar{t} + \gamma$ samples, of $\Delta R < 0.5$, which is not well modeled by pythia $W/t\bar{t}$ +jets samples. Figure 4.13 shows the $\Delta R(e, \gamma)$ and $\Delta R(\mu, \gamma)$ distributions. The region $\Delta R(e, \gamma) < 0.2$ is excluded due to the photon/electron isolation cuts. To assess the effect of the missing low ΔR phase space, the average transfer factor is derived for events with $\Delta R > 0.5$ and compared to the average transfer factor computed with all events. The effect is found to be a 12% effect on the lost-e transfer factor and < 1% on the lost- $\mu + \tau_{\text{had}}$ transfer factor. Since no trends are found versus various signal regions, a flat 12% uncertainty is applied to lost-e prediction. No systematic uncertainty is applied to the lost- $\mu + \tau_{\text{had}}$ prediction.

The observed event yields and the corresponding predictions are shown in Table A.1 (for high $\Delta\phi$) and Table A.2 (for low $\Delta\phi$) of appendix A. Comparisons of the observed yields and expected MC yields for the $e + \gamma$ and $\mu + \gamma$ control regions in Figures B.2 and B.1 of appendix B.

4.6.2 Estimation of events with electrons faking photons

The fake-rate estimation predicts the expected rate from $W(ev)$ events where the electron fakes a photon. The method relies on computing an $e \rightarrow \gamma$ fake rate, derived from a mixture of simulation and data, and applying the fake rate as an event weight to the single electron control region, in which we veto events with a photon.

The kinematic selection for the single electron control region is exactly the same as the single photon control region except that we require exactly zero photons, exactly one electron with tight ID criteria, and use the tight electron 4-vector in place of the photon 4-vector where relevant.

The crux of this method is the derivation of the fake rate. The fake rate in a given region of phase space is defined to be the ratio of events with photons and no electron with respect to events with exactly one tight electron and zero photons. The fake rate will be derived using simulated $W/t\bar{t}$ events. However, due to MC modeling of various nuisances relevant to electron reconstruction, an overall difference is to be expected between data and MC fake-rates. To correct for this, we will also measure the fake-rate in data and MC using DY events with a tag-and-probe (T&P) method. These T&P measurements will be used to correct the fake rates derived on $W/t\bar{t}$ simulations.

The overall prediction is then given by:

$$N_{e \rightarrow \gamma} = N_e^{\text{data}} \cdot f^{tt,W} \cdot \beta^{\text{data}/\text{MC}} \cdot \frac{\epsilon_{SR}^{\text{trig}}}{\epsilon_{CR}^{\text{trig}}}, \quad (4.5)$$

where $f^{tt,W}$ is the fake-rate derived from $W/t\bar{t}$ simulation, β represents the T&P corrections factors, and ϵ represents the measured trigger efficiency.

There are two important parameterizations, namely, $f^{tt,W}$ and β .

Fake-rate parameterization

The fake rate is parameterized as a function of local metrics relevant to electron reconstruction; the electron p_T and the charged track multiplicity, Q_{mult} around the electron are found to give the best closure on MC. The metric Q_{mult} is defined to be the sum of charged PF candidates with the jet matched, $\Delta R < 0.3$, to the electron. Since we require electrons have at least $p_T > 100$ GeV, the jet clustering algorithm almost always clusters the electron into an AK4 jet. On the rare occasions that there is no matched jet, the event is rejected. The distribution of Q_{mult} is shown in Figure 4.14 for DY, $W+jets$, and $t\bar{t}$ events.

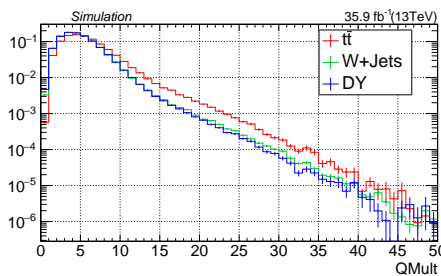


FIGURE 4.14: Q_{mult} distribution in a jet matched to the electron in DY, $W+jets$, and $t\bar{t}$ events. Each of these distributions are scaled to unit area.

When deriving the fake-rate from simulation events are divided into two categories, signal region (SR) events, and control region (CR) events. Signal region events are those with zero electrons found and an EM objects matched, $\Delta R < 0.2$, to a gen-level electron. Control region events are those with 1 tight electron ($p_T > 100$ GeV), exactly zero photons, and $m_T(e, p_T^{miss}) < 100$ GeV; the last requirement increases the purity of the control sample and avoids overlap with signal events. After these selections are applied, the fake rate is then defined as $f^{tt,W} = N_{SR}/N_{CR}$.

Table A.3 shows the parameterization of the fake rate that is used. To validate this parameterization, the fake rate method is applied to MC and the prediction is compared to the true yields from simulation. Figure 4.15 show the comparison of the prediction (applying the fake rate parameterization to single electron MC events) and true yields; the agreement is found to be within 20%.

Data/MC fake rate corrections

The data/MC corrections for the fake rate are computed using a T&P method on Drell-Yan events. Z bosons are reconstructed using a tag object and a probe object. The tag object definition is one tight electron with $p_T > 40$ GeV. The probe can either be one tight electron or one photon with $p_T > 100$ GeV. Event selections otherwise includes, $N_{jets} \geq 2$, $p_T^{miss} < 100$ GeV, zero isolated tracks (not including the tag/probe objects), and $\Delta R(\text{tag}, \text{probe}) > 0.2$. In the case where the probe satisfies the tag criteria, the tag is chosen randomly and the event is counted twice.

Once the photon and electron candidates are formed, the $m_{\ell\ell}$ distribution is fit using a Breit-Wigner convoluted with a Gaussian to model the Z boson peak and a

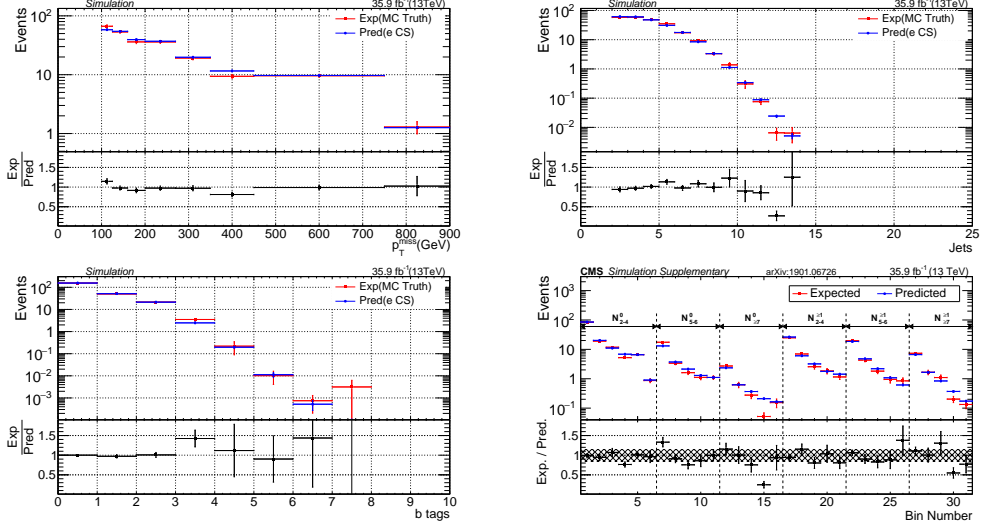


FIGURE 4.15: Comparison of fake rate prediction using fake rate parameterization and true MC yields using $W/t\bar{t} + (\gamma)$ simulations versus p_T^{miss} (top left), N_{jets} (top right), $N_{\text{b-jets}}$ (bottom left) and search bins (bottom right). The hashed region in the lower panel of bottom right plot shows the total systematic uncertainty.

polynomial to model the combinatorial background. The fit is performed on both data and MC in regions of Q_{mult} , which is the variable for which the discrepancies between data and MC are found to be the largest. Table 4.4 shows the fitted fake rate in data and MC, and the corresponding correction factor in each of the Q_{mult} bins. Figure 4.16 shows the fit results for each of the fake rate measurements.

TABLE 4.4: Fake rate as measured by T&P procedure on Drell-Yan events in data and MC.

Q_{mult}	MC fake rate	data fake rate	scale factor
0-1	0.014 ± 0.002	0.016 ± 0.003	1.17 ± 0.27
≥ 2	0.015 ± 0.001	0.018 ± 0.002	1.21 ± 0.16

Fake rate prediction

Using the results described above, the prediction for the fake photon background is shown in Table A.4 (for high $\Delta\phi$) and Table A.5 (for low $\Delta\phi$).

4.6.3 Invisible Z estimation

The invisible Z background is estimated using a $Z(\ell\ell)$ plus γ control region. The method relies on the fact that for $\gamma Z(vv)$ events, the p_T^{miss} is roughly equal to the transverse momentum of the Z boson. There is also a small contribution from limited resolution of other objects in the event – primarily jets; this effect of finite resolution means that $p_{T,Z(\ell\ell)}$ cannot be used directly as a proxy for p_T^{miss} .

The $Z(\ell\ell)$ plus γ events are required to have one high- p_T photon and two oppositely charged, same flavor leptons (e, μ) whose invariant mass is consistent with the Z mass, $80 < m_{\ell\ell} < 100$ GeV. For the purposes of computing event level kinematic variables, the effect of leptons is removed. For H_T^γ , N_{jets} , $N_{\text{b-jets}}$, and $\Delta\phi$ jets which are matched, $\Delta R < 0.3$, to the charged leptons are ignored. For p_T^{miss} the reconstructed

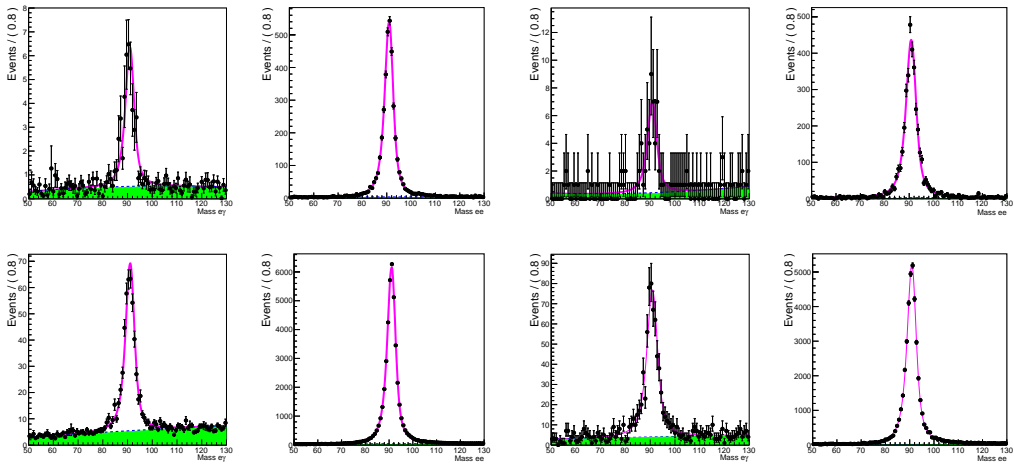


FIGURE 4.16: Tag & probe fits of the fake rate in 0-1 Q_{mult} bins (top row) and $\geq 2 Q_{mult}$ bins (bottom row). The first and second columns are the the photon region and electron region fits in MC, respectively. The third and fourth columns are the photon region and electron region fits in data, respectively.

transverse momentum of the Z candidate is added to the p_T^{miss} vector. This cleaning procedure allow for finite jet resolution to smear the $p_{T,Z(\ell\ell)}$ and provide a consistent way of modeling the kinematics of neutrino decays. The kinematic selections are then the same as the signal region, but using these “cleaned” variables.

$Z(\ell\ell)$ plus γ events have one primary difference with respect to $Z(\nu\nu) + \gamma$ events; the former can result from the photon being radiated by charged leptons from the Z boson decay. This effect is small for our phase space, $p_{T,Z(\ell\ell)} p_T^{miss} > 100$ GeV and $p_T^\gamma > 100$ GeV. However, these events will typically produce a photon which is roughly colinear with one of the charged leptons in the event. We require that the angle between any electron or muon and the photon be $\Delta R(e/\mu, \gamma) > 0.2$. We also require invariant mass of di-lepton pair to be in the range 80 – 100 GeV which further suppresses the photon radiation from lepton.

The triggers for the γ -DY control region are the same as the signal region triggers.

Because of the low statistics for $Z(\ell\ell)+\gamma$ events, the p_T^{miss} shape will be taken directly from MC. The overall event yield will be measured by scaling the $Z(\nu\nu) + \gamma$ event yield by a MC transfer factor, TF, $(N_{\nu\nu+\gamma}^{\text{MC}} / N_{ll+\gamma}^{\text{MC}})$ that will account for the relative branching ratio, $\mathcal{B}(\nu\nu)/\mathcal{B}(\ell\ell)$, and reconstruction efficiencies of the charged leptons. The kinematics of the $Z(\nu\nu)+\gamma$ and $Z(\ell\ell)+\gamma$ are very identical and they are shown in figure 4.17 for some of the variables. Because of the nonavailability of the $Z(\ell\ell)+\gamma$ MC samples with $p_T^\gamma < 130$ GeV, these transfer factors are derived from high p_T^γ region.

The prediction is given by,

$$N_{\nu\nu+\gamma}^{\text{data}}(\text{SR Bin}) = N_{ll+\gamma}^{\text{data}} \cdot \beta_{ll+\gamma} \cdot \left(\frac{N_{\nu\nu+\gamma}^{\text{MC}}}{N_{ll+\gamma}^{\text{MC}}} \right)^{p_T^\gamma > 190} \cdot \frac{N_{\nu\nu+\gamma}^{\text{MC}}(\text{SR Bin})}{N_{\nu\nu+\gamma}^{\text{MC}}} \quad (4.6)$$

where $\beta_{ll+\gamma}$ represents the purity of the $Z(\ell\ell)+\gamma$ control region and the last term $N_{\nu\nu+\gamma}^{\text{MC}}(\text{SR Bin})/N_{\nu\nu+\gamma}^{\text{MC}}$ represents a MC template that determines the $p_T^{miss}, N_{\text{jets}}$ shape of the prediction; the template is computed independently for each of the signal regions. $N_{ll+\gamma}^{\text{data}}$ represents the observed number of events in data while $N_{ll+\gamma}^{\text{MC}}$ represents the expected number of from MC; both are computed inclusively in search

bins. As mentioned before, we derive TF in $p_T^\gamma > 190$ GeV region. There are two reasons why the same TF is applicable even at low photon p_T^γ regions:

- The number of events that lie in the region $100 < p_T^\gamma < 190$ GeV is a small fraction of the total events (about 15%).
- TF is not dependent on photon p_T (top left plot in Figure 4.17).

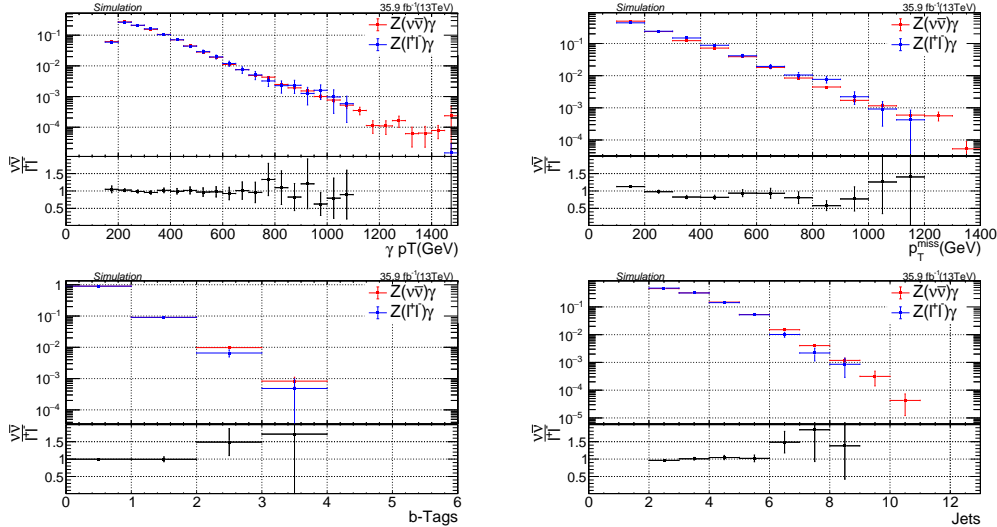


FIGURE 4.17: Comparison of $Z(\ell\ell)\gamma$ with $Z(vv)\gamma$ as function of p_T^γ (top left), p_T^{miss} (top right), $N_{\text{b-jets}}$ (bottom left) and N_{jets} (bottom right) for $p_T^\gamma > 190$ GeV

The purity of the $Z(\ell\ell)+\gamma$ control region is determined from a fit to the invariant mass, $m_{\ell\ell}$, distribution. This isolates contamination from $\gamma t\bar{t}$ events, which are expected to have a roughly flat distribution. The purity is checked in three different ways, using MC to predict the number of $t\bar{t}\gamma$ events, using a fit to the $m_{\ell\ell}$ distribution, and using the opposite-sign, different-flavor control sample ($e\mu\gamma$). All three predictions give consistent results when calculated within the baseline phase-space, which are reported in Table 4.5. The uncertainties associated with our prediction of the $Z(\ell\ell)\gamma$ purity is also propagated to the final $Z\gamma$ prediction.

TABLE 4.5: Purity in the $Z\gamma$ control region.

$N_{\text{b-jets}}$	Method		
	MC	$m_{\ell\ell}$ fits	$e\mu$ CR
≥ 0	0.978 ± 0.009	0.97	0.97 ± 0.03

Because of the very low statistics in low $\Delta\phi$ region in data, we make use of scale factors that are derived using high $\Delta\phi$ events to predict events in the low $\Delta\phi$ region. Scale factor is given by equation 4.7 and it is found to be 1.11 ± 0.21 .

$$SF = \left(\frac{N_{\ell\ell+\gamma}^{\text{data}} \cdot \beta_{\ell\ell+\gamma}}{N_{vv+\gamma}^{\text{MC}}} \right)^{p_T^\gamma > 190, \text{high } \Delta\phi} \quad (4.7)$$

Prediction in low $\Delta\phi$ region is,

$$N_{\nu\nu+\gamma}^{data}(SR\ Bin) = SF \cdot N_{\nu\nu+\gamma}^{\text{MC}}(SR\ Bin) \quad (4.8)$$

To account for systematic uncertainties associated with the MC modeling of the p_T^{miss} shape, we apply the full electro-weak corrections obtained from theory calculations [102] as a function of p_T^{miss} . These uncertainties are listed in table 4.6. they can be as high as 40% in highest p_T^{miss} bin. These uncertainties are treated as correlated across p_T^{miss} bins for the limit setting procedure. Uncertainties from b-tag SF are also considered and they are 2% in 0b-tag bins and 6% in ≥ 1 b-tag bins. The b-tag SF uncertainty is treated as anti-correlated in 0 and ≥ 1 b-tag bins. Final predictions for $Z(\nu\nu) + \gamma$ are listed in Table A.6 for high $\Delta\phi$ and in Table A.7 for low $\Delta\phi$ regions.

TABLE 4.6: Electroweak corrections as a function of p_T^{miss} .

p_T^{miss} (GeV)	% EW Correction
100-200	8
200-270	18
270-350	20
350-450	25
450-750	35
≥ 750	40

4.6.4 $\gamma + \text{jets}$ and QCD multijet estimation

Along with the presence of a well identified high p_T photon in the event, the $\gamma + \text{jets}$ production contributes to the background in search regions if one of the jets in an event is mis-measured resulting in fake p_T^{miss} or it contains a jet originating from b-quarks with a semileptonic decay of B mesons. Fluctuations in hadronization of jets can also result in an energetic π^0 misidentified as a photon which along with fake p_T^{miss} originating from other jets in the event can result in a QCD multijet production contribution to the search regions. Fake p_T^{miss} arising from mis-measurements of jets or semileptonic b-jets is usually aligned with the jet itself. Hence, a most of this background is rejected by angular cuts summarized in section 4.4 i.e. $\Delta\phi(\vec{p}_T^{\text{miss}}, \vec{p}_T^{\text{jet}}) > 0.3$ for first two leading jets. The main contribution to background is due to the $\gamma + \text{jets}$ processes and QCD multijet contribution is very small. In the method described in this section, the total background due to fake p_T^{miss} is estimated without further separating the QCD multijet and $\gamma + \text{jets}$ processes. The control sample to estimate the $\gamma + \text{jets}$ and QCD multijet background is derived inverting the $\Delta\phi(p_T^{\text{miss}}, \text{jet1})$ and $\Delta\phi(p_T^{\text{miss}}, \text{jet2})$ criteria ($\min(\Delta\phi_1, \Delta\phi_2) < 0.3$) while keeping all the search selections intact except that $100 < p_T^{\text{miss}} < 200$ GeV sideband is also used. Since fake p_T^{miss} and mis-measured jets are mostly aligned in transverse direction, the inverted $\Delta\phi$ region provides a high statistics region rich in multijet background. Figure 4.18 shows the $\min(\Delta\phi_1, \Delta\phi_2)$ distribution in MC with $p_T^{\text{miss}} > 200$ GeV.

The method briefly summarized as follows:

- Using the low p_T^{miss} sideband, ratio $R(N_{\text{jets}}, N_{\text{b-jets}}) = \text{high-}\Delta\phi/\text{low-}\Delta\phi$ is determined. This ratio is determined from data sideband. Contribution from electroweak background (lost lepton + τ_{had} , e faking photon and invisible Z) is subtracted from event yields before measuring the ratio. The $R(N_{\text{jets}}, N_{\text{b-jets}})$ means that the ratio is binned in the bins of jet multiplicity and b-jet multiplicity.

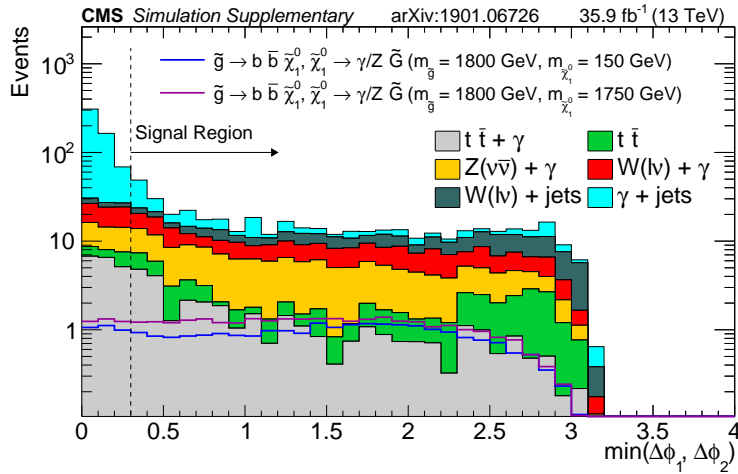


FIGURE 4.18: Distribution of $\min(\Delta\phi_1, \Delta\phi_2)$ in MC after applying all signal region selections except angular cuts. The region $\min(\Delta\phi_1, \Delta\phi_2) < 0.3$ serves as a $\gamma + \text{jets}$ enriched sample and $\min(\Delta\phi_1, \Delta\phi_2) > 0.3$ is the signal region. In this plot, $p_T^{\text{miss}} > 200$ GeV selection is applied. The histograms shown as lines represent two signal models which indicate that there is negligible signal contamination.

- The number of events obtained in low- $\Delta\phi$ region in $p_T^{\text{miss}} > 200$ GeV region, after subtracting the electroweak backgrounds, is multiplied with ratio to obtained number of events in the search regions.
- Since $\Delta\phi$ and p_T^{miss} are not completely independent, the method is corrected for dependence on p_T^{miss} using the MC, using an additional correction factor, $\kappa(N_{\text{jets}}, N_{\text{b-jets}})$, where the quantities in bracket shows the binning variables. So in this sense, it is a ABCD method modified to correct for $\Delta\phi$ and p_T^{miss} dependencies using the κ factor.
- The factor κ is validated in data using zero photon events using jet with highest neutral electromagnetic fraction as a proxy to photon.

The boundaries for high- $\Delta\phi$ and low- $\Delta\phi$, and high p_T^{miss} and low p_T^{miss} used as ABCD regions are shown in Figure 4.19 (left).

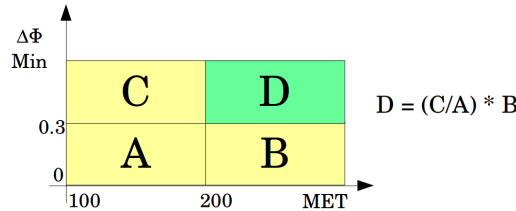


FIGURE 4.19: Definitions of various regions used in ABCD methods. Region D is signal region where background is to be estimated or validation region for zero photon sample.

The ratio of high- $\Delta\phi$ to low- $\Delta\phi$ has a strong dependence as a function of p_T^{miss} . This dependence is accounted for by an additional correction factor using ratio, R, in low p_T^{miss} and high p_T^{miss} regions in MC. That is a factor κ defined as $\kappa(N_{\text{jets}}, N_{\text{b-jets}}) = R(N_{\text{jets}}, N_{\text{b-jets}}) (\text{high } p_T^{\text{miss}}) / R(N_{\text{jets}}, N_{\text{b-jets}}) (\text{low } p_T^{\text{miss}})$. Please note that the ratio R and double ratio, κ are binned in the bins of N_{jets} and $N_{\text{b-jets}}$.

Using these values of R and κ , the performance of the method is validated using MC simulation. If the numbers R and κ were derived using exact search region definitions, the closure would be one. Hence this validation mainly tests performance parameterization of these factors. The results of this closure tests are shown in Figure 4.20 as a function of search bins used for this analysis. The number of $\gamma + \text{jets}$ and QCD multijet background events estimated using the methods (blue) closely reproduces those expected in search regions (cyan). The first bin in each $N_{\text{jets}}-N_{\text{b-jets}}$ block corresponds to $100 < p_T^{\text{miss}} < 200$ GeV control regions, where expected and predicted backgrounds exactly match by definition.

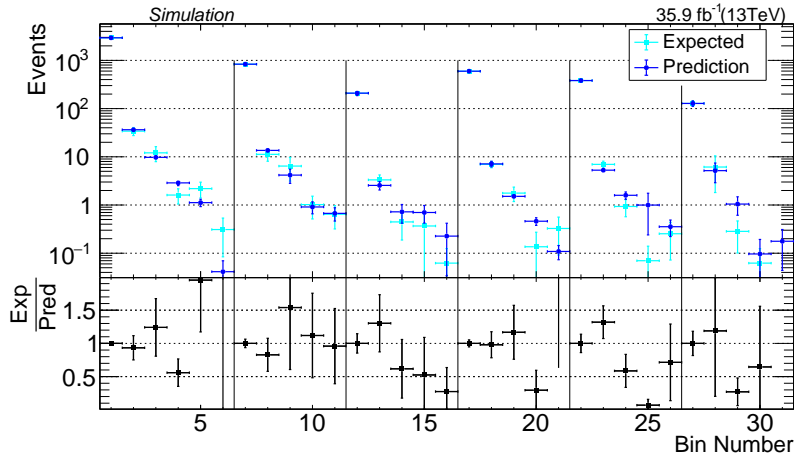


FIGURE 4.20: Comparison of $\gamma + \text{jets}$ and QCD multijet background estimated using low- $\Delta\phi$ control regions taken from MC (blue) to that expected in search regions (cyan).

TABLE 4.7: Double ratio(κ^{MC}) computed in the one γ regions and ratio of high- $\Delta\phi$ to low- $\Delta\phi$ (R^{data}) obtained from data using $100 < p_T^{\text{miss}} < 200$ GeV region with electroweak contribution subtracted.

	$N_{\text{b-jets}}$	N_{jets}	K^{MC}	R^{data}
0	2 - 4	0.29 \pm 0.04	0.80 \pm 0.02	
	5 - 6	0.47 \pm 0.11	0.94 \pm 0.05	
	≥ 7	0.40 \pm 0.11	1.04 \pm 0.17	
≥ 1	2 - 4	0.24 \pm 0.05	0.65 \pm 0.03	
	5 - 6	0.34 \pm 0.07	0.91 \pm 0.09	
	≥ 7	0.47 \pm 0.34	1.29 \pm 0.26	

Since the double ratio $\kappa(N_{\text{jets}}, N_{\text{b-jets}})$ used for correcting R in low and high p_T^{miss} regions is obtained from MC, and makes an important component of this method, it is validated using data. To define the data control sample, photon selection is inverted and events with a well identified photon are vetoed. In these zero photon events, the jet with the highest electromagnetic fraction is used as a proxy to the photon, and all baseline selection criteria are applied to the event. The jet used as proxy-photon is removed from the list of jets to avoid any double counting of the objects. With this zero photon event sample, double ratio, $\kappa(N_{\text{jets}}, N_{\text{b-jets}})$, is calculated exactly as in MC events.

The zero photon control sample is obtained from the data collected using a combination of inclusive H_T and single jet triggers as explained in 4.3. The electroweak

contribution to this sample is subtracted using event yields from the MC simulation samples. The MC event yields are corrected for the trigger efficiencies. Since these triggers achieve efficiency plateau only for $H_T > 1$ TeV, the $H_T > 1$ TeV region is used for validating the double ratio. The closure of this validation method in MC is shown in Figure 4.21.

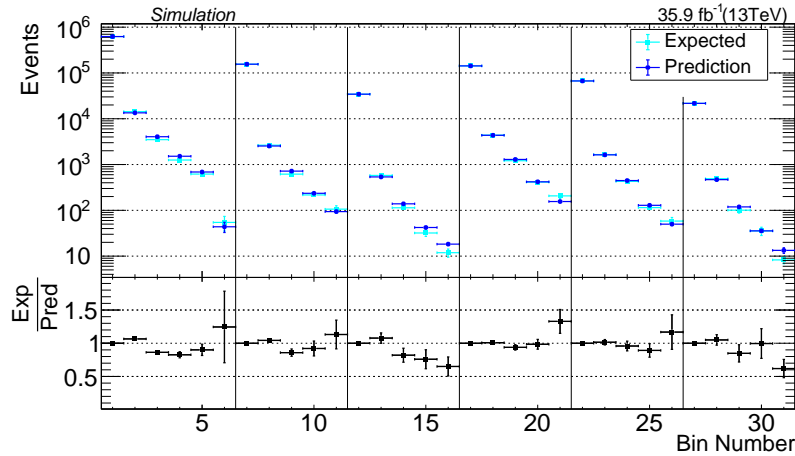


FIGURE 4.21: In zero photon validation region in MC, comparison of $\gamma + \text{jets}$ and QCD multijet background estimated using low- $\Delta\phi$ control regions taken from MC (blue) to that expected in search regions (cyan).

The values of double ratio, $\kappa(N_{\text{jets}}, N_{\text{b-jets}})$ obtained from zero photon validation region in data and MC are compared in Figure 4.22.

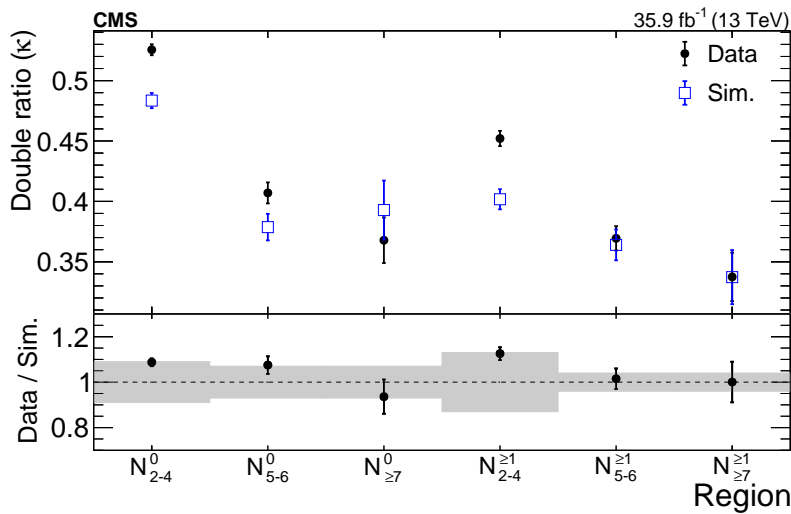


FIGURE 4.22: The double ratio κ in each $N_{\text{jets}}-N_{\text{b-jets}}$ region for zero-photon events. The filled black circles are the observed κ values after subtracting the electroweak contamination based on simulation. The open blue squares are the κ values computed directly from simulation. The ratio is shown in the bottom panel, where the shaded region corresponds to the systematic uncertainty in the $\gamma + \text{jets}$ prediction. In the label N_j^b , j refers to the number of jets and b refers to the number of b-tagged jets.

The uncertainties on predicted $\gamma + \text{jets}$ and QCD multijet background is dominated by statistical size of event sample in low- $\Delta\phi$ control region with $p_T^{\text{miss}} > 200$ GeV i.e. the region B, and ranges from 6-100%. These components of systematic uncertainties are taken uncorrelated across all bins. An additional contribution to this control region is due to uncertainties on predicted electroweak backgrounds which is subtracted from region B. This can range between 10-100%. Since $R(N_{\text{jets}}, N_{\text{b-jets}}) = \text{high-}\Delta\phi/\text{low-}\Delta\phi$ is defined in the bins of N_{jets} and $N_{\text{b-jets}}$ from low p_T^{miss} sideband region in single photon side band, statistical uncertainties on R are taken to be correlated for all bins with same N_{jets} and $N_{\text{b-jets}}$. The uncertainties on double ratio have two components: (a) difference between $K_{0\gamma}$ in data and MC, and (b) statistical uncertainty on $K_{0\gamma}^{\text{MC}}$. These two contributions are added in quadrature to assign the systematic uncertainties which are also taken fully correlated for all bins with same N_{jets} and $N_{\text{b-jets}}$. The final predictions of $\gamma + \text{jets}$ and QCD multijet processes is shown in A.8.

4.7 Systematic uncertainty for signal models

We consider a variety of experimental and theoretical systematic uncertainties on the signal rates. They are:

- **Luminosity:** A flat uncertainty of 2.5% is used.
- **Isolated track veto:** A flat uncertainty of 2% is assigned to the T5ttttZG, T5bbbbZG, T5qqqqHG and T6ttZG signal samples to account for any data/MC differences.
- **PF Jet ID:** Some of the PF Jet ID criteria, defined in Section 4.4, are not well-modeled in the fast simulation. Therefore, the jet ID criteria are not applied to the fast simulation samples. The efficiency of the event cleaning cut on the signal samples is expected to be $>99\%$ from the full simulation, so corrections are not needed. The uncertainty in this correction is taken to be a flat 1% uncertainty.
- **b-tag efficiency:** The b-tagging and mistagging scale factors are functions of the jet p_T and η . The scale factors are varied by their uncertainties and these variations are propagated as migrations between the different signal bins, with no effect on the overall signal efficiency. The b-tagging, charm-mistagging, and light flavor-mistagging scale factors are varied independently.
- **b-tag FastSim corrections:** The b-tagging and mistagging performance in the fast simulation must be corrected to match the full simulation. Separate correction factors are derived for b-jets, c-jets, and light flavor jets, as functions of the jet p_T and η . As with the scale factors above, the correction factors for each type of jet are varied independently by their uncertainties and these variations are propagated as migrations between the different signal bins.
- **Jet Energy Corrections:** The jet energy corrections (JECs) are varied using the p_T - and η -dependent jet energy scale uncertainties, with a separate set of corrections for the fast simulation samples. These variations are propagated into the various jet-dependent variables, including: N_{jets} , $N_{\text{b-jets}}$, p_T^{miss} , $\Delta\phi(\text{jet}, p_T^{\text{miss}})$ and H_T^γ . The effect is 5% or less.

- **Jet Energy Resolution:** Simulated jet momenta are smeared to match that in data, and the smearing factors are varied according to uncertainties on the jet energy resolution measurements. These variations are propagated into the various jet-dependent variables, including N_{jets} , $N_{\text{b-jets}}$, p_T^{miss} , $\Delta\phi(\text{jet}, p_T^{\text{miss}})$ and H_T^γ . The overall effect is 2%.
- **p_T^{miss} Uncertainty :** Mainly special treatment of p_T^{miss} modeling in FastSim, and is expected to be important only in compressed regions. The signal yields are obtained using GenMET, summing all visible generator-level particles, and PFMET and average of the GenMET and PFMET is taken as central value. A flat uncertainty equal to one-half the difference between the GenMET and PFMET, fully correlated among p_T^{miss} bins is used for limit settings. This procedure results in less than a few percent uncertainty in non-compressed and $< 10\%$ uncertainties in highly compressed regions.
- **ISR:** An ISR correction is derived from t̄events, with a selection requiring two leptons (electrons or muons) and two b-tagged jets, implying that any other jets in the event arise from ISR. The correction factors are 1.000, 0.920, 0.821, 0.715, 0.662, 0.561, 0.511 for $N_{\text{jets}}\text{-ISR} = 0, 1, 2, 3, 4, 5, 6+$. For signal samples, number of ISR jets is the number of jets which are not originating from decay of gluino or vector boson or Higgs or top. The corrections are applied to the simulated signal samples with an additional normalization factor, typically ~ 1.15 (depending on the signal model), to ensure the overall cross section of the sample remains constant. The systematic uncertainty in these corrections is chosen to be half of the deviation from unity for each correction factor. The effect on the yield ranges from 4 – 30%, with the largest effect for compressed signal models. This is the most dominant uncertainty for the signal models which populate high N_{jets} bins.

Following theoretical uncertainties are evaluated for each signal model point or explained otherwise.

- **Scales:** The uncertainty is calculated using the envelope of the weights from varying the renormalization and factorization scales, μ_R and μ_F , by a factor of 2 [103, 104]. The effect on the yield is 2%.
- **PDFs:** The LHC4PDF prescription for the uncertainty on the total cross section is included as ± 1 sigma bands in the results plots. No additional uncertainty is considered for the uncertainty in the acceptance due to PDFs.

Table 4.8 summarizes the various uncertainties, the range of their impact on signal yields and modeling of the correlations.

Additionally, the effect of potential signal contamination in the $e + \gamma$ and $\mu + \gamma$ control regions is considered. If some events observed in the control regions are in fact due to a SUSY signal, the corresponding background prediction in the signal region will be too high. This effect is dealt with in the analysis by a corresponding reduction in the effective efficiency for the signal point. For the T5tttZG signal, the size of this reduction of effective signal efficiency is about 10% coming from $\mu + \gamma$ control region and 5% coming from $e + \gamma$ control region. For $e + \gamma$, effect of signal contamination is small as compared to $\mu + \gamma$, since transfer factor for lost electron is smaller than lost $\mu + \tau_{\text{had}}$ transfer factor. In the case of T6ttZG model, signal contamination is about 5% for $\mu + \gamma$ and 2.5% for $e + \gamma$. For other SMS that are considered in the analysis signal contamination is negligible.

TABLE 4.8: Systematic uncertainties for signal samples

Type of uncertainty	Magnitude	Correlation modeling
MC stats	1 – 70%	
JEC, JER	5%, 2%	Uncorr. across all bins
Iso-track veto	2%	
PF jet ID	1%	
b-tag SF	5% in high stat bins	Corr. across bins of same b-tag and anti-corr. across bins of different b-tag
ISR re-weighting μ_R and μ_F scales	4 – 30% 2%	Corr. across same N_{jets} bins
GenMET vs PFMET	< 10%	Corr. across p_T^{miss} bins
Trigger efficiency	2%	Corr. across all bins

Chapter 5

Results and summary

5.1 Results & statistical interpretations

The background predictions obtained in Section 4.6 and the observed data are used for interpretation in the context of SMS models shown in Figure 4.1. Each analysis bin is represented as a individual counting experiment with one signal process and five background processes. Each process is assumed to be a Poisson distribution with some number of prior distribution representing the uncertainty on the corresponding process's rate parameter. The exact details of how these uncertainties are modeled depends on the details of each of the background estimation methods that were used.

In general, each background estimation is a scaling of a control region, $N_{\text{bkg}}^{\text{pred}} = N_{\text{CR}}^{\text{pred}} \beta$, where β is the transfer factor, $N_{\text{CR}}^{\text{pred}}$ is the expected yield in the control region of the corresponding process, and $N_{\text{bkg}}^{\text{pred}}$ is the prediction provided as the expected mean of the corresponding process's Poisson distribution for a given signal region. In general, $N_{\text{CR}}^{\text{pred}}$ is constrained by the observed yields in the control region, $N_{\text{CR}}^{\text{obs}}$ and there are five such constraints from each of the 5 control regions discussed in Section 4.6. For a simplified counting experiment with only one background process and one signal process, the likelihood for this type of background prediction would be,

$$\mathcal{L}(N_{\text{sig}}^{\text{pred}}, N_{\text{bkg}}^{\text{pred}} | N_{\text{SR}}^{\text{obs}}, N_{\text{CR}}^{\text{obs}}) \propto \left(N_{\text{bkg}}^{\text{pred}} + N_{\text{sig}}^{\text{pred}} \right)^{N_{\text{SR}}^{\text{obs}}} e^{-N_{\text{bkg}}^{\text{pred}}} \cdot \left(\frac{N_{\text{bkg}}^{\text{pred}}}{\beta} \right)^{N_{\text{CR}}^{\text{obs}}} e^{-N_{\text{bkg}}^{\text{pred}}/\beta} \quad (5.1)$$

This likelihood, is equivalent to a Poisson likelihood with a gamma distribution as the prior and can be used to constrain both the predicted background the signal strength in the signal region with the proper modeling of the $N_{\text{bkg}}^{\text{pred}}$ uncertainty due to limited statistics of the control region observed yield.

As such, we model the uncertainty on the prediction due to limited control region statistics as a gamma distribution. This procedure is followed, especially when the observed control region statistics are too small to justify a Gaussian approximation. While the observed control region events vary considerably, for the signal regions in extreme corners of our phase space the use of a Gamma prior distribution is critical for modeling uncertainties. For uniformity, we generally use it everywhere. The exception to this, as mentioned below, is the $e+\text{jets}$ control region, which is used for estimating the fake-photon background, where we use a Gaussian prior to model the effect of limited control region statistics. Note, the number of observed events in

these control regions is always larger than 17 events, for which the 1σ intervals of a Poisson distribution and Gaussian distribution still agree to within 10%.

The uncertainty on the transfer factors used to scale the observed event yields in the control regions are modeled with log-normal prior distributions. These priors account for uncertainties typically arising from limited MC statistics, systematic effects due to composition or limited knowledge of object reconstruction efficiencies, or PDF/scale uncertainties. Uncertainties from limited MC statistics are typically uncorrelated across each of the search regions. Other source of systematic uncertainty typically correlate expected yields from various signal regions. Details of the modeling of systematic uncertainties for each of the background estimations is given below.

For the lost-e and lost- $\mu + \tau_{\text{had}}$ predictions, the uncertainties on the prediction are modeled with a gamma distribution, with the shape parameter set to the observed number of events in the corresponding $\ell - \gamma$ control region and the scale parameter is set to be the average transfer factor, given in Table 4.3. There are also log-normal prior distributions used to model the uncertainties of the transfer factors, which account for the following sources:

- limited MC statistics; the corresponding nuisance parameters are fully uncorrelated.
- PDF and scale uncertainties; the corresponding nuisance parameters are fully correlated across signal regions and between lost-e and lost- $\mu + \tau_{\text{had}}$.
- jet energy scale uncertainties; the corresponding nuisance parameters are fully correlated across all signal regions.
- lepton scale factor uncertainties; the corresponding nuisance parameters are fully correlated across p_T^{miss} bins and fully uncorrelated across $N_{\text{b-jets}}, N_{\text{jets}}$ regions;
- uncertainties related to soft/collinear photon modeling; the corresponding nuisance parameters are fully correlated for lost-e and negligible for $\mu + \tau_{\text{had}}$ prediction.

For the fake-rate estimation of $W + \gamma$ and $t\bar{t} + \gamma$ events, the systematic uncertainties from the control region statistics are typically small. All of the uncertainties are modeled with log-normal prior distributions whose uncertainties correspond to:

- the statistical uncertainty from the $e \rightarrow \gamma$ control regions; the corresponding nuisance parameters are fully uncorrelated across all signal regions.
- fake rate scale factors; the corresponding nuisance parameters are fully correlated across all signal regions.
- uncertainties due to pileup and initial state radiation (ISR) modeling of simulations; the corresponding nuisance parameters are fully correlated across all signal regions.

For the $Z\gamma$ predictions, the statistical uncertainties from control region are modeled with a gamma prior distribution whose shape parameter is the observed events in the $Z(\ell\ell)\gamma$ control region and the scale parameter is the purity-corrected MC transfer factor, which in the nomenclature of Equation 4.6 is $\beta \cdot N_{\nu\nu+\gamma}^{\text{MC}} / N_{\ell\ell+\gamma}^{\text{MC}}$. Additional log-normal prior distributions are included to account for the following factors:

- the effect of limited MC statistics on $N_{X+\gamma}^{\text{MC}}$; the corresponding nuisance parameters are fully uncorrelated across all signal regions;
- uncertainties on the purity; the corresponding nuisance parameter fully correlates the effect across all signal regions.
- uncertainties due to b-tag scale factors; the corresponding nuisance parameters are fully correlated across p_T^{miss} and N_{jets} bins, anti-correlated across $N_{\text{b-jets}}$ regions.
- uncertainty due to missing higher order corrections; the corresponding nuisance parameters are fully correlated across p_T^{miss} bins, uncorrelated across $N_{\text{b-jets}}, N_{\text{jets}}$ regions.

For the multijet predictions, the systematic uncertainties due to limited control region statistics are modeled with a Gamma prior distribution whose shape parameter is the observed number of events in the low- $\Delta\phi$ control regions and the scale parameter is the product of the high-to-low ratio, $R_{\text{h/l}}$, the double ratio correction factors, κ , and the purity, β , obtained from data-driven predictions of the electroweak backgrounds in the low- $\Delta\phi$ control regions. Systematic uncertainties on the knowledge of this combined transfer factor are modeled with log-normal prior distributions and account for

- uncertainties on $R_{\text{h/l}}$ due to limited number of events in data sideband; the corresponding nuisance parameters are fully correlated across p_T^{miss} bins and fully uncorrelated across $N_{\text{b-jets}}, N_{\text{jets}}$ regions.
- uncertainties on κ based on validations with zero photon events; the corresponding nuisance parameters are fully correlated across p_T^{miss} bins and fully uncorrelated across $N_{\text{b-jets}}$ and N_{jets} regions.
- uncertainties on β due to all uncertainties as described above; the corresponding nuisance parameters are fully uncorrelated across all search regions.

All of the uncertainties associated with the signal yields, described in detail in Section 4.7, are modeled with log-normal prior distributions. Nuisance parameters associated with ISR modeling uncertainties are correlated across the various N_{jets} bins, but uncorrelated across $N_{\text{b-jets}}$ and p_T^{miss} regions. Nuisance parameters associated with p_T^{miss} modeling in simulation are correlated across the various p_T^{miss} bins and uncorrelated across $N_{\text{b-jets}}$ and N_{jets} regions. Nuisance parameters associated with b-tagging scale factors are fully correlated across all p_T^{miss} and N_{jets} , but anti-correlated across the $N_{\text{b-jets}}$ regions. The nuisance parameters associated with the statistical uncertainties of our simulated samples are fully uncorrelated across all signal regions. A single nuisance parameter is associated with the luminosity uncertainty and fully correlates the effect across all signal regions.

Expected and observed limits are computed after adjusting the central values and uncertainties associated with all nuisance parameters to data by minimizing them with respect to the observed yields while fixing the signal strength to zero.

The predicted background and observed yields are shown in Table 5.1 and Fig. 5.1. The largest deviation is found in bin 2 ($2 \leq N_{\text{jets}} \leq 4$, $N_{\text{b-jets}} = 0$, and $270 < p_T^{\text{miss}} < 350$ GeV), where the background is predicted to be 91 events with 51 events observed. The local significance of this single bin was computed to be around 2 standard deviations below the SM expectation. This calculation does not account for the

look-elsewhere effect associated with the use of 25 exclusive signal regions, which is expected to reduce this significance. In general, a large deviation in a single bin is inconsistent with the expected distributions of events from the signal models considered here. The observations in all other bins are consistent with the SM expectations within one standard deviation.

TABLE 5.1: Predicted and observed event yields for each of the 25 exclusive signal regions.

N_{jets}	$N_{\text{b-jets}}$	$p_T^{\text{miss}} [\text{GeV}]$	Lost e	Lost $\mu + \tau_{\text{had}}$	Misid. γ	$Z(\nu\bar{\nu})\gamma$	$\gamma + \text{jets}$	Total	Data
2-4	0	200-270	10.5 ± 2.6	31.2 ± 6.0	22.3 ± 5.4	33.6 ± 8.3	60 ± 11	157 ± 16	151
2-4	0	270-350	5.8 ± 1.8	29.6 ± 5.9	11.9 ± 2.9	22.9 ± 6.0	20.5 ± 4.3	91 ± 10	51
2-4	0	350-450	1.68 ± 0.88	13.9 ± 3.9	6.6 ± 1.6	17.0 ± 5.2	4.1 ± 1.4	43.3 ± 6.8	50
2-4	0	450-750	1.98 ± 0.94	8.1 ± 3.1	6.7 ± 1.5	18.1 ± 7.1	2.5 ± 1.3	37.4 ± 8.0	33
2-4	0	>750	$0.00^{+0.69}_{-0.00}$	1.2 ± 1.2	0.79 ± 0.19	2.8 ± 1.2	$0.41^{+0.42}_{-0.41}$	5.2 ± 1.9	6
5-6	0	200-270	1.28 ± 0.61	5.1 ± 1.9	3.53 ± 0.75	3.09 ± 0.78	15.8 ± 4.8	28.8 ± 5.3	26
5-6	0	270-350	2.06 ± 0.80	3.2 ± 1.5	2.39 ± 0.56	1.98 ± 0.54	3.7 ± 1.8	13.3 ± 2.6	11
5-6	0	350-450	0.77 ± 0.46	$0.64^{+0.65}_{-0.64}$	1.26 ± 0.30	1.49 ± 0.47	1.23 ± 0.97	5.4 ± 1.4	8
5-6	0	>450	0.26 ± 0.26	1.9 ± 1.1	1.00 ± 0.24	1.65 ± 0.65	$0.07^{+0.52}_{-0.07}$	4.9 ± 1.4	7
≥ 7	0	200-270	$0.00^{+0.61}_{-0.00}$	$0.0^{+1.3}_{-0.0}$	0.72 ± 0.16	0.37 ± 0.11	1.8 ± 1.2	2.9 ± 1.9	3
≥ 7	0	270-350	$0.34^{+0.35}_{-0.34}$	1.5 ± 1.0	0.38 ± 0.10	0.24 ± 0.08	1.22 ± 0.94	3.6 ± 1.5	3
≥ 7	0	350-450	$0.34^{+0.35}_{-0.34}$	0.73 ± 0.73	0.17 ± 0.05	0.16 ± 0.07	$0.07^{+0.50}_{-0.07}$	1.46 ± 0.96	0
≥ 7	0	>450	$0.00^{+0.61}_{-0.00}$	$0.0^{+1.3}_{-0.0}$	0.20 ± 0.06	0.17 ± 0.08	$0.00^{+0.75}_{-0.00}$	$0.37^{+1.60}_{-0.37}$	0
2-4	≥ 1	200-270	3.4 ± 1.5	14.5 ± 4.2	7.1 ± 1.7	3.55 ± 0.89	11.3 ± 3.3	39.8 ± 5.9	50
2-4	≥ 1	270-350	2.9 ± 1.4	5.6 ± 2.5	3.79 ± 0.92	2.45 ± 0.65	5.7 ± 1.8	20.4 ± 3.6	20
2-4	≥ 1	350-450	$0.0^{+1.0}_{-0.0}$	1.1 ± 1.1	2.00 ± 0.45	1.81 ± 0.55	0.59 ± 0.44	5.5 ± 1.7	4
2-4	≥ 1	>450	2.3 ± 1.2	4.4 ± 2.3	1.62 ± 0.38	2.14 ± 0.84	0.95 ± 0.54	11.5 ± 2.8	8
5-6	≥ 1	200-270	3.5 ± 1.3	2.4 ± 1.4	5.5 ± 1.2	0.76 ± 0.20	7.7 ± 2.4	19.9 ± 3.3	21
5-6	≥ 1	270-350	1.06 ± 0.64	4.0 ± 1.8	2.98 ± 0.63	0.49 ± 0.14	2.1 ± 1.0	10.6 ± 2.3	15
5-6	≥ 1	350-450	0.71 ± 0.51	2.4 ± 1.4	1.38 ± 0.29	0.32 ± 0.11	$0.30^{+0.49}_{-0.30}$	5.1 ± 1.6	6
5-6	≥ 1	>450	$0.35^{+0.36}_{-0.35}$	$0.0^{+1.4}_{-0.0}$	0.67 ± 0.15	0.48 ± 0.20	$0.00^{+0.56}_{-0.00}$	$1.5^{+1.6}_{-1.5}$	2
≥ 7	≥ 1	200-270	0.72 ± 0.53	2.0 ± 1.2	1.68 ± 0.37	0.13 ± 0.04	5.9 ± 5.0	10.5 ± 5.1	12
≥ 7	≥ 1	270-350	$0.00^{+0.65}_{-0.00}$	1.33 ± 0.96	0.73 ± 0.16	0.10 ± 0.04	$0.0^{+1.1}_{-0.0}$	2.2 ± 1.6	1
≥ 7	≥ 1	350-450	0.72 ± 0.53	$0.0^{+1.2}_{-0.0}$	0.44 ± 0.10	0.07 ± 0.03	$0.0^{+0.50}_{-0.0}$	$1.2^{+1.7}_{-1.2}$	1
≥ 7	≥ 1	>450	$0.36^{+0.37}_{-0.36}$	$0.0^{+1.2}_{-0.0}$	0.23 ± 0.07	0.04 ± 0.02	$0.0^{+1.1}_{-0.0}$	$0.6^{+1.7}_{-0.6}$	1

The test statistic $q_\mu = -2 \ln \mathcal{L}_\mu / \mathcal{L}_{\max}$, where \mathcal{L}_{\max} is the maximum likelihood determined by allowing all parameters, including the signal strength, to float, and \mathcal{L}_μ is the profiled likelihood. Limits are determined using the asymptotic form of the test statistic [105] in conjunction with the CL_s criterion [106, 107]. Expected upper limits are derived by varying observed yields according to expectations from the background only hypothesis.

Using the statistical procedure described above, 95% confidence level (CL) upper limits are computed on the signal cross section for each simplified model and each mass hypothesis. Exclusion limits are defined by comparing observed upper limits to the predicted NLO+NLL signal cross section. The signal cross sections are also varied according to theoretical uncertainties to give a ± 1 standard deviation variation on the observed exclusion contour. The 95% CL cross section limits and exclusion contours for the four models considered, T5qqqqHG, T5bbbbZG, T5tttZG, and T6ttZG, are shown in Fig. 5.2.

Generally, the limits degrade at both high and low $m_{\tilde{\chi}_1^0}$. For $m_{\tilde{\chi}_1^0} \approx m_{\tilde{g}} (m_f)$, the quarks from the decay of gluinos (top squarks) have low p_T . Correspondingly, the H_T^γ , N_{jets} , and $N_{\text{b-jets}}$ distributions tend toward lower values, reducing the signal efficiency and causing signal events to populate regions with higher background yields. For small $m_{\tilde{\chi}_1^0}$, the quarks produced in the decay of gluinos or top squarks have high p_T but lower p_T^{miss} on average. For all models except T5qqqqHG, when the NLSP mass drops below the mass of the Z boson, the kinematics of the NLSP decay require the Z boson to be far off-shell. As the Z boson mass is forced to be lower, the LSP will carry a larger fraction of the momentum of the NLSP, producing larger p_T^{miss} . This causes a slight increase in the sensitivity when the NLSP mass is near the

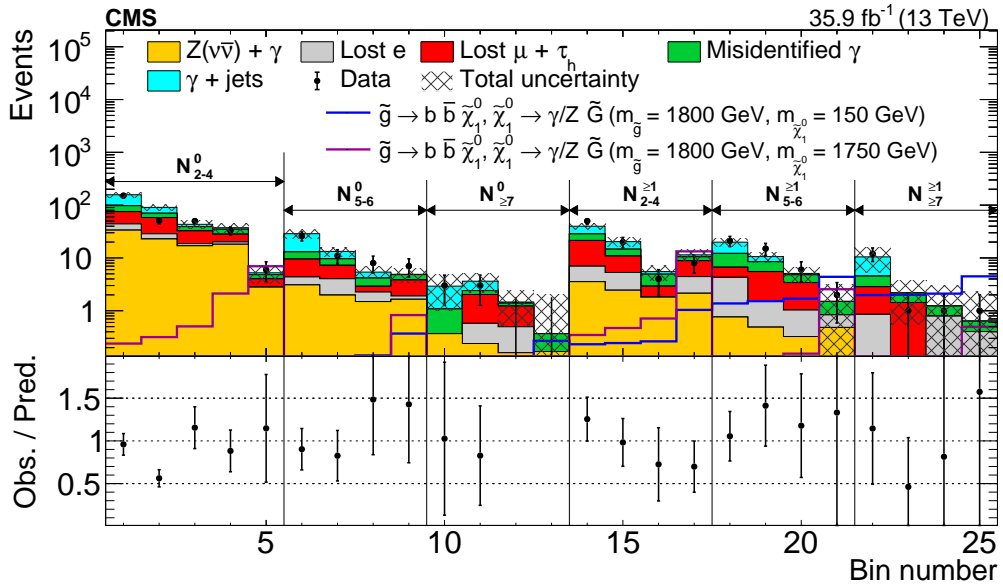


FIGURE 5.1: Observed numbers of events and predicted numbers of events from the various SM backgrounds in the 25 signal regions. The categories, denoted by vertical lines, are labeled as N_j^b , where j refers to the number of jets and b refers to the number of b-tagged jets. The numbered bins within each category are the various p_T^{miss} bins, as defined in Table 5.1. The lower panel shows the ratio of the observed events to the predicted SM background events. The error bars in the lower panel are the quadrature sum of the statistical uncertainty in the observed data and the systematic uncertainty in the predicted backgrounds before the adjustments based on a maximum likelihood fit to data assuming no signal strength.

Z boson mass. While a similar effect would happen for the T5qqqqHG model, the simulation used here does not probe the region of parameter space where the Higgs boson would be forced to have a mass far off-shell.

The features seen in exclusion curves can be understood using acceptance \times efficiency plots shown in figure B.4 in Appendix B.3.

For moderate $m_{\tilde{\chi}_1^0}$, gluino masses as large as 2090, 2120, and 1970 GeV are excluded for the T5qqqqHG, T5bbbbZG, and T5ttttZG models, respectively. Top squark masses as large as 1230 GeV are excluded for the T6ttZG model. For small $m_{\tilde{\chi}_1^0}$, gluino masses as large as 1920, 1950, and 1800 GeV are excluded for the T5qqqqHG, T5bbbbZG, and T5ttttZG models, respectively. Top squark masses as large as 1110 GeV are excluded for the T6ttZG model. There is close agreement between the observed and expected limits.

5.2 Summary

A search for gluino and top squark pair production is presented, based on a proton-proton collision dataset at a center-of-mass energy of 13 TeV recorded with the CMS detector in 2016. The data correspond to an integrated luminosity of 35.9fb^{-1} . Events are required to have at least one isolated photon with transverse momentum $p_T > 100$ GeV, two jets with $p_T > 30$ GeV and pseudorapidity $|\eta| < 2.4$, and missing transverse momentum $p_T^{\text{miss}} > 200$ GeV.

The data are categorized into 25 exclusive signal regions based on the number of jets, the number of b-tagged jets, and p_T^{miss} . Background yields from the standard

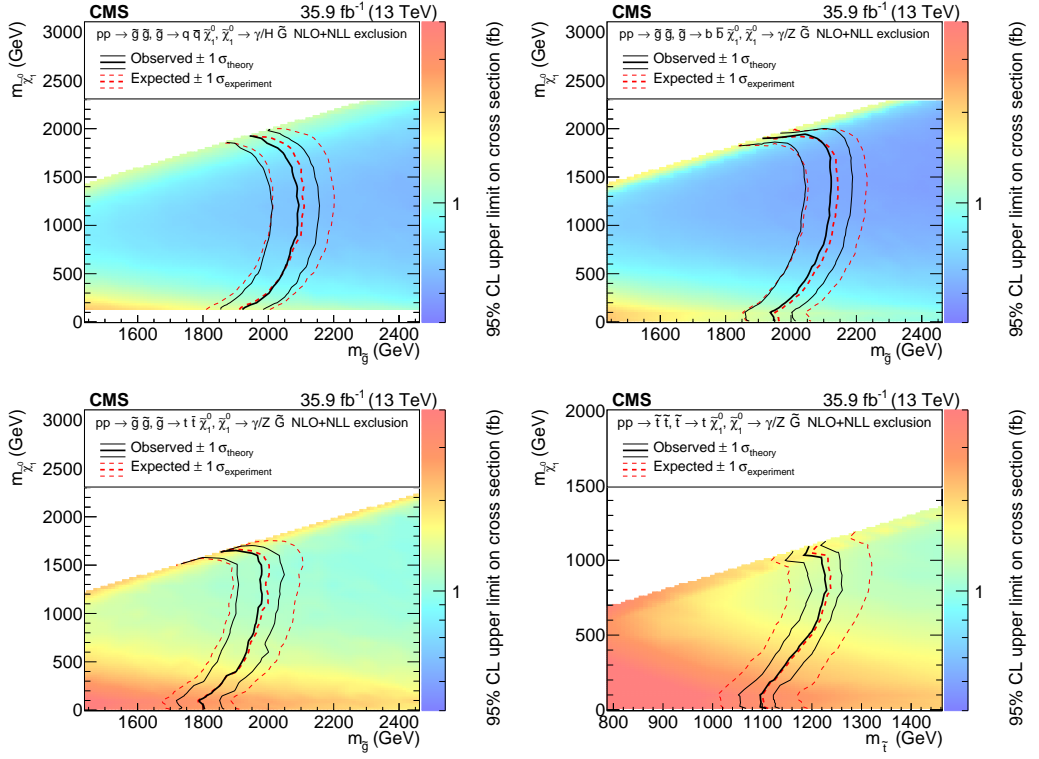


FIGURE 5.2: Observed and expected 95% CL upper limits for gluino or top squark pair production cross sections for the T5qqqqHG (upper left), T5bbbbZG (upper right), T5ttttZG (bottom left), and T6ttZG (bottom right) models. Black lines denote the observed exclusion limit and the uncertainty due to variations of the theoretical prediction of the gluino or top squark pair production cross section. The dashed lines correspond to the region containing 68% of the distribution of the expected exclusion limits under the background-only hypothesis.

model processes are predicted using simulation and data control regions. The observed event yields are found to be consistent with expectations from the standard model processes within the uncertainties.

Results are interpreted in the context of simplified models. Four such models are studied, three of which involve gluino pair production and one of which involves top squark pair production. All models assume a gauge-mediated supersymmetry (SUSY) breaking scenario, in which the lightest SUSY particle is a gravitino (\tilde{G}). We consider scenarios in which the gluino decays to a neutralino $\tilde{\chi}_1^0$ and a pair of light-flavor quarks (T5qqqqHG), bottom quarks (T5bbbbZG), or top quarks (T5ttttZG). In the T5qqqqHG model, the $\tilde{\chi}_1^0$ decays with equal probability either to a photon and a \tilde{G} or to a Higgs boson and a \tilde{G} . In the T5bbbbZG and T5ttttZG models, the $\tilde{\chi}_1^0$ decays with equal probability either to a photon and a \tilde{G} or to a Z boson and a \tilde{G} . In the top squark pair production model (T6ttZG), top squarks decay to a top quark and $\tilde{\chi}_1^0$, and the $\tilde{\chi}_1^0$ decays with equal probability either to a photon and a \tilde{G} or to a Z boson and a \tilde{G} .

Using the cross sections for SUSY pair production calculated at next-to-leading order plus next-to-leading logarithmic accuracy, we place 95% confidence level lower limits on the gluino mass as large as 2120 GeV, depending on the model and the $m_{\tilde{\chi}_1^0}$ value, and limits on the top squark mass as large as 1230 GeV, depending on the $m_{\tilde{\chi}_1^0}$ value. These results significantly improve upon those from previous searches for SUSY with photons.

5.3 Outlook

The main focus of this search was on GMSB scenarios with strong production of gluinos and stops. However, this is a generic search which searches for any beyond SM phenomena resulting in events with photon, p_T^{miss} , N_{jets} and N_{b-jets} final states. It is also possible to use the results of this search interpret them in terms of any other models. In this section we study the scope of this search by considering EW production of SUSY particles with SMS scenarios.

5.3.1 Electroweak models

Two kinds of electroweak (EWK) SMS scenarios, TChiWG and TChiNG, are studied and the expected limits are determined. In TChiWG (Figure 5.3 top), there is production of neutralinos ($\tilde{\chi}_1^0$) and charginos ($\tilde{\chi}_1^\pm$). The decay of $\tilde{\chi}_1^0$ gives $\tilde{G} + \gamma$ and the decay of $\tilde{\chi}_1^\pm$ gives $W^\pm + \tilde{G}$. In TChiNG (Figure 5.3 bottom) scenario, $\tilde{\chi}_1^\pm$ and $\tilde{\chi}_1^0$ are nearly mass degenerate, with $\tilde{\chi}_1^\pm$ being slightly heavier than $\tilde{\chi}_1^0$ and its decay gives rise to $\tilde{\chi}_1^0$ and soft particles which generally do not pass object level requirements. In this case, two production modes, $\tilde{\chi}_1^\pm\text{-}\tilde{\chi}_1^\pm$ (bottom left) and $\tilde{\chi}_1^\pm\text{-}\tilde{\chi}_1^0$ (bottom right) are considered. The branching fraction for the decay of $\tilde{\chi}_1^0$ is 50% $\tilde{G} + \gamma$, 25% $\tilde{G} + H$ and 25% $\tilde{G} + Z$. These are the same models as considered by the electrowikino search performed by CMS in Ref. [108]. The cross sections are calculated at NLO+NLL accuracy [109, 110, 111] and are computed in the limit of mass degenerate wino $\tilde{\chi}_2^0$ and $\tilde{\chi}_1^\pm$.

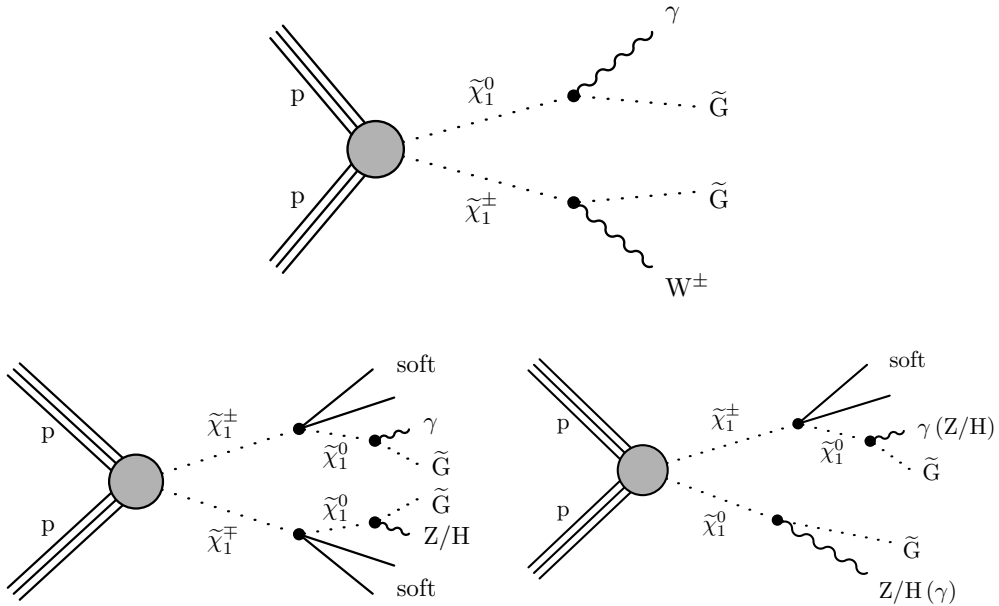


FIGURE 5.3: SMS diagrams for TChiWG (top) and TChiNG (bottom).

5.3.2 Sensitivity of the search

The results of the search described in this thesis are interpreted in terms of the above mentioned SMS scenarios and the expected limits on the cross section are compared with Ref. [108]. Figure 5.4 shows the expected upper limits on the cross section for TChiWG scenario (left) and TChiNG (right) scenario using this search.

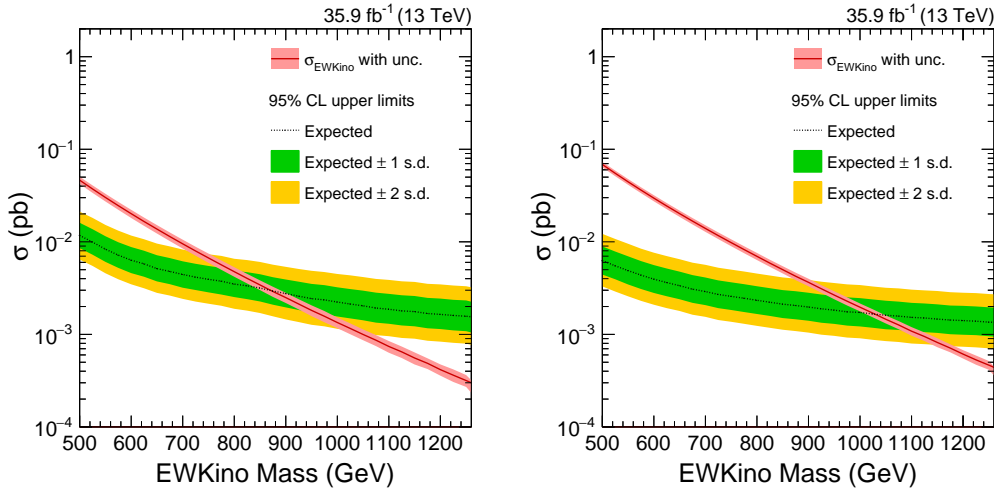


FIGURE 5.4: Expected upper limit on the cross section of TChiWG (left) and TChiNG (right) models.

EWKino masses below 870 GeV for TChiWG case and mass below 1030 GeV for TChiNG case can be excluded. The EW search of CMS [108] has expected EWKino mass exclusion of 920 GeV and 1070 GeV for TChiWG and TChiNG models respectively, which is about 40-50 GeV higher than this search.

It is also worth noting that the search described in this thesis does not consider all sources of systematic uncertainties in EWKino signal models. Only the statistical uncertainty in the MC samples and integrated luminosity uncertainty are considered. If all the sources of systematic uncertainty are considered, the limits in this search are going to degrade to some extent. However, these studies lead to an important conclusion that the search can target a wide range of models although strong production scenarios were the main focus.

One of the possible ways to improve this search and have a good sensitivity for EW models, is to loosen hadronic activity criteria mentioned in section 4.4. At present, the search requires minimum H_T^γ (sum p_T of jets and photon) of 500 GeV, which is very disadvantageous for EWKino production models. One possible way to reduce the background in low H_T^γ regions, is increasing p_T^γ or p_T^{miss} threshold.

During run 2 (year 2016-2018), CMS has collected more than 135 fb^{-1} of data and this is going to be an advantage for EW SUSY searches. A combination of several searches with photons is performed by CMS using 2016 data [112]. This combination uses photon + H_T^γ search [81], EW search [108], photon + lepton search [113] and diphoton search [114]. Since this search has very good sensitivity for strong SUSY production models, and if one performs further optimization the search for EW SUSY models, this search is going to play a significant role on the path to discovery or to constrain SUSY models.

Appendix A

Additional tables

A.1 Lost lepton + τ_{had} predictions

TABLE A.1: Observed events yields, average transfer factors (TFs) and predictions for lost-e and lost- μ + τ_{had} backgrounds in high $\Delta\phi$ regions.

Bin	Lost-e			Lost- μ		
	Obs.	Avg. TF	Pred.	Obs.	Avg. TF	Pred.
1	160	0.44 ± 0.07	70 ± 13	167	0.95 ± 0.07	159 ± 17
2	27	0.39 ± 0.06	10.5 ± 2.6	31	1.01 ± 0.07	31.2 ± 6.0
3	14	0.41 ± 0.07	5.8 ± 1.8	29	1.02 ± 0.07	29.6 ± 5.9
4	4	0.42 ± 0.07	1.68 ± 0.88	14	1.00 ± 0.07	13.9 ± 3.9
5	5	0.40 ± 0.06	1.98 ± 0.94	7	1.15 ± 0.08	8.1 ± 3.1
6	0	0.38 ± 0.06	$0.00^{+0.69}_{-0.00}$	1	1.23 ± 0.09	1.2 ± 1.2
7	23	0.28 ± 0.05	6.5 ± 1.8	31	0.66 ± 0.06	20.5 ± 4.1
8	5	0.26 ± 0.04	1.28 ± 0.61	8	0.64 ± 0.05	5.1 ± 1.9
9	8	0.26 ± 0.04	2.06 ± 0.80	5	0.64 ± 0.05	3.2 ± 1.5
10	3	0.26 ± 0.04	0.77 ± 0.46	1	0.64 ± 0.05	$0.64^{+0.65}_{-0.64}$
11	1	0.26 ± 0.04	0.26 ± 0.26	3	0.64 ± 0.05	1.9 ± 1.1
12	7	0.31 ± 0.08	2.2 ± 1.0	10	0.69 ± 0.10	6.9 ± 2.4
13	0	0.34 ± 0.09	$0.0^{+0.61}_{-0.0}$	0	0.73 ± 0.10	$0.0^{+1.3}_{-0.0}$
14	1	0.34 ± 0.09	$0.34^{+0.35}_{-0.34}$	2	0.73 ± 0.10	1.5 ± 1.0
15	1	0.34 ± 0.09	$0.34^{+0.35}_{-0.34}$	1	0.73 ± 0.10	0.73 ± 0.73
16	0	0.34 ± 0.09	$0.00^{+0.61}_{-0.00}$	0	0.73 ± 0.10	$0.0^{+1.3}_{-0.0}$
17	53	0.53 ± 0.09	28.2 ± 5.6	49	0.96 ± 0.10	47.2 ± 8.3
18	6	0.57 ± 0.09	3.4 ± 1.5	13	1.11 ± 0.11	14.5 ± 4.2
19	5	0.57 ± 0.09	2.9 ± 1.4	5	1.11 ± 0.11	5.6 ± 2.5
20	0	0.57 ± 0.09	$0.0^{+1.0}_{-0.0}$	1	1.11 ± 0.11	1.1 ± 1.1
21	4	0.57 ± 0.09	2.3 ± 1.2	4	1.11 ± 0.11	4.4 ± 2.3
22	41	0.39 ± 0.07	15.9 ± 3.7	51	0.73 ± 0.08	37.4 ± 6.5
23	10	0.35 ± 0.06	3.5 ± 1.3	3	0.79 ± 0.08	2.4 ± 1.4
24	3	0.35 ± 0.06	1.06 ± 0.64	5	0.79 ± 0.08	4.0 ± 1.8
25	2	0.35 ± 0.06	0.71 ± 0.51	3	0.79 ± 0.08	2.4 ± 1.4
26	1	0.35 ± 0.06	$0.35^{+0.36}_{-0.35}$	0	0.79 ± 0.08	$0.0^{+1.43}_{-0.0}$
27	16	0.43 ± 0.10	6.9 ± 2.3	16	0.65 ± 0.10	10.4 ± 3.0
28	2	0.36 ± 0.08	0.72 ± 0.53	3	0.66 ± 0.10	2.0 ± 1.2
29	0	0.36 ± 0.08	$0.00^{+0.65}_{-0.00}$	2	0.66 ± 0.10	1.33 ± 0.96
30	2	0.36 ± 0.08	0.72 ± 0.53	0	0.66 ± 0.10	$0.0^{+1.2}_{-0.0}$
31	1	0.36 ± 0.08	$0.36^{+0.37}_{-0.36}$	0	0.66 ± 0.10	$0.0^{+1.2}_{-0.0}$

TABLE A.2: Observed events yields, average transfer factors (TFs) and predictions for lost-e and lost- $\mu + \tau_{\text{had}}$ backgrounds in the low- $\Delta\Phi$ control region.

Bin	Lost-e			Lost- μ		
	Obs.	Avg. TF	Pred.	Obs.	Avg. TF	Pred.
1	77	0.20 ± 0.04	15.5 ± 3.9	62	0.64 ± 0.09	39.5 ± 7.7
2	22	0.16 ± 0.04	3.6 ± 1.1	25	0.57 ± 0.06	14.2 ± 3.3
3	11	0.18 ± 0.04	1.93 ± 0.74	7	0.63 ± 0.07	4.4 ± 1.7
4	6	0.16 ± 0.04	0.94 ± 0.44	5	0.66 ± 0.07	3.3 ± 1.5
5	7	0.17 ± 0.04	1.22 ± 0.55	11	0.59 ± 0.07	6.4 ± 2.1
6	0	0.17 ± 0.04	$0.00^{+0.31}_{-0.00}$	0	0.58 ± 0.07	$0.0^{+1.1}_{-0.0}$
7	10	0.19 ± 0.04	1.95 ± 0.76	13	0.54 ± 0.11	7.1 ± 2.4
8	1	0.17 ± 0.04	0.17 ± 0.17	1	0.54 ± 0.07	$0.54^{+0.55}_{-0.54}$
9	2	0.17 ± 0.04	0.33 ± 0.25	3	0.54 ± 0.07	1.63 ± 0.96
10	2	0.17 ± 0.04	0.33 ± 0.25	1	0.54 ± 0.07	$0.54^{+0.55}_{-0.54}$
11	0	0.17 ± 0.04	$0.00^{+0.30}_{-0.00}$	1	0.54 ± 0.07	$0.54^{+0.55}_{-0.54}$
12	1	0.26 ± 0.09	$0.26^{+0.28}_{-0.26}$	4	0.43 ± 0.12	1.72 ± 0.99
13	1	0.17 ± 0.06	$0.17^{+0.18}_{-0.17}$	2	0.59 ± 0.20	1.19 ± 0.93
14	0	0.17 ± 0.06	$0.00^{+0.31}_{-0.00}$	0	0.59 ± 0.20	$0.0^{+1.1}_{-0.0}$
15	1	0.17 ± 0.06	$0.17^{+0.18}_{-0.17}$	1	0.59 ± 0.20	$0.59^{+0.63}_{-0.59}$
16	0	0.17 ± 0.06	$0.00^{+0.31}_{-0.00}$	1	0.59 ± 0.20	$0.59^{+0.63}_{-0.59}$
17	26	0.39 ± 0.08	10.2 ± 2.9	22	0.86 ± 0.16	18.8 ± 5.3
18	4	0.27 ± 0.06	1.10 ± 0.59	4	0.68 ± 0.10	2.7 ± 1.4
19	1	0.27 ± 0.06	$0.27^{+0.28}_{-0.27}$	2	0.68 ± 0.10	1.37 ± 0.99
20	2	0.27 ± 0.06	0.55 ± 0.40	0	0.68 ± 0.10	$0.0^{+1.2}_{-0.0}$
21	0	0.27 ± 0.06	$0.00^{+0.49}_{-0.00}$	2	0.68 ± 0.10	1.37 ± 0.99
22	9	0.23 ± 0.06	2.03 ± 0.87	14	0.73 ± 0.13	10.2 ± 3.3
23	5	0.25 ± 0.06	1.26 ± 0.63	2	0.54 ± 0.08	1.07 ± 0.77
24	1	0.25 ± 0.06	$0.25^{+0.26}_{-0.25}$	1	0.54 ± 0.08	0.54 ± 0.54
25	1	0.25 ± 0.06	$0.25^{+0.26}_{-0.25}$	1	0.54 ± 0.08	0.54 ± 0.54
26	2	0.25 ± 0.06	0.50 ± 0.37	1	0.54 ± 0.08	0.54 ± 0.54
27	3	0.27 ± 0.10	0.81 ± 0.56	4	0.51 ± 0.12	2.0 ± 1.1
28	2	0.25 ± 0.07	0.50 ± 0.38	3	0.53 ± 0.10	1.59 ± 0.97
29	1	0.25 ± 0.07	$0.25^{+0.26}_{-0.25}$	0	0.53 ± 0.10	$0.00^{+0.95}_{-0.00}$
30	1	0.25 ± 0.07	$0.25^{+0.26}_{-0.25}$	0	0.53 ± 0.10	$0.00^{+0.95}_{-0.00}$
31	0	0.25 ± 0.07	$0.00^{+0.45}_{-0.00}$	0	0.53 ± 0.10	$0.00^{+0.95}_{-0.00}$

A.2 Electron fake photon

TABLE A.3: Fake rate parameterization derived from $W/t\bar{t}$ simulations.

p_T	Q_{mult}	fake rate
100 – 120	0 – 1	0.0261 ± 0.0029
	2 – 4	0.0125 ± 0.0009
	4 – 7	0.0080 ± 0.0006
	≥ 7	0.0052 ± 0.0006
120 – 140	0 – 1	0.0208 ± 0.0028
	2 – 4	0.0118 ± 0.0011
	4 – 7	0.0068 ± 0.0006
	≥ 7	0.0050 ± 0.0006
140 – 160	0 – 1	0.0263 ± 0.0036
	2 – 4	0.0094 ± 0.0010
	4 – 7	0.0079 ± 0.0007
	≥ 7	0.0028 ± 0.0004
160 – 180	0 – 1	0.0243 ± 0.0041
	2 – 4	0.0114 ± 0.0012
	4 – 7	0.0065 ± 0.0007
	≥ 7	0.0034 ± 0.0006
180 – 200	0 – 1	0.0194 ± 0.0038
	2 – 4	0.0070 ± 0.0011
	4 – 7	0.0070 ± 0.0009
	≥ 7	0.0040 ± 0.0008
200 – 230	0 – 1	0.0177 ± 0.0030
	2 – 4	0.0104 ± 0.0014
	4 – 7	0.0044 ± 0.0005
	≥ 7	0.0042 ± 0.0008
230 – 260	0 – 1	0.0235 ± 0.0052
	2 – 4	0.0062 ± 0.0011
	4 – 7	0.0051 ± 0.0008
	≥ 7	0.0034 ± 0.0007
260 – 300	0 – 1	0.0293 ± 0.0079
	2 – 4	0.0096 ± 0.0014
	4 – 7	0.0062 ± 0.0010
	≥ 7	0.0075 ± 0.0017
300 – 380	0 – 1	0.0224 ± 0.0052
	2 – 4	0.0091 ± 0.0014
	4 – 7	0.0073 ± 0.0009
	≥ 7	0.0035 ± 0.0006
380 – 500	0 – 1	0.0232 ± 0.0048
	2 – 4	0.0084 ± 0.0011
	4 – 7	0.0047 ± 0.0006
	≥ 7	0.0036 ± 0.0008
> 500	0 – 1	0.0210 ± 0.0041
	2 – 4	0.0102 ± 0.0015
	4 – 7	0.0076 ± 0.0010
	≥ 7	0.0047 ± 0.0014

TABLE A.4: Observed single electron yields, after accounting for lepton scale factors and relative trigger efficiencies factor, in each of the signal regions, the average scale factor due to MC-based fake rates and data/MC fake rate correction factors from T&P measurements, and the corresponding fake-rate predictions with all the uncertainties (statistical and systematic) taken into consideration.

Bin	Obs. e events	Avg. transfer factor	Prediction
1	11777	0.0089 ± 0.0022	105 ± 25
2	2426	0.0092 ± 0.0022	22.3 ± 5.4
3	1259	0.0094 ± 0.0023	11.9 ± 2.9
4	699	0.0094 ± 0.0022	6.6 ± 1.6
5	668	0.0100 ± 0.0022	6.7 ± 1.5
6	77	0.0103 ± 0.0021	0.79 ± 0.19
7	1551	0.0090 ± 0.0020	13.9 ± 3.2
8	410	0.0086 ± 0.0018	3.53 ± 0.75
9	249	0.0096 ± 0.0022	2.39 ± 0.56
10	136	0.0092 ± 0.0020	1.26 ± 0.30
11	104	0.0096 ± 0.0021	1.00 ± 0.24
12	255	0.0087 ± 0.0018	2.21 ± 0.47
13	75	0.0095 ± 0.0019	0.72 ± 0.16
14	44	0.0086 ± 0.0019	0.38 ± 0.10
15	20	0.0084 ± 0.0016	0.17 ± 0.05
16	17	0.0117 ± 0.0024	0.20 ± 0.06
17	3879	0.0084 ± 0.0019	32.4 ± 7.5
18	861	0.0083 ± 0.0019	7.1 ± 1.7
19	435	0.0087 ± 0.0021	3.79 ± 0.92
20	232	0.0086 ± 0.0019	2.00 ± 0.45
21	172	0.0094 ± 0.0021	1.62 ± 0.38
22	2322	0.0085 ± 0.0018	19.8 ± 4.3
23	635	0.0087 ± 0.0019	5.5 ± 1.2
24	331	0.0090 ± 0.0018	2.98 ± 0.63
25	169	0.0082 ± 0.0016	1.38 ± 0.30
26	80	0.0083 ± 0.0016	0.67 ± 0.15
27	740	0.0087 ± 0.0017	6.4 ± 1.3
28	184	0.0092 ± 0.0019	1.68 ± 0.37
29	98	0.0075 ± 0.0014	0.73 ± 0.16
30	57	0.0076 ± 0.0015	0.44 ± 0.10
31	26	0.0089 ± 0.0018	0.23 ± 0.07

TABLE A.5: Observed single electron yields, after accounting for lepton scale factors and relative trigger efficiencies factor, in each of the low- $\Delta\phi$ control regions, the average scale factor due to MC-based fake rates and data/MC fake rate correction factors from T&P measurements, and the corresponding fake-rate predictions with all the uncertainties (statistical and systematic) taken into consideration.

Bin	Obs. e events	Avg. transfer factor	Prediction
1	994	0.0122 ± 0.0050	12.2 ± 5.0
2	177	0.0127 ± 0.0049	2.24 ± 0.89
3	100	0.0117 ± 0.0044	1.17 ± 0.45
4	59	0.0140 ± 0.0059	0.82 ± 0.37
5	33	0.0127 ± 0.0050	0.42 ± 0.18
6	3	0.0154 ± 0.0053	0.05 ± 0.03
7	207	0.0116 ± 0.0041	2.41 ± 0.87
8	43	0.0112 ± 0.0040	0.48 ± 0.19
9	14	0.0071 ± 0.0023	0.10 ± 0.04
10	3	0.0179 ± 0.0048	0.05 ± 0.03
11	3	0.0222 ± 0.0097	0.07 ± 0.05
12	36	0.0106 ± 0.0036	0.38 ± 0.14
13	8	0.0080 ± 0.0022	0.06 ± 0.03
14	3	0.0075 ± 0.0029	0.02 ± 0.02
15	2	0.0185 ± 0.0053	0.04 ± 0.03
16	0	0.0222 ± 0.0097	0.00 ± 0.04
17	513	0.0115 ± 0.0043	5.9 ± 2.2
18	132	0.0120 ± 0.0044	1.58 ± 0.59
19	58	0.0100 ± 0.0037	0.58 ± 0.23
20	23	0.0133 ± 0.0043	0.31 ± 0.12
21	26	0.0106 ± 0.0041	0.28 ± 0.12
22	358	0.0112 ± 0.0040	4.0 ± 1.5
23	80	0.0110 ± 0.0037	0.88 ± 0.31
24	35	0.0092 ± 0.0030	0.32 ± 0.12
25	20	0.0102 ± 0.0029	0.20 ± 0.07
26	8	0.0089 ± 0.0054	0.07 ± 0.05
27	106	0.0117 ± 0.0039	1.24 ± 0.43
28	23	0.0110 ± 0.0030	0.25 ± 0.09
29	15	0.0115 ± 0.0048	0.17 ± 0.09
30	6	0.0115 ± 0.0028	0.07 ± 0.03
31	2	0.0073 ± 0.0018	0.01 ± 0.01

A.3 Invisible Z estimation

TABLE A.6: $Z(\nu\nu) + \gamma$ MC yields and prediction for the high $\Delta\phi$ regions.

Bin	MC Yield	Prediction
1	80.90 ± 0.68	92 ± 17
2	29.46 ± 0.41	33.6 ± 8.3
3	20.06 ± 0.34	22.9 ± 6.0
4	14.90 ± 0.29	17.0 ± 5.2
5	15.92 ± 0.30	18.1 ± 7.1
6	2.46 ± 0.12	2.8 ± 1.2
7	7.30 ± 0.23	8.3 ± 1.6
8	2.71 ± 0.14	3.09 ± 0.78
9	1.74 ± 0.12	1.98 ± 0.54
10	1.31 ± 0.10	1.49 ± 0.47
11	1.44 ± 0.11	1.65 ± 0.65
12	0.70 ± 0.08	0.80 ± 0.18
13	0.32 ± 0.06	0.37 ± 0.11
14	0.21 ± 0.05	0.24 ± 0.08
15	0.14 ± 0.04	0.16 ± 0.07
16	0.15 ± 0.03	0.17 ± 0.08
17	8.43 ± 0.14	9.6 ± 1.8
18	3.12 ± 0.08	3.55 ± 0.89
19	2.15 ± 0.07	2.45 ± 0.65
20	1.59 ± 0.05	1.81 ± 0.55
21	1.88 ± 0.06	2.14 ± 0.84
22	1.63 ± 0.08	1.86 ± 0.36
23	0.67 ± 0.06	0.76 ± 0.20
24	0.43 ± 0.04	0.49 ± 0.14
25	0.28 ± 0.03	0.32 ± 0.11
26	0.42 ± 0.06	0.48 ± 0.20
27	0.19 ± 0.02	0.21 ± 0.05
28	0.12 ± 0.02	0.13 ± 0.04
29	0.09 ± 0.03	0.10 ± 0.04
30	0.06 ± 0.02	0.07 ± 0.03
31	0.04 ± 0.01	0.04 ± 0.02

TABLE A.7: $Z(\nu\nu) + \gamma$ MC yields and prediction for the low $\Delta\phi$ regions.

Bin	MC Yield	Prediction
1	19.13 ± 0.32	21.3 ± 4.4
2	7.46 ± 0.22	8.3 ± 2.2
3	4.52 ± 0.17	5.0 ± 1.4
4	2.91 ± 0.14	3.2 ± 1.0
5	2.01 ± 0.12	2.24 ± 0.90
6	0.16 ± 0.03	0.18 ± 0.09
7	1.77 ± 0.14	1.97 ± 0.43
8	0.72 ± 0.09	0.80 ± 0.23
9	0.51 ± 0.08	0.57 ± 0.18
10	0.24 ± 0.05	0.26 ± 0.10
11	0.20 ± 0.04	0.23 ± 0.10
12	0.21 ± 0.05	0.23 ± 0.07
13	0.12 ± 0.04	0.14 ± 0.06
14	0.04 ± 0.01	0.04 ± 0.02
15	0.02 ± 0.01	0.03 ± 0.01
16	0.02 ± 0.01	0.03 ± 0.01
17	2.05 ± 0.07	2.28 ± 0.49
18	0.81 ± 0.05	0.90 ± 0.24
19	0.48 ± 0.03	0.53 ± 0.15
20	0.34 ± 0.03	0.38 ± 0.13
21	0.28 ± 0.04	0.31 ± 0.13
22	0.54 ± 0.08	0.60 ± 0.15
23	0.16 ± 0.03	0.17 ± 0.06
24	0.11 ± 0.03	0.12 ± 0.04
25	0.06 ± 0.01	0.06 ± 0.02
26	0.07 ± 0.02	0.08 ± 0.04
27	0.06 ± 0.01	0.06 ± 0.02
28	0.04 ± 0.02	0.04 ± 0.02
29	0.01 ± 0.01	0.02 ± 0.01
30	0.008 ± 0.003	0.009 ± 0.005
31	0.006 ± 0.003	0.007 ± 0.004

A.4 $\gamma + \text{jets}$ and QCD multijet

TABLE A.8: Fake p_T^{miss} background control sample statistics and electroweak predictions with uncertainties.

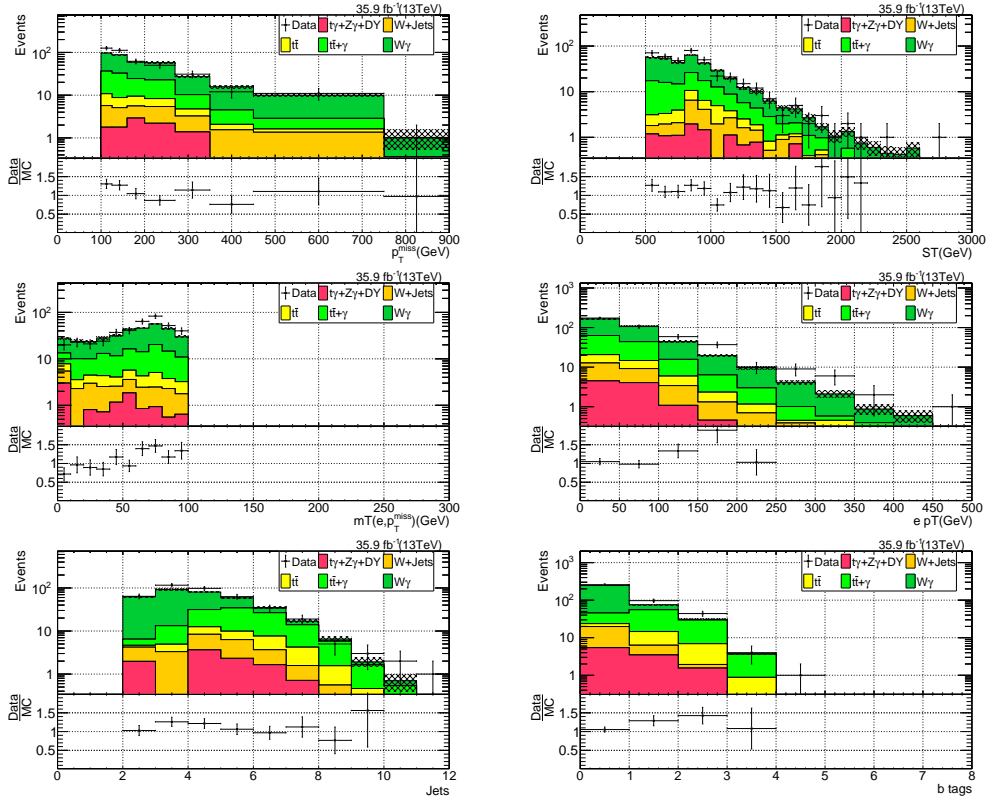
$N_{\text{jets}}^{\text{b-jets}}$	Bin	Low $\Delta\phi$ raw	EW low $\Delta\phi$	$\gamma + \text{jets}$ low $\Delta\phi$	$\gamma + \text{jets}$ high $\Delta\phi$
N_{2-4}^0	1	5109	88 ± 11	5020 ± 72	3994 ± 112
	2	286	28.3 ± 4.2	258 ± 17	60 ± 11
	3	101	12.5 ± 2.4	88 ± 10	20.5 ± 4.3
	4	26	8.3 ± 1.9	17.7 ± 5.4	4.1 ± 1.4
	5	21	10.3 ± 2.3	10.7 ± 5.1	2.5 ± 1.3
	6	2	$0.23^{+1.10}_{-0.23}$	1.8 ± 1.8	$0.41^{+0.42}_{-0.41}$
N_{5-6}^0	7	710	13.4 ± 2.7	697 ± 27	654 ± 45
	8	38	1.99 ± 0.64	36.0 ± 6.2	15.8 ± 4.8
	9	11	2.6 ± 1.0	8.4 ± 3.5	3.7 ± 1.8
	10	4	1.2 ± 0.6	2.8 ± 2.1	1.23 ± 0.97
	11	1	0.84 ± 0.63	$0.2^{+1.2}_{-0.2}$	$0.00^{+0.52}_{-0.00}$
$N_{\geq 7}^0$	12	89	2.60 ± 1.0	86.4 ± 9.5	90 ± 17
	13	6	1.56 ± 0.95	4.4 ± 2.6	1.8 ± 1.2
	14	3	$0.06^{+1.1}_{-0.06}$	2.9 ± 2.1	1.22 ± 0.94
	15	1	0.83 ± 0.65	$0.17^{+1.2}_{-0.17}$	0.07 ± 0.50
	16	0	$0.62^{+0.70}_{-0.62}$	$0.0^{+1.8}_{-0.0}$	$0.00^{+0.75}_{-0.00}$
$N_{2-4}^{\geq 1}$	17	1320	37.2 ± 6.4	1283 ± 37	838 ± 48
	18	78	6.3 ± 1.7	71 ± 9	11.3 ± 3.3
	19	39	2.8 ± 1.1	36.2 ± 6.3	5.7 ± 1.8
	20	5	1.2 ± 1.3	3.8 ± 2.6	0.59 ± 0.44
	21	8	2.0 ± 1.1	6.0 ± 3.0	0.95 ± 0.54
$N_{5-6}^{\geq 1}$	22	319	16.8 ± 3.7	302 ± 18	275 ± 31
	23	28	3.4 ± 1.0	24.6 ± 5.4	7.7 ± 2.4
	24	8	1.23 ± 0.61	6.8 ± 2.9	2.1 ± 1.0
	25	2	1.05 ± 0.61	$0.95^{+1.5}_{-0.95}$	$0.30^{+0.49}_{-0.30}$
	26	1	1.19 ± 0.66	$0.0^{+1.8}_{-0.0}$	$0.00^{+0.56}_{-0.00}$
$N_{\geq 7}^{\geq 1}$	27	61	4.2 ± 1.3	56.8 ± 7.9	74 ± 18
	28	12	2.4 ± 1.0	9.6 ± 3.6	5.9 ± 5.0
	29	0	$0.44^{+0.99}_{-0.00}$	$0.0^{+1.8}_{-0.0}$	$0.0^{+1.1}_{-0.0}$
	30	0	0.33 ± 0.99	$0.0^{+1.8}_{-0.0}$	$0.0^{+1.1}_{-0.0}$
	31	0	$0.02^{+1.1}_{-0.00}$	$0.0^{+1.8}_{-0.0}$	$0.0^{+1.1}_{-0.0}$

Appendix B

Data verses MC in control regions

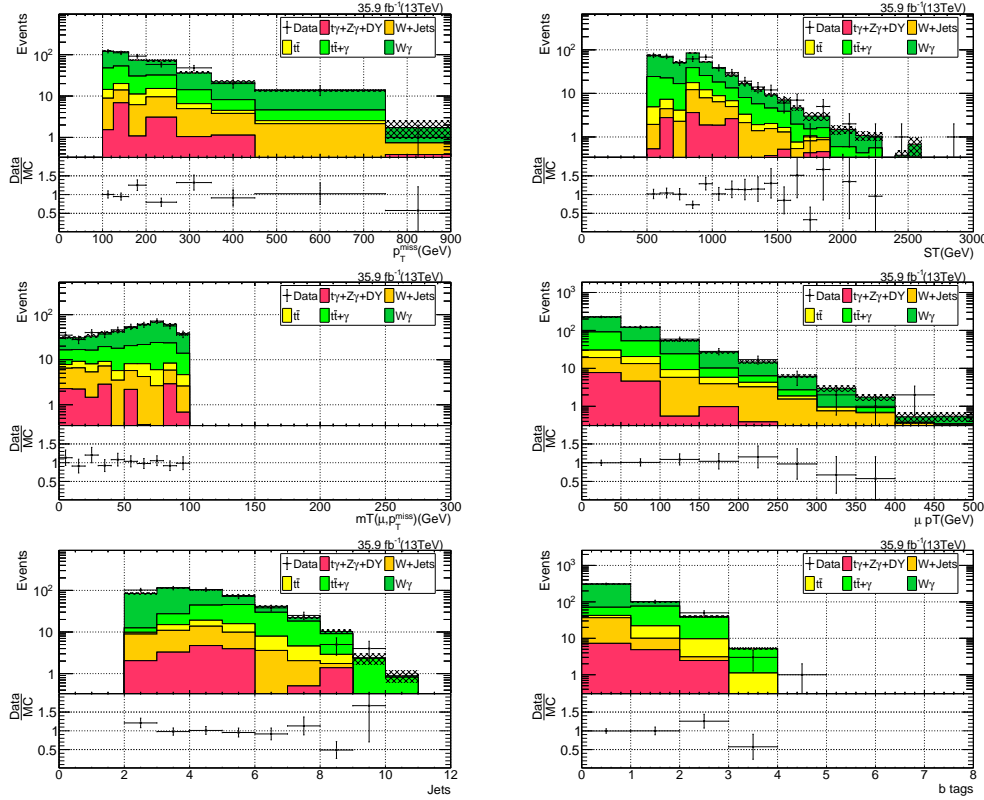
B.1 $e/\mu + \gamma$ control region

FIGURE B.1: Distribution of $e + \gamma$ events versus p_T^{miss} (top left), H_T^γ (top right), m_T (middle left), $p_{T,e}$ (middle right), N_{jets} (bottom left), $N_{b\text{-jets}}$ (bottom right). Filled histograms denote expected yields from MC for various processes. Markers represent data yields. MC event yields are scaled to the same integrated luminosity as data.



Comparisons of the observed yields and expected MC yields for the electron and muon control regions in Figures B.2 and B.1. While the agreement between data and MC expectations is not directly required, MC modeling of ratios of events can affect the lost lepton prediction. Thus, data-MC comparisons of the control region represent an important validation of the systematic uncertainties of the transfer factors. MC modeling of the various analysis variables used to define the signal regions are generally found to have good agreement with data. For the $e + \gamma$ CR the p_T , p_T^{miss} , and m_T distributions are found to have differing shapes for data and MC. This could

FIGURE B.2: Distribution of $\mu + \gamma$ events versus p_T^{miss} (top left), S_T (top right), M_T (middle left), $p_{T,\mu}$ (middle right), N_{jets} (bottom left), N_b -jets (bottom right). Filled histograms denote expected yields from MC for various processes. Markers represent data yields. MC event yields are scaled to the same integrated luminosity as data.



be because of some mis-modelling in the electron p_T and p_T^{miss} which affect m_T distribution since m_T is derived from p_T^{miss} and electron p_T . Effect of electron p_T mis-modeling can have maximum 10% effect on TF. Since the existing uncertainty on TF is 15-25%, this systematic effect(if any) is already covered. In low p_T^{miss} bins(100-200 GeV), data-MC differences is found to be 20%. The low p_T^{miss} region is used as a sideband for multijet estimation and it does not correspond to any signal region. Lost electron contribution is very negligible in this sideband and it is dominated by multijet. So these differences are going to have very small effect (1-2% or less) on multijet prediction.

All yields are computed after applying the b-tagging scale factors [77] and lepton scale factors to MC.

B.2 $Z(\ell\ell)+\gamma$ control region

A comparison of $ll + \gamma$ events in data with MC is shown in figure B.3. In top left plot, since di-lepton pair is ignored, p_T of the pair contributes to p_T^{miss} . Data agrees well with MC, within the statistical uncertainties.

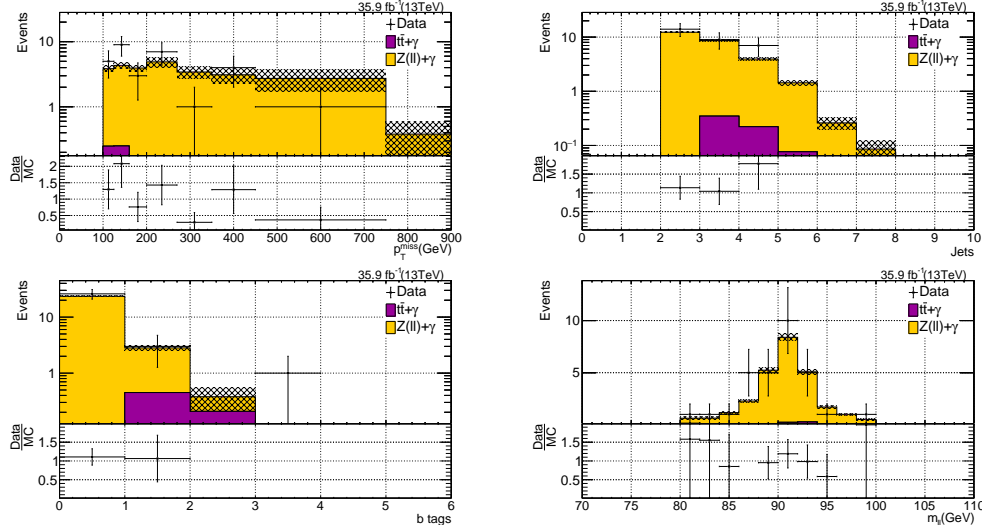


FIGURE B.3: Comparison of $ll + \gamma$ in data with $ll + \gamma$ events in MC as function of p_T^{miss} (top left), N_{jets} (top right), $N_{\text{b-jets}}$ (bottom left) and m_{ll} (bottom right) for $p_T^\gamma > 190\text{GeV}$. Note that p_T^{miss} is calculated by ignoring the di-lepton pair. For the top left plot of p_T^{miss} , hashed error bars refer to statistical and EW correction uncertainties listed in Table 4.6. For the remaining 3 plots, error bars are statistical only.

B.3 Signal acceptance \times efficiency

Signal acceptance \times efficiency is studied for different signal models and they are shown in figure B.4. To some extent acceptance \times efficiency is related to sensitivity of the analysis. Other factors such as background composition in different search bins, signal kinematics and cross section also affect the sensitivity and hence the exclusion limits. These plots are useful to in understanding some of the features seen in exclusion curves- low sensitivity near diagonal and kink for very low NLSP masses etc.

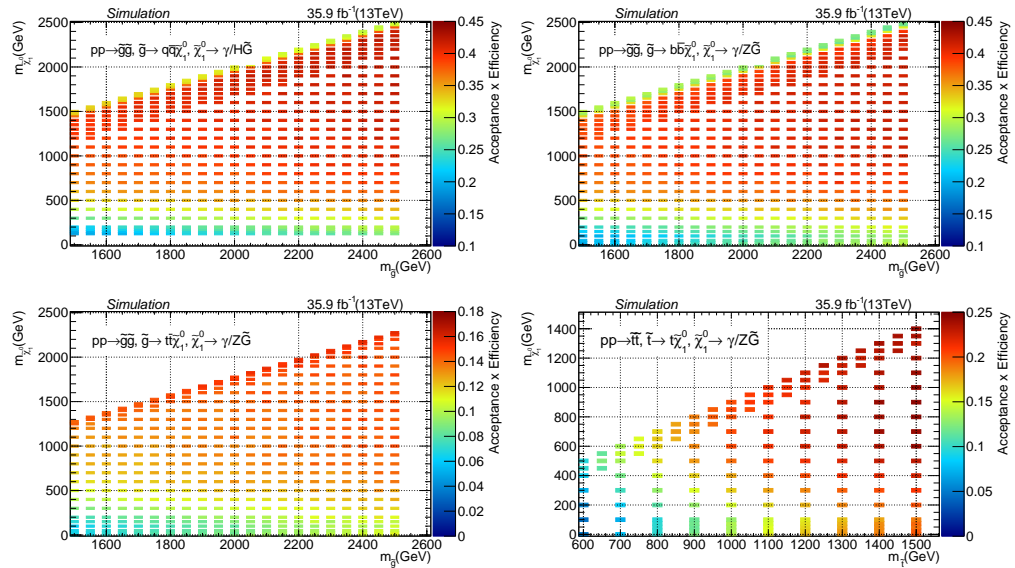


FIGURE B.4: Acceptance × efficiency for different mass points corresponding to T5qqqqHG (top left), T5bbbbZG (top right), T5ttttZG (bottom left) and T6ttZG (bottom right).

Appendix C

Data cleaning

In 2016 data there was an issue in ECAL pulse reconstruction. A correction to mitigate the effect was applied to electron and photon objects, but the PF candidates, which are inputs to both jets and p_T^{miss} , are not modified. Instead the correction was propagated to p_T^{miss} based on ΔR matching of these objects while jets are left unmodified. While most of the events where corrections are not properly propagated are rejected by $\Delta\phi$ cuts between leading two jets and p_T^{miss} directions, a few events still seem to survive after various selections. To account for residual effects of this reconstruction feature on this analysis, $p_T^{jet}/p_T^\gamma \geq 1$ where the jet and photon are matching within $\Delta R < 0.3$. Since a jet matching to a photon is nothing but the photon candidate clustered with neighboring activities, the p_T^{jet} is expected to be higher than p_T^γ . This is verified to be so in MC with p_T^{jet}/p_T^γ as a function of p_T^γ as shown in Figures C.1 top-left for low- $\Delta\phi$ region with $p_T^{miss} > 100$ GeV and top-right for high- $\Delta\phi$ region with $100 < p_T^{miss} < 200$ GeV. The same quantities for these event selection show a distinct population in data events as shown in bottom row of Figure C.1.

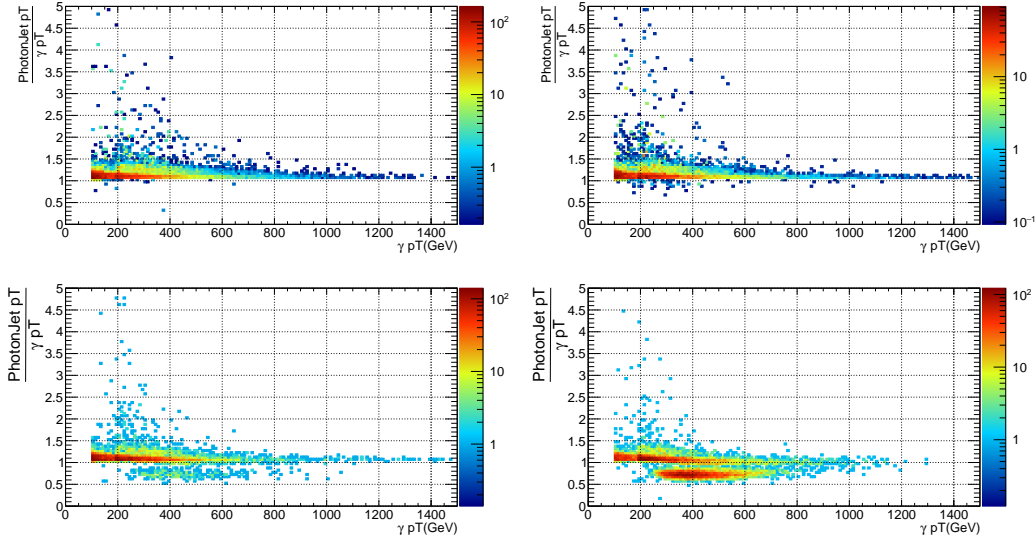


FIGURE C.1: Left column: p_T^{jet}/p_T^γ as a function of p_T^γ in low- $\Delta\phi$ region with $p_T^{miss} > 100$ GeV region for events in $\gamma +$ jets events in MC (top-left) and for data (bottom-left). Right column: same quantities in high- $\Delta\phi$ region with $100 < p_T^{miss} < 200$ GeV for $\gamma +$ jets events in MC (top-right) and for data (bottom-right).

Bibliography

- [1] S. Weinberg. "A Model of Leptons". In: *Phys. Rev. Lett.* 19 (21 1967), pp. 1264–1266. DOI: [10.1103/PhysRevLett.19.1264](https://doi.org/10.1103/PhysRevLett.19.1264). URL: <https://link.aps.org/doi/10.1103/PhysRevLett.19.1264>.
- [2] A. Salam. "Gauge unification of fundamental forces". In: *Rev. Mod. Phys.* 52 (3 1980), pp. 525–538. DOI: [10.1103/RevModPhys.52.525](https://doi.org/10.1103/RevModPhys.52.525). URL: <https://link.aps.org/doi/10.1103/RevModPhys.52.525>.
- [3] S. L. Glashow. "Partial-symmetries of weak interactions". In: *Nuclear Physics* 22.4 (1961), pp. 579 –588. ISSN: 0029-5582. DOI: [https://doi.org/10.1016/0029-5582\(61\)90469-2](https://doi.org/10.1016/0029-5582(61)90469-2). URL: <http://www.sciencedirect.com/science/article/pii/0029558261904692>.
- [4] B. Odom et al. "New Measurement of the Electron Magnetic Moment Using a One-Electron Quantum Cyclotron". In: *Phys. Rev. Lett.* 97 (3 2006), p. 030801. DOI: [10.1103/PhysRevLett.97.030801](https://doi.org/10.1103/PhysRevLett.97.030801). URL: <https://link.aps.org/doi/10.1103/PhysRevLett.97.030801>.
- [5] F. Zwicky. "Die Rotverschiebung von extragalaktischen Nebeln". In: *Helv. Phys. Acta* 6 (1933), p. 110. URL: <http://adsabs.harvard.edu/abs/1933AcHPh..6..110Z>.
- [6] D. Clowe et al. "A direct empirical proof of the existence of dark matter". In: *Astrophys. J.* 648 (2006), pp. L109–L113. DOI: [10.1086/508162](https://doi.org/10.1086/508162). arXiv: [astro-ph/0608407 \[astro-ph\]](https://arxiv.org/abs/astro-ph/0608407).
- [7] A. G. Riess et al. "Observational evidence from supernovae for an accelerating universe and a cosmological constant". In: *Astron. J.* 116 (1998), pp. 1009–1038. DOI: [10.1086/300499](https://doi.org/10.1086/300499). arXiv: [astro-ph/9805201 \[astro-ph\]](https://arxiv.org/abs/astro-ph/9805201).
- [8] G. Steigman. "Observational Tests of Antimatter Cosmologies". In: *Annual Review of Astronomy and Astrophysics* 14.1 (1976), pp. 339–372. DOI: [10.1146/annurev.aa.14.090176.002011](https://doi.org/10.1146/annurev.aa.14.090176.002011). eprint: <https://doi.org/10.1146/annurev.aa.14.090176.002011>. URL: <https://doi.org/10.1146/annrev.aa.14.090176.002011>.
- [9] L. Canetti, M. Drewes, and M. Shaposhnikov. "Matter and Antimatter in the Universe". In: *New J. Phys.* 14 (2012), p. 095012. DOI: [10.1088/1367-2630/14/9/095012](https://doi.org/10.1088/1367-2630/14/9/095012). arXiv: [1204.4186 \[hep-ph\]](https://arxiv.org/abs/1204.4186).
- [10] G. 't Hooft. "Naturalness, chiral symmetry, and spontaneous chiral symmetry breaking". In: *NATO Sci. Ser. B* 59 (1980), pp. 135–157. DOI: [10.1007/978-1-4684-7571-5_9](https://doi.org/10.1007/978-1-4684-7571-5_9).
- [11] M. Tanabashi, K. Hagiwara, K. Hikasa, et al. "Review of Particle Physics". In: *Phys. Rev. D* 98 (3 2018), p. 030001. DOI: [10.1103/PhysRevD.98.030001](https://doi.org/10.1103/PhysRevD.98.030001). URL: <https://link.aps.org/doi/10.1103/PhysRevD.98.030001>.
- [12] E. Noether. "Invariante Variationsprobleme". ger. In: *Nachrichten von der Gesellschaft der Wissenschaften zu Göttingen, Mathematisch-Physikalische Klasse* 1918 (1918), pp. 235–257. URL: <http://eudml.org/doc/59024>.

- [13] D. Griffiths. *Introduction to elementary particles*. 2008. ISBN: 9783527406012.
- [14] D. J. Gross and F. Wilczek. "Ultraviolet Behavior of Non-Abelian Gauge Theories". In: *Phys. Rev. Lett.* 30 (26 1973), pp. 1343–1346. DOI: [10.1103/PhysRevLett.30.1343](https://doi.org/10.1103/PhysRevLett.30.1343). URL: <https://link.aps.org/doi/10.1103/PhysRevLett.30.1343>.
- [15] H. D. Politzer. "Reliable Perturbative Results for Strong Interactions?" In: *Phys. Rev. Lett.* 30 (26 1973), pp. 1346–1349. DOI: [10.1103/PhysRevLett.30.1346](https://doi.org/10.1103/PhysRevLett.30.1346). URL: <https://link.aps.org/doi/10.1103/PhysRevLett.30.1346>.
- [16] A. Salam and J. C. Ward. "Weak and electromagnetic interactions". In: *Il Nuovo Cimento (1955-1965)* 11.4 (1959), pp. 568–577. ISSN: 1827-6121. DOI: [10.1007/BF02726525](https://doi.org/10.1007/BF02726525). URL: <https://doi.org/10.1007/BF02726525>.
- [17] S. L. Glashow. "The renormalizability of vector meson interactions". In: *Nucl. Phys.* 10 (1959), pp. 107–117. DOI: [10.1016/0029-5582\(59\)90196-8](https://doi.org/10.1016/0029-5582(59)90196-8).
- [18] G. Arnison et al. "Experimental observation of isolated large transverse energy electrons with associated missing energy at $\sqrt{s} = 540 \text{ GeV}$ ". In: *Physics Letters B* 122.1 (1983), pp. 103 –116. ISSN: 0370-2693. DOI: [https://doi.org/10.1016/0370-2693\(83\)91177-2](https://doi.org/10.1016/0370-2693(83)91177-2). URL: <http://www.sciencedirect.com/science/article/pii/0370269383911772>.
- [19] M. Banner et al. "Observation of single isolated electrons of high transverse momentum in events with missing transverse energy at the CERN pp collider". In: *Physics Letters B* 122.5 (1983), pp. 476 –485. ISSN: 0370-2693. DOI: [https://doi.org/10.1016/0370-2693\(83\)91605-2](https://doi.org/10.1016/0370-2693(83)91605-2). URL: <http://www.sciencedirect.com/science/article/pii/0370269383916052>.
- [20] G. Arnison et al. "Experimental observation of lepton pairs of invariant mass around $95 \text{ GeV}/c^2$ at the CERN SPS collider". In: *Physics Letters B* 126.5 (1983), pp. 398 –410. ISSN: 0370-2693. DOI: [https://doi.org/10.1016/0370-2693\(83\)90188-0](https://doi.org/10.1016/0370-2693(83)90188-0). URL: <http://www.sciencedirect.com/science/article/pii/0370269383901880>.
- [21] P. Bagnaia et al. "Evidence for $Z^0 \rightarrow e^+e^-$ CERN pp collider". In: *Physics Letters B* 129.1 (1983), pp. 130 –140. ISSN: 0370-2693. DOI: [https://doi.org/10.1016/0370-2693\(83\)90744-X](https://doi.org/10.1016/0370-2693(83)90744-X). URL: <http://www.sciencedirect.com/science/article/pii/037026938390744X>.
- [22] B. Martin and G. Shaw. *Particle Physics*. 3rd ed. John Wiley & Sons.
- [23] P. W. Higgs. "Broken Symmetries and the Masses of Gauge Bosons". In: *Phys. Rev. Lett.* 13 (1964). [,160(1964)], pp. 508–509. DOI: [10.1103/PhysRevLett.13.508](https://doi.org/10.1103/PhysRevLett.13.508).
- [24] F. Englert and R. Brout. "Broken Symmetry and the Mass of Gauge Vector Mesons". In: *Phys. Rev. Lett.* 13 (1964). [,157(1964)], pp. 321–323. DOI: [10.1103/PhysRevLett.13.321](https://doi.org/10.1103/PhysRevLett.13.321).
- [25] G. Aad et al. "Observation of a new particle in the search for the Standard Model Higgs boson with the ATLAS detector at the LHC". In: *Phys. Lett. B* 716 (2012), p. 1. DOI: [10.1016/j.physletb.2012.08.020](https://doi.org/10.1016/j.physletb.2012.08.020). arXiv: [1207.7214 \[hep-ex\]](https://arxiv.org/abs/1207.7214).
- [26] S. Chatrchyan et al. "Observation of a new boson at a mass of 125 GeV with the CMS experiment at the LHC". In: *Phys. Lett. B* 716 (2012), pp. 30–61. DOI: [10.1016/j.physletb.2012.08.021](https://doi.org/10.1016/j.physletb.2012.08.021). arXiv: [1207.7235 \[hep-ex\]](https://arxiv.org/abs/1207.7235).
- [27] CMS Collaboration. "Summaries of CMS cross section measurements". URL: <https://twiki.cern.ch/twiki/bin/view/CMSPublic/PhysicsResultsCombined>.

- [28] Y. Fukuda et al. "Evidence for oscillation of atmospheric neutrinos". In: *Phys. Rev. Lett.* 81 (1998), pp. 1562–1567. DOI: [10.1103/PhysRevLett.81.1562](https://doi.org/10.1103/PhysRevLett.81.1562). arXiv: [hep-ex/9807003 \[hep-ex\]](https://arxiv.org/abs/hep-ex/9807003).
- [29] H. Baer and X. Tata. "The Minimal Supersymmetric Standard Model". In: *Weak Scale Supersymmetry: From Superfields to Scattering Events*. Cambridge University Press, 2006, 127–189. DOI: [10.1017/CBO9780511617270.009](https://doi.org/10.1017/CBO9780511617270.009).
- [30] S. P. Martin. "A supersymmetry primer". In: *Adv. Ser. Direct. High Energy Phys.* 21 (2010), p. 1. DOI: [10.1142/9789814307505_0001](https://doi.org/10.1142/9789814307505_0001). arXiv: [hep-ph/9709356 \[hep-ph\]](https://arxiv.org/abs/hep-ph/9709356).
- [31] C. Rizzi, A. Juste Rozas, and M. P. Casado Lechuga. "Searches for supersymmetric particles in final states with multiple top and bottom quarks with the ATLAS detector". Presented 15 Oct 2018. 2018. URL: <http://cds.cern.ch/record/2646377>.
- [32] H. Nishino et al. "Search for Proton Decay via $p \rightarrow e^+ \pi^0$ and $p \rightarrow \mu^+ \pi^0$ in a Large Water Cherenkov Detector". In: *Phys. Rev. Lett.* 102 (14 2009), p. 141801. DOI: [10.1103/PhysRevLett.102.141801](https://doi.org/10.1103/PhysRevLett.102.141801). URL: <https://link.aps.org/doi/10.1103/PhysRevLett.102.141801>.
- [33] J. Ellis et al. "Supersymmetric relics from the big bang". In: *Nuclear Physics B* 238.2 (1984), pp. 453–476. ISSN: 0550-3213. DOI: [https://doi.org/10.1016/0550-3213\(84\)90461-9](https://doi.org/10.1016/0550-3213(84)90461-9). URL: <http://www.sciencedirect.com/science/article/pii/0550321384904619>.
- [34] M. Dine and A. E. Nelson. "Dynamical supersymmetry breaking at low-energies". In: *Phys. Rev.* D48 (1993), pp. 1277–1287. DOI: [10.1103/PhysRevD.48.1277](https://doi.org/10.1103/PhysRevD.48.1277). arXiv: [hep-ph/9303230 \[hep-ph\]](https://arxiv.org/abs/hep-ph/9303230).
- [35] M. Dine, A. E. Nelson, and Y. Shirman. "Low-energy dynamical supersymmetry breaking simplified". In: *Phys. Rev.* D51 (1995), pp. 1362–1370. DOI: [10.1103/PhysRevD.51.1362](https://doi.org/10.1103/PhysRevD.51.1362). arXiv: [hep-ph/9408384 \[hep-ph\]](https://arxiv.org/abs/hep-ph/9408384).
- [36] M. Dine et al. "New tools for low-energy dynamical supersymmetry breaking". In: *Phys. Rev.* D53 (1996), pp. 2658–2669. DOI: [10.1103/PhysRevD.53.2658](https://doi.org/10.1103/PhysRevD.53.2658). arXiv: [hep-ph/9507378 \[hep-ph\]](https://arxiv.org/abs/hep-ph/9507378).
- [37] P. Meade, N. Seiberg, and D. Shih. "General Gauge Mediation". In: *Prog. Theor. Phys. Suppl.* 177 (2009), p. 143. DOI: [10.1143/PTPS.177.143](https://doi.org/10.1143/PTPS.177.143). arXiv: [0801.3278 \[hep-ph\]](https://arxiv.org/abs/0801.3278).
- [38] G. F. Giudice and R. Rattazzi. "Theories with gauge mediated supersymmetry breaking". In: *Phys. Rept.* 322 (1999), pp. 419–499. DOI: [10.1016/S0370-1573\(99\)00042-3](https://doi.org/10.1016/S0370-1573(99)00042-3). arXiv: [hep-ph/9801271 \[hep-ph\]](https://arxiv.org/abs/hep-ph/9801271).
- [39] P. Grajek, A. Mariotti, and D. Redigolo. "Phenomenology of General Gauge Mediation in light of a 125 GeV Higgs". In: *JHEP* 07 (2013), p. 109. DOI: [10.1007/JHEP07\(2013\)109](https://doi.org/10.1007/JHEP07(2013)109). arXiv: [1303.0870 \[hep-ph\]](https://arxiv.org/abs/1303.0870).
- [40] S. Deser and B. Zumino. "Broken Supersymmetry and Supergravity". In: *Phys. Rev. Lett.* 38 (1977), p. 1433. DOI: [10.1103/PhysRevLett.38.1433](https://doi.org/10.1103/PhysRevLett.38.1433).
- [41] E. Cremmer et al. "Super-Higgs effect in supergravity with general scalar interactions". In: *Phys. Lett. B* 79 (1978), p. 231. ISSN: 0370-2693. DOI: [10.1016/0370-2693\(78\)90230-7](https://doi.org/10.1016/0370-2693(78)90230-7).
- [42] S. Knapen and D. Redigolo. "Gauge mediation at the LHC: status and prospects". In: *JHEP* 01 (2017), p. 135. DOI: [10.1007/JHEP01\(2017\)135](https://doi.org/10.1007/JHEP01(2017)135). arXiv: [1606.07501 \[hep-ph\]](https://arxiv.org/abs/1606.07501).

- [43] J. T. Ruderman and D. Shih. "General Neutralino NLSPs at the Early LHC". In: *JHEP* 08 (2012), p. 159. DOI: [10.1007/JHEP08\(2012\)159](https://doi.org/10.1007/JHEP08(2012)159). arXiv: [1103.6083 \[hep-ph\]](https://arxiv.org/abs/1103.6083).
- [44] N. Arkani-Hamed et al. "MAMBOSET: The path from LHC data to the new standard model via on-shell effective theories". 2007.
- [45] J. Alwall, P. C. Schuster, and N. Toro. "Simplified models for a first characterization of new physics at the LHC". In: *Phys. Rev. D* 79 (2009), p. 075020. DOI: [10.1103/PhysRevD.79.075020](https://doi.org/10.1103/PhysRevD.79.075020). arXiv: [0810.3921 \[hep-ph\]](https://arxiv.org/abs/0810.3921).
- [46] J. Alwall et al. "Model-independent jets plus missing energy searches". In: *Phys. Rev. D* 79 (2009), p. 015005. DOI: [10.1103/PhysRevD.79.015005](https://doi.org/10.1103/PhysRevD.79.015005). arXiv: [0809.3264 \[hep-ph\]](https://arxiv.org/abs/0809.3264).
- [47] D. Alves et al. "Simplified models for LHC new physics searches". In: *J. Phys. G* 39 (2012), p. 105005. DOI: [10.1088/0954-3899/39/10/105005](https://doi.org/10.1088/0954-3899/39/10/105005). arXiv: [1105.2838 \[hep-ph\]](https://arxiv.org/abs/1105.2838).
- [48] S. Chatrchyan et al. "Interpretation of searches for supersymmetry with simplified models". In: *Phys. Rev. D* 88 (2013), p. 052017. DOI: [10.1103/PhysRevD.88.052017](https://doi.org/10.1103/PhysRevD.88.052017). arXiv: [1301.2175 \[hep-ex\]](https://arxiv.org/abs/1301.2175).
- [49] O. S. Brüning et al. *LHC Design Report*. CERN Yellow Reports: Monographs. Geneva: CERN, 2004. URL: <https://cds.cern.ch/record/782076>.
- [50] J. Haffner. "The CERN accelerator complex. Complexe des accélérateurs du CERN". In: (2013). General Photo. URL: <https://cds.cern.ch/record/1621894>.
- [51] *LHCfaq*. 2017. URL: <https://home.cern/resources/brochure/accelerators/lhc-facts-and-figures>.
- [52] C. Patrignani et al. "Review of Particle Physics". In: *Chin. Phys. C* 40.10 (2016), p. 100001. DOI: [10.1088/1674-1137/40/10/100001](https://doi.org/10.1088/1674-1137/40/10/100001).
- [53] CMS Collaboration. *Public CMS Luminosity Information*. URL: https://twiki.cern.ch/twiki/bin/view/CMSPublic/LumiPublicResults#2016_proton_proton_collisions.
- [54] S. Chatrchyan et al. "The CMS experiment at the CERN LHC". In: *JINST* 3 (2008), S08004. DOI: [10.1088/1748-0221/3/08/S08004](https://doi.org/10.1088/1748-0221/3/08/S08004).
- [55] T. C. Collaboration. "Description and performance of track and primary-vertex reconstruction with the CMS tracker". In: *Journal of Instrumentation* 9.10 (2014), P10009–P10009. DOI: [10.1088/1748-0221/9/10/p10009](https://doi.org/10.1088/1748-0221/9/10/p10009). URL: <https://doi.org/10.1088%2F1748-0221%2F9%2F10%2Fp10009>.
- [56] C. Collaboration. "Performance of the CMS hadron calorimeter with cosmic ray muons and LHC beam data". In: *Journal of Instrumentation* 5.03 (2010), T03012–T03012. DOI: [10.1088/1748-0221/5/03/t03012](https://doi.org/10.1088/1748-0221/5/03/t03012). URL: <https://doi.org/10.1088%2F1748-0221%2F5%2F03%2Ft03012>.
- [57] A. M. Sirunyan et al. "Performance of the CMS muon detector and muon reconstruction with proton-proton collisions at $\sqrt{s} = 13$ TeV". In: *JINST* 13.06 (2018), P06015. DOI: [10.1088/1748-0221/13/06/P06015](https://doi.org/10.1088/1748-0221/13/06/P06015). arXiv: [1804.04528 \[physics.ins-det\]](https://arxiv.org/abs/1804.04528).
- [58] S. Chatrchyan et al. "The Performance of the CMS Muon Detector in Proton-Proton Collisions at $\sqrt{s} = 7$ TeV at the LHC". In: *JINST* 8 (2013), P11002. DOI: [10.1088/1748-0221/8/11/P11002](https://doi.org/10.1088/1748-0221/8/11/P11002). arXiv: [1306.6905 \[physics.ins-det\]](https://arxiv.org/abs/1306.6905).

- [59] C. Borschensky et al. “Squark and gluino production cross sections in pp collisions at $\sqrt{s} = 13, 14, 33$ and 100 TeV”. In: *Eur. Phys. J. C* 74 (2014), p. 3174. DOI: [10.1140/epjc/s10052-014-3174-y](https://doi.org/10.1140/epjc/s10052-014-3174-y). arXiv: [1407.5066 \[hep-ph\]](https://arxiv.org/abs/1407.5066).
- [60] V. Khachatryan et al. “The CMS trigger system”. In: *JINST* 12 (2017), P01020. DOI: [10.1088/1748-0221/12/01/P01020](https://doi.org/10.1088/1748-0221/12/01/P01020). arXiv: [1609.02366 \[physics.ins-det\]](https://arxiv.org/abs/1609.02366).
- [61] A. M. Sirunyan et al. “Particle-flow reconstruction and global event description with the CMS detector”. In: *JINST* 12 (2017), P10003. DOI: [10.1088/1748-0221/12/10/P10003](https://doi.org/10.1088/1748-0221/12/10/P10003). arXiv: [1706.04965 \[physics.ins-det\]](https://arxiv.org/abs/1706.04965).
- [62] W Adam et al. “Reconstruction of electrons with the Gaussian-sum filter in the CMS tracker at the LHC”. In: *Journal of Physics G: Nuclear and Particle Physics* 31.9 (2005), N9–N20. DOI: [10.1088/0954-3899/31/9/n01](https://doi.org/10.1088/0954-3899/31/9/n01). URL: <https://doi.org/10.1088/0954-3899/31/9/2F9%2Fn01>.
- [63] S. Chatrchyan et al. “Description and performance of track and primary-vertex reconstruction with the CMS tracker”. In: *JINST* 9.10 (2014), P10009. DOI: [10.1088/1748-0221/9/10/P10009](https://doi.org/10.1088/1748-0221/9/10/P10009). arXiv: [1405.6569 \[physics.ins-det\]](https://arxiv.org/abs/1405.6569).
- [64] K. Rose. “Deterministic annealing for clustering, compression, classification, regression, and related optimization problems”. In: *Proceedings of the IEEE* 86.11 (1998), pp. 2210–2239. ISSN: 0018-9219. DOI: [10.1109/5.726788](https://doi.org/10.1109/5.726788).
- [65] R. Fruhwirth, W. Waltenberger, and P. Vanlaer. “Adaptive vertex fitting”. In: *J. Phys.* G34 (2007), N343. DOI: [10.1088/0954-3899/34/12/N01](https://doi.org/10.1088/0954-3899/34/12/N01).
- [66] M. Cacciari, G. P. Salam, and G. Soyez. “The anti- k_T jet clustering algorithm”. In: *JHEP* 04 (2008), p. 063. DOI: [10.1088/1126-6708/2008/04/063](https://doi.org/10.1088/1126-6708/2008/04/063). arXiv: [0802.1189 \[hep-ph\]](https://arxiv.org/abs/0802.1189).
- [67] M. Cacciari, G. P. Salam, and G. Soyez. “FastJet user manual”. In: *Eur. Phys. J. C* 72 (2012), p. 1896. DOI: [10.1140/epjc/s10052-012-1896-2](https://doi.org/10.1140/epjc/s10052-012-1896-2). arXiv: [1111.6097 \[hep-ph\]](https://arxiv.org/abs/1111.6097).
- [68] S. Chatrchyan et al. “Performance of CMS muon reconstruction in pp collision events at $\sqrt{s} = 7$ TeV”. In: *JINST* 7 (2012), P10002. DOI: [10.1088/1748-0221/7/10/P10002](https://doi.org/10.1088/1748-0221/7/10/P10002). arXiv: [1206.4071 \[physics.ins-det\]](https://arxiv.org/abs/1206.4071).
- [69] V. Khachatryan et al. “Performance of electron reconstruction and selection with the CMS detector in proton-proton collisions at $\sqrt{s} = 8$ TeV”. In: *JINST* 10 (2015), P06005. DOI: [10.1088/1748-0221/10/06/P06005](https://doi.org/10.1088/1748-0221/10/06/P06005). arXiv: [1502.02701 \[physics.ins-det\]](https://arxiv.org/abs/1502.02701).
- [70] V. Khachatryan et al. “Performance of photon reconstruction and identification with the CMS detector in proton-proton collisions at $\sqrt{s} = 8$ TeV”. In: *JINST* 10 (2015), P08010. DOI: [10.1088/1748-0221/10/08/P08010](https://doi.org/10.1088/1748-0221/10/08/P08010). arXiv: [1502.02702 \[physics.ins-det\]](https://arxiv.org/abs/1502.02702).
- [71] K. Rehermann and B. Tweedie. “Efficient identification of boosted semileptonic top quarks at the LHC”. In: *JHEP* 03 (2011), p. 059. DOI: [10.1007/JHEP03\(2011\)059](https://doi.org/10.1007/JHEP03(2011)059). arXiv: [1007.2221 \[hep-ph\]](https://arxiv.org/abs/1007.2221).
- [72] R. Meyer and L. W. Feld. “Studies of the misidentification probability of electrons as photons with the CMS experiment in data recorded in 2015”. Presented 2016. 2016. URL: <https://cds.cern.ch/record/2239058>.
- [73] V. Khachatryan et al. “Jet energy scale and resolution in the CMS experiment in pp collisions at 8 TeV”. In: *JINST* 12 (2017), P02014. DOI: [10.1088/1748-0221/12/02/P02014](https://doi.org/10.1088/1748-0221/12/02/P02014). arXiv: [1607.03663 \[hep-ex\]](https://arxiv.org/abs/1607.03663).

- [74] S. Chatrchyan et al. “Determination of jet energy calibration and transverse momentum resolution in CMS”. In: *JINST* 6 (2011), P11002. DOI: [10.1088/1748-0221/6/11/P11002](https://doi.org/10.1088/1748-0221/6/11/P11002). arXiv: [1107.4277 \[physics.ins-det\]](https://arxiv.org/abs/1107.4277).
- [75] “Jet energy scale and resolution performance with 13 TeV data collected by CMS in 2016”. In: (2018). URL: <http://cds.cern.ch/record/2622157>.
- [76] “Jet energy scale and resolution performances with 13TeV data”. In: (2016). URL: <https://cds.cern.ch/record/2160347>.
- [77] A. M. Sirunyan et al. “Identification of heavy-flavour jets with the CMS detector in pp collisions at 13 TeV”. In: *JINST* 13 (2018), P05011. DOI: [10.1088/1748-0221/13/05/P05011](https://doi.org/10.1088/1748-0221/13/05/P05011). arXiv: [1712.07158 \[physics.ins-det\]](https://arxiv.org/abs/1712.07158).
- [78] CMS Collaboration. *CMS SUSY Results: Objects Efficiency*. URL: <https://twiki.cern.ch/twiki/bin/view/CMSPublic/SUSMoriond2017ObjectsEfficiency>.
- [79] CMS Collaboration. *Performance of missing energy reconstruction in 13 TeV pp collision data using the CMS detector*. CMS Physics Analysis Summary CMS-PAS-JME-16-004. 2016. URL: <http://cds.cern.ch/record/2205284>.
- [80] A. M. Sirunyan et al. “Search for supersymmetry in events with a photon, jets, b-jets, and missing transverse momentum in proton-proton collisions at 13 TeV”. In: (2019). arXiv: [1901.06726 \[hep-ex\]](https://arxiv.org/abs/1901.06726).
- [81] A. M. Sirunyan et al. “Search for supersymmetry in events with at least one photon, missing transverse momentum, and large transverse event activity in proton-proton collisions at $\sqrt{s} = 13$ TeV”. In: *JHEP* 12 (2017), p. 142. DOI: [10.1007/JHEP12\(2017\)142](https://doi.org/10.1007/JHEP12(2017)142). arXiv: [1707.06193 \[hep-ex\]](https://arxiv.org/abs/1707.06193).
- [82] J. Alwall et al. “The automated computation of tree-level and next-to-leading order differential cross sections, and their matching to parton shower simulations”. In: *JHEP* 07 (2014), p. 079. DOI: [10.1007/JHEP07\(2014\)079](https://doi.org/10.1007/JHEP07(2014)079). arXiv: [1405.0301 \[hep-ph\]](https://arxiv.org/abs/1405.0301).
- [83] A. Kalogeropoulos and J. Alwall. “The SysCalc code: A tool to derive theoretical systematic uncertainties”. 2018.
- [84] P. Artoisenet et al. “Automatic spin-entangled decays of heavy resonances in Monte Carlo simulations”. In: *JHEP* 03 (2013), p. 015. DOI: [10.1007/JHEP03\(2013\)015](https://doi.org/10.1007/JHEP03(2013)015). arXiv: [1212.3460 \[hep-ph\]](https://arxiv.org/abs/1212.3460).
- [85] M. Czakon and A. Mitov. “Top++: A Program for the Calculation of the Top-Pair Cross-Section at Hadron Colliders”. In: *Comput. Phys. Commun.* 185 (2014), p. 2930. DOI: [10.1016/j.cpc.2014.06.021](https://doi.org/10.1016/j.cpc.2014.06.021). arXiv: [1112.5675 \[hep-ph\]](https://arxiv.org/abs/1112.5675).
- [86] R. Gavin et al. “W Physics at the LHC with FEWZ 2.1”. In: *Comput. Phys. Commun.* 184 (2013), p. 208. DOI: [10.1016/j.cpc.2012.09.005](https://doi.org/10.1016/j.cpc.2012.09.005). arXiv: [1201.5896 \[hep-ph\]](https://arxiv.org/abs/1201.5896).
- [87] R. Gavin et al. “FEWZ 2.0: A code for hadronic Z production at next-to-next-to-leading order”. In: *Comput. Phys. Commun.* 182 (2011), p. 2388. DOI: [10.1016/j.cpc.2011.06.008](https://doi.org/10.1016/j.cpc.2011.06.008). arXiv: [1011.3540 \[hep-ph\]](https://arxiv.org/abs/1011.3540).
- [88] R. D. Ball et al. “Parton distributions for the LHC Run II”. In: *JHEP* 04 (2015), p. 040. DOI: [10.1007/JHEP04\(2015\)040](https://doi.org/10.1007/JHEP04(2015)040). arXiv: [1410.8849 \[hep-ph\]](https://arxiv.org/abs/1410.8849).
- [89] T. Sjöstrand et al. “An introduction to PYTHIA 8.2”. In: *Comput. Phys. Commun.* 191 (2015), p. 159. DOI: [10.1016/j.cpc.2015.01.024](https://doi.org/10.1016/j.cpc.2015.01.024). arXiv: [1410.3012 \[hep-ph\]](https://arxiv.org/abs/1410.3012).

- [90] V. Khachatryan et al. "Event generator tunes obtained from underlying event and multiparton scattering measurements". In: *Eur. Phys. J. C* 76 (2016), p. 155. DOI: [10.1140/epjc/s10052-016-3988-x](https://doi.org/10.1140/epjc/s10052-016-3988-x). arXiv: [1512.00815 \[hep-ex\]](https://arxiv.org/abs/1512.00815).
- [91] J. Alwall et al. "Comparative study of various algorithms for the merging of parton showers and matrix elements in hadronic collisions". In: *Eur. Phys. J. C* 53 (2008), p. 473. DOI: [10.1140/epjc/s10052-007-0490-5](https://doi.org/10.1140/epjc/s10052-007-0490-5). arXiv: [0706.2569 \[hep-ph\]](https://arxiv.org/abs/0706.2569).
- [92] R. Frederix and S. Frixione. "Merging meets matching in MC@NLO". In: *JHEP* 12 (2012), p. 061. DOI: [10.1007/JHEP12\(2012\)061](https://doi.org/10.1007/JHEP12(2012)061). arXiv: [1209.6215 \[hep-ph\]](https://arxiv.org/abs/1209.6215).
- [93] W. Beenakker et al. "Squark and gluino production at hadron colliders". In: *Nucl. Phys. B* 492 (1997), p. 51. DOI: [10.1016/S0550-3213\(97\)00084-9](https://doi.org/10.1016/S0550-3213(97)00084-9). arXiv: [hep-ph/9610490 \[hep-ph\]](https://arxiv.org/abs/hep-ph/9610490).
- [94] A. Kulesza and L. Motyka. "Threshold Resummation for Squark-Antisquark and Gluino-Pair Production at the LHC". In: *Phys. Rev. Lett.* 102 (2009), p. 111802. DOI: [10.1103/PhysRevLett.102.111802](https://doi.org/10.1103/PhysRevLett.102.111802). arXiv: [0807.2405 \[hep-ph\]](https://arxiv.org/abs/0807.2405).
- [95] A. Kulesza and L. Motyka. "Soft gluon resummation for the production of gluino-gluino and squark-antisquark pairs at the LHC". In: *Phys. Rev. D* 80 (2009), p. 095004. DOI: [10.1103/PhysRevD.80.095004](https://doi.org/10.1103/PhysRevD.80.095004). arXiv: [0905.4749 \[hep-ph\]](https://arxiv.org/abs/0905.4749).
- [96] W. Beenakker et al. "Soft-gluon resummation for squark and gluino hadroproduction". In: *JHEP* 12 (2009), p. 041. DOI: [10.1088/1126-6708/2009/12/041](https://doi.org/10.1088/1126-6708/2009/12/041). arXiv: [0909.4418 \[hep-ph\]](https://arxiv.org/abs/0909.4418).
- [97] W. Beenakker et al. "Squark and gluino hadroproduction". In: *Int. J. Mod. Phys. A* 26 (2011), p. 2637. DOI: [10.1142/S0217751X11053560](https://doi.org/10.1142/S0217751X11053560). arXiv: [1105.1110 \[hep-ph\]](https://arxiv.org/abs/1105.1110).
- [98] S. Agostinelli et al. "GEANT4—a simulation toolkit". In: *Nucl. Instrum. Meth. A* 506 (2003), p. 250. DOI: [10.1016/S0168-9002\(03\)01368-8](https://doi.org/10.1016/S0168-9002(03)01368-8).
- [99] S. Abdullin et al. "The fast simulation of the CMS detector at LHC". In: *J. Phys. Conf. Ser.* 331 (2011), p. 032049. DOI: [10.1088/1742-6596/331/3/032049](https://doi.org/10.1088/1742-6596/331/3/032049).
- [100] A. Giannanco. "The Fast Simulation of the CMS Experiment". In: *J. Phys. Conf. Ser.* 513 (2014), p. 022012. DOI: [10.1088/1742-6596/513/2/022012](https://doi.org/10.1088/1742-6596/513/2/022012).
- [101] *Jet algorithms performance in 13 TeV data*. CMS Physics Analysis Summary CMS-PAS-JME-16-003. 2017. URL: <http://cds.cern.ch/record/2256875>.
- [102] A. Denner et al. "NLO QCD and electroweak corrections to $Z + \gamma$ production with leptonic Z-boson decays". In: *JHEP* 02 (2016), p. 057. DOI: [10.1007/JHEP02\(2016\)057](https://doi.org/10.1007/JHEP02(2016)057). arXiv: [1510.08742 \[hep-ph\]](https://arxiv.org/abs/1510.08742).
- [103] M. Cacciari et al. "The $t\bar{t}$ cross-section at 1.8 TeV and 1.96 TeV: a study of the systematics due to parton densities and scale dependence". In: *JHEP* 04 (2004), p. 068. DOI: [10.1088/1126-6708/2004/04/068](https://doi.org/10.1088/1126-6708/2004/04/068). arXiv: [hep-ph/0303085 \[hep-ph\]](https://arxiv.org/abs/hep-ph/0303085).
- [104] S. Catani et al. "Soft gluon resummation for Higgs boson production at hadron colliders". In: *JHEP* 07 (2003), p. 028. DOI: [10.1088/1126-6708/2003/07/028](https://doi.org/10.1088/1126-6708/2003/07/028). arXiv: [hep-ph/0306211 \[hep-ph\]](https://arxiv.org/abs/hep-ph/0306211).

- [105] G. Cowan et al. “Asymptotic formulae for likelihood-based tests of new physics”. In: *Eur. Phys. J.* C71 (2011). [Erratum: *Eur. Phys. J.* C73,2501(2013)], p. 1554. DOI: [10.1140/epjc/s10052-011-1554-0](https://doi.org/10.1140/epjc/s10052-011-1554-0), [10.1140/epjc/s10052-013-2501-z](https://doi.org/10.1140/epjc/s10052-013-2501-z). arXiv: [1007.1727 \[physics.data-an\]](https://arxiv.org/abs/1007.1727).
- [106] T. Junk. “Confidence level computation for combining searches with small statistics”. In: *Nucl. Instrum. Meth. A* 434 (1999), p. 435. DOI: [10.1016/S0168-9002\(99\)00498-2](https://doi.org/10.1016/S0168-9002(99)00498-2). arXiv: [hep-ex/9902006 \[hep-ex\]](https://arxiv.org/abs/hep-ex/9902006).
- [107] A. L. Read. “Presentation of search results: the CL_s technique”. In: *J. Phys. G* 28 (2002), p. 2693. DOI: [10.1088/0954-3899/28/10/313](https://doi.org/10.1088/0954-3899/28/10/313).
- [108] A. M. Sirunyan et al. “Search for gauge-mediated supersymmetry in events with at least one photon and missing transverse momentum in pp collisions at $\sqrt{s} = 13$ TeV”. In: *Phys. Lett. B* 780 (2018), p. 118. DOI: [10.1016/j.physletb.2018.02.045](https://doi.org/10.1016/j.physletb.2018.02.045). arXiv: [1711.08008 \[hep-ex\]](https://arxiv.org/abs/1711.08008).
- [109] B. Fuks et al. “Precision predictions for electroweak superpartner production at hadron colliders with Resummino”. In: *Eur. Phys. J.* C73 (2013), p. 2480. DOI: [10.1140/epjc/s10052-013-2480-0](https://doi.org/10.1140/epjc/s10052-013-2480-0). arXiv: [1304.0790 \[hep-ph\]](https://arxiv.org/abs/1304.0790).
- [110] B. Fuks et al. “Gaugino production in proton-proton collisions at a center-of-mass energy of 8 TeV”. In: *JHEP* 10 (2012), p. 081. DOI: [10.1007/JHEP10\(2012\)081](https://doi.org/10.1007/JHEP10(2012)081). arXiv: [1207.2159 \[hep-ph\]](https://arxiv.org/abs/1207.2159).
- [111] W. Beenakker et al. “The Production of charginos / neutralinos and sleptons at hadron colliders”. In: *Phys. Rev. Lett.* 83 (1999). [Erratum: *Phys. Rev. Lett.* 100,029901(2008)], pp. 3780–3783. DOI: [10.1103/PhysRevLett.100.029901](https://doi.org/10.1103/PhysRevLett.100.029901), [10.1103/PhysRevLett.83.3780](https://doi.org/10.1103/PhysRevLett.83.3780). arXiv: [hep-ph/9906298 \[hep-ph\]](https://arxiv.org/abs/hep-ph/9906298).
- [112] *Combined search for gauge-mediated supersymmetry with photons in 13 TeV collisions at the CMS experiment*. Tech. rep. CMS-PAS-SUS-18-005. Geneva: CERN, 2019. URL: <http://cds.cern.ch/record/2668332>.
- [113] A. M. Sirunyan et al. “Search for supersymmetry in events with a photon, a lepton, and missing transverse momentum in proton-proton collisions at $\sqrt{s} = 13$ TeV”. In: *JHEP* 01 (2019), p. 154. DOI: [10.1007/JHEP01\(2019\)154](https://doi.org/10.1007/JHEP01(2019)154). arXiv: [1812.04066 \[hep-ex\]](https://arxiv.org/abs/1812.04066).
- [114] A. M. Sirunyan et al. “Search for supersymmetry in final states with photons and missing transverse momentum in proton-proton collisions at 13 TeV”. In: *Submitted to: JHEP* (2019). arXiv: [1903.07070 \[hep-ex\]](https://arxiv.org/abs/1903.07070).